Heusler compounds as tunable material class for devices

Dissertation
zur Erlangung des Doktorgrades der Naturwissenschaften
(Dr. rer. nat.)

der

Naturwissenschaftlichen Fakultät II
Chemie, Physik und Mathematik
der Martin-Luther-Universität
Halle-Wittenberg,

vorgelegt von

Albrecht Köhler
geb. am 17. Februar 1987 in Leipzig

Evaluators:
1. Prof. Dr. S. S. P. Parkin (supervisor)
2. Prof. Dr. B. Hillebrands

Halle (Saale), November 15th 2016
Date of defense: July 4th 2017

I confirm that this is my own work and I have documented and indicated all sources and material used. Text and figures were partly taken from publications directly originating from this work.

Albrecht Köhler, 15th of November 2016

Ph.D. Thesis

Contents

Abbreviations

AC Alternating Current

AFM Atomic Force Microscopy or Antiferromagnet - depending on the context

AlTiC Aluminium Titanium Carbide

am.-Ta amorphous Tantalum

AP Antiparallel

CFA full Heusler compound Co_2FeAl

CFMS full Heusler compound $Co_2Fe_{0.4}Mn_{0.6}Si$

CIMS full Heusler compound $Co_{2-x}Ir_xMnSi$

CIPT Current-in-plane Tunneling

CMP Chemical Mechanical Processing

CMS full Heusler compound Co_2MnSi

CPP-GMR Current Perpendicular to Plane Giant Magnetoresistance

DC Direct Current

DOS Density Of States

FL Free Layer in a multilayer device stack

FM Ferromagnet or Ferromagnetic

FMR Ferromagnetic Resonance

FWHM Full Width Half Maximum of a peak

GMR Giant Magnetoresistance

HDD Hard Disk Drive

HM Half Metal or Halfmetallic

HRTEM High Resolution Transmission Electron Microscopy

IEC Interlayer Exchange Coupling

IP In Plane orientation for a corresponding magnetic field dependent measurement

MBE Molecular Beam Epitaxy

MOKE Magneto-Optic Kerr Effect

MR Magnetoresistance

MRAM Magnetic Read And Memory

MTJ Magnetic Tunnel Junction

NM Non-Magnet or Non-Magnetic

PID Proportional Integral Derivative

PIXE Particle-Induced X-ray Emission

PMA Perpendicular Magnetic Anisotropy

PSV Pseudo Spin Valve without AFM pinning in the stack

RA Resistance Area product

RBS Rutherford Backscattering

RF Radio Frequency

RKKY Ruderman-Kittel-Kasuya-Yosida interaction

RL Reference Layer in a multilayer device stack

RT Room Temperature (ambient)

RTA Rapid Transfer Annealing

SAF Synthetic Antiferromagnet

SNR Signal to Noise Ratio

SP Spin Polarization

SPM Scanning Probe Microscopy

SQUID-VSM Superconducting Quantum Interference Device

STEM Scanning Transmission Electron Microscopy

STT-RAM Spin Transfer Torque Read And Memory

SV Spin Valve

SZM Structure Zone Model

TMR Tunnel Magnetoresistance

VSM Vibrating Sample Magnetometer

WD Western Digital Corporation

XMCD X-ray Magnetic Circular Dichroism

XRD X-Ray Diffractometry

XRF X-Ray Fluorescence

XRR X-Ray Reflectometry

Nomenclature

A_θ absorption factor

α_i directional cosine for three directions

α dimensionless damping parameter

$\overline{C^2}$ polarization factor

E_{diff} diffusion barrier for adparticles

E_{ES} Ehrlich-Schwöbel barrier

E_F Fermi level image/profile

E_{kin} kinetic energy

G geometry factor

γ interface spin-scattering asymmetry

Γ two magnon scattering strength parameter

ΔH width of an FMR peak (with indexed origin)

H_c coercivity

H_d dipolar field from orange peel coupling as described by Néel

$\mathbf{H}_{eff}$ effective magnetic field vector within a material

H_{ex} exchange bias field of an FM in contact with an AFM

H_{res} FMR resonance field for a specific applied RF frequency

J_1 bilinear coupling strength

J_2 biquadratic coupling strength

L Lorentz factor

l_{sf} spin diffusion length

M_{eff} effective demagnetizing field

m_{hkl} multiplicity of the plane defined by Miller indices hkl

M_r remanence of a magnetic thin film

M_s saturation magnetization of a magnetic thin film

N_A Avogadro constant

p_{base} base pressure of a deposition chamber (no gas flow)

Q^T_{hkl} normalized texture quality factor

R_a average of absolute surface height of AFM surface image/profile

R_q root mean square average of height deviation of AFM surface image/profile

$R_{\square}$ sheet resistance (also termed $R_{\mathrm{b/t}}$ for bottom/top electrode)

R_z sum of maximum peak and minimum valley of AFM surface image/profile

$\tilde{t}$ thickness of magnetically dead layer of a magnetic thin film

T_a annealing temperature (in- or ex-situ)

T_C Curie temperature

T_{hkl} preferred orientation factor

T_m melting temperature

T_s substrate temperature

Introduction

Half-metallic (HM) ferromagnets attract considerable interest for spin-filtering applications. However, experimental observation of the half-metallic state is limited and the critical condition is to retain high *spin polarization* (SP) above *ambient/room temperature* (RT). Heusler compounds such as Co_2MnSi[1] (CMS) and Co_2FeAl[2] (CFA) that have high Curie temperatures are optimal candidates for these ventures. M_s of the two Heuslers is linked to the crystal structure, which develops generally as *amorph.* $\mapsto$ A2 $\mapsto$ B2 $\mapsto$ $L2_1$ with increasing annealing temperature T_a[3]. Half-metallicity for Heuslers originates from a strong d-band hybridization of the atoms on sublattice A and C, where the resulting anti-bonding states cannot couple with the element on sublattice B (see fig. 1), leading to a gap across the Fermi-level E_F.

CMS[4], is a prominent and well studied candidate for *tunnel magnetoresistance* (TMR, see p. 85)[5], *current perpendicular to plane giant magnetoresistance* (CPP-GMR)[6], *spin transfer torque read and memory* (STT-RAM)[7] spintronic devices and recently a SP of at least 93% has been reported, even after rather mild annealing procedures[8]. It furthermore constitutes a robust half metal that is unaffected by B2 disorder[9]. However, partial Co-Mn antisite disorder with increasing annealing temperatures can give rise to defect scattering in bulk[10] and thin films[11], which effectively reduces SP. CMS is the record holder in terms of highest TMR for Heuslers used in *magnetic tunnel junctions* (MTJ), i.e. 1995% at 4.2 K and 354% at 290 K[12]. The current record holder of Heuslers at RT is $Co_2FeAl_{0.5}Si_{0.5}$ with 386% at RT (832% at 9 K)[13], where the films were grown via *molecular beam epitaxy* (MBE).

CFA is another prominent Co-based full Heusler and is currently ranking second highest Heusler-based TMR at RT with 360% (785% at 10K)[14]. B2 and $L2_1$ phase have a similar theoretical bulk SP of around 30%[15]. Strictly speaking, CFA is not a half metal, but exhibits a perfectly spin-polarized Δ_1 band in the [001] direction, which means that Δ_1 bands exist for the majority spin but not for the minority spin at E_F[16]. *Inomata et al* evaluated SP = 0.99 from MgO-MTJs with Cr-buffered CFA when applying Julliere's model[17]. This matches with the calculated band dispersions in the [001] direction and demonstrates the almost half-metallic nature of CFA. HM Heuslers exhibit the highest *magnetoresistance* (MR) ratios for CPP-GMR, which is likely going to be the next generation type of *hard disk drive* (HDD) read sensor (see chapter on p. 93).

[1] U. Geiersbach, A. Bergmann, and K. Westerholt, *J. Magn. Magn. Materials* **240**, 1-3 (2002), pp. 546–549

[2] K.H.J. Buschow, P.G. van Engen, and R. Jongebreur, *J. Magn. Magn. Materials* **38**, 1 (1983), pp. 1–22

[3] T. Graf, C. Felser, and S. S. P. Parkin, *Progress in Solid State Chemistry* **39**, 1 (2011), pp. 1–50

[4] I. Galanakis, P. H. Dederichs, and N. Papanikolaou, *Phys. Rev. B* **66** (17 2002), p. 174429, S. Picozzi, A. Continenza, and A. J. Freeman, *Phys. Rev. B* **66**, 9 (2002), p. 094421

[5] G. Li et al., *Phys. Rev. B* **89** (1 2014), p. 014428, H. Liu et al., *Appl. Phys. Lett.* **101**, 13, 132418 (2012), Y. Sakuraba et al., *Jap. J. Appl. Phys.* **44**, 35 (2005), pp. 1100–1102

[6] T. Iwase et al., *Appl. Phys. Express* **2**, 6 (2009), p. 063003, Y. Sakuraba et al., *Phys. Rev. B* **82** (9 2010), p. 094444

[7] L. Tang and Z. Yang, *J. Appl. Physics* **114**, 19 (2013), p. 193703

[8] M. Jourdan et al., *Nat. Commun.* **5** (2014), p. 3974

[9] S. Picozzi, A. Continenza, and A. J. Freeman, *Phys. Rev. B* **69**, 9 (2004), p. 094423

[10] M. P. Raphael et al., *Phys. Rev. B* **66** (10 2002), p. 104429

[11] Y. Sakuraba et al., *Phys. Rev. B* **82** (9 2010), p. 094444

[12] H. Liu et al., *Appl. Phys. Lett.* **101**, 13, 132418 (2012)

[13] N. Tezuka et al., *Appl. Phys. Lett.* **94**, 16, 162504 (2009)

[14] W. Wang, H. Sukegawa, and K. Inomata, *Phys. Rev. B* **82** (9 Sept. 2010), p. 092402

[15] Y. Miura, K. Nagao, and M. Shirai, *Phys. Rev. B* **69** (14 Apr. 2004), p. 144413

[16] W. Wang et al., *Phys. Rev. B* **81** (14 Apr. 2010), p. 140402

[17] C. Felser and G. H. Fecher, Spintronics: From Materials to Devices, Springer Berlin Heidelberg, 2013

The lattice mismatch of CMS ($a = 5.645$ Å) and CFA ($a = 5.730$ Å) with MgO ($a = 4.21$ Å) is –4.9% and –3.8%, respectively[18]. This leads to a an in-plane lattice elongation in (001)-epitaxial thin films, which reduces the unit cell height, depending on film thickness. Appropriate choice of underlayers and capping materials can induce strain in the Heusler in order to optimize the lattice matching with the MgO barrier for TMR applications. Lattice constants for polycrystalline CFA films are reported to decrease from 5.700 Å to 5.675 Å when reducing the thickness from 1000 Å to 100 Å[19]. For HDD read sensors, polycrystalline Heusler thin films have to be developed with the aspiration of achieving comparable record values as their epitaxial counterparts.

The aim of this work is to portray opportunities and obstacles of the implementation of highly *spin-polarized* Heusler compounds into nanoscale device technologies, specifically devices that utilize CPP-GMR and TMR. Tunability of this compound class will be demonstrated by developing a novel quaternary soft-magnetic Heusler $Co_{2-x}Ir_xMnSi$ and tuning the magnetic anisotropy of the hard-magnetic Mn-Ga based perpendicularly magnetized Heuslers[20]. Fundamental magnetic properties of these Heuslers will be exposed and related to their growth mechanisms in thin films. Successful TMR device implementation of Co_2MnSi and Co_2FeAl and a road map for CPP-GMR integration will be presented.

[18] K.H.J. Buschow, P.G. van Engen, and R. Jongebreur, *J. Magn. Magn. Materials* **38**, 1 (1983), pp. 1–22

[19] M. Belmeguenai et al., *J. Magn. Magn. Materials* **373** (2015), pp. 140–143

[20] A detailed introduction will be given in the relevant chapter.

Measurement techniques

XRD

X-ray diffractometry (XRD) is a method for identifying the atomic structure of a compound or molecule. X-rays diffract form the specimen following an underlying set of physical rules. Let's start with considering a unit well where the primitive vectors **a**, **b** and **c** of the crystal lattice span the unit cell of a compound. Their periodic repetition constructs the *Bravais lattice* $\mathbf{R} = n_1\mathbf{a} + n_2\mathbf{b} + n_3\mathbf{c};\ n_\mathrm{i} \in \mathbb{Z}$. The most common crystal systems are cubic, tetragonal and hexagonal with $a = |\mathbf{a}|$ and $c = |\mathbf{c}|$ being the lattice constants of the unit cell. A diffraction event now follows the Laue condition. It states that the scattering has to take place in specific directions related to the primitive vectors, i.e. the scattering vector **k** has to be equal to a reciprocal lattice vector $\mathbf{Q} = h\mathbf{x} + k\mathbf{y} + l\mathbf{z};\ h,k,l \in \mathbb{Z}$. The definition of the reciprocal lattice vectors is:

$$\begin{aligned}\mathbf{x} &= 2\pi\frac{\mathbf{b}\times\mathbf{c}}{\mathbf{a}\,(\mathbf{b}\times\mathbf{b})}\\ \mathbf{y} &= 2\pi\frac{\mathbf{c}\times\mathbf{a}}{\mathbf{b}\,(\mathbf{c}\times\mathbf{a})}\\ \mathbf{z} &= 2\pi\frac{\mathbf{a}\times\mathbf{b}}{\mathbf{c}\,(\mathbf{a}\times\mathbf{b})}\end{aligned} \tag{1}$$

Because the Laue condition states that $\mathbf{k} = \mathbf{Q}$ it is possible to identify the reflex-contributing Miller indices:

$$\begin{aligned}\mathbf{a}\cdot\mathbf{k} &= 2\pi\mathrm{h}\\ \mathbf{b}\cdot\mathbf{k} &= 2\pi\mathrm{k}\\ \mathbf{c}\cdot\mathbf{k} &= 2\pi\mathrm{l}\end{aligned} \tag{2}$$

with Miller indices h, k and l. Geometrically, Miller indices are related to the distance d_hkl of parallel lattice planes. The relation depends on the crystal system:

$$\frac{1}{d_\mathrm{hkl}^2} = \begin{cases}\dfrac{\mathrm{h}^2+\mathrm{k}^2+\mathrm{l}^2}{a^2} & \text{(cubic)} \quad (3a)\\ \dfrac{\mathrm{h}^2+\mathrm{k}^2}{a^2} + \dfrac{\mathrm{l}^2}{c^2} & \text{(tetragonal)} \quad (3b)\\ \dfrac{4}{3}\dfrac{\mathrm{h}^2+\mathrm{hk}+\mathrm{k}^2}{a^2} + \dfrac{\mathrm{l}^2}{c^2} & \text{(hexagonal)} \quad (3c)\end{cases}$$

The Bragg equation is equivalent to the Laue condition, but expresses the scattering angle θ_{hkl} vs. the interplanar spacing of lattice planes $d = d_{hkl}$ and relates them to the used X-ray radiation wavelength λ:

$$\lambda = 2d_{hkl} \sin\theta_{hkl}. \tag{4}$$

Both Bragg and Laue equations can be combined to interpret diffraction data and to extract information by e.g. assigning Miller indices to the observed reflexes. Cu $K_{\alpha 1}$ radiation with $\lambda = 1.541\,84$ Å is used for the structural analysis of the samples.

Reflex intensities

The intensity of the reflexes relates to the *atomic form factor* f, which is the Fourier transform of the spatial electronic charge distribution ρ_e of the scattering atom. ρ_e equals the square of the electronic wave function. f can be approximated by a model function with nine coefficients a_j, b_j, c (j=1, 2, 3) which can be found in crystallographic standard tables[21].

[21] P. J. Brown et al., vol. C, Springer, 2004, p. 554

$$f = \int_{at} \rho_e(\mathbf{r}) \exp(-i\mathbf{Q}\mathbf{r}) d\mathbf{r} \approx \sum_{j=1}^{4} a_j \exp\left(-b_j \sin^2\theta/\lambda^2\right) + c \tag{5}$$

where $\mathbf{r}$ is the location of point charges. In the case of $\theta \to 0 \Leftrightarrow \mathbf{Q} \to 0$, the integral on the left hand side just runs over the charge distribution, meaning that for small scattering angles the atomic form factor f equals the number of electrons, i.e. atomic number Z.
The next step is to extend the integration in eq. 5 over the total charge contribution of the N atoms in the unit cell in order to obtain the *structure factor* $\mathbf{F}$, which is a complex quantity. It sums up the involved atomic form factors, multiplied with complex phase factor:

$$\mathbf{F} = \sum_{n=1}^{N} \int_{at} \rho_e(\mathbf{r}) \exp(-i\mathbf{Q}(\mathbf{r} - \mathbf{r}_n)) d\mathbf{r} = \sum_{n=1}^{N} f_n \exp\left(i\mathbf{Q}\mathbf{r}_n\right) \tag{6}$$

By introducing fractional atomic coordinates $\mathbf{r}_n = u_n\mathbf{a} + v_n\mathbf{b} + w_n\mathbf{c}$ and using the Laue conditions (eq. 2) one can rewrite eq. 6 to

$$\mathbf{F} \to \mathbf{F}_{hkl} = \sum_{n=1}^{N} f_n \exp\left[2\pi i \left(hu_n + kv_n + lw_n\right)\right]. \tag{7}$$

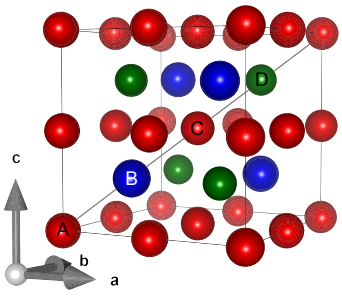

Figure 1: Heusler unit cell of the $L2_1$ structure (space group 225). Sublattice A and C are occupied by Co (red), while B and D holds Mn (blue) and Si (green), respectively.

The total intensity reaching the detector is ultimately proportional to the product of $\mathbf{F}_{hkl}$ and its complex conjugate $\mathbf{F}^*_{hkl}$

$$I \propto |\mathbf{F}_{hkl}|^2 \tag{8}$$

To simulate a full Heusler XRD spectrum, a good start is to sort the (hkl) reflexes by their position θ_{hkl}. To do so, list solutions of eqs. 3a-3c for the respective lattice and then solve eq. 4 for θ_{hkl}. Some of the reflexes can already be excluded, since their intensity is zero. In case of a Heusler this is because the $L2_1$ structure can be seen as four interpenetrating fcc lattices, each shifted by (a/4, a/4, a/4) relative to

each other and occupied with 4 atoms of an element A, B, C and D, exemplified for Co_2MnSi in fig. 1. Entering the fcc fractional atomic coordinates (u_n,v_n,w_n; n = 1–4)[22] into eq. 7 gives real values for all fcc $\mathbf{F}_{hkl}$. E.g. for the sublattice that is occupied with element A

$$F^{A}_{hkl} = \begin{cases} 4f^{A} & \text{all hkl are even or odd,} \\ 0 & \text{hkl are mixed,} \end{cases} \tag{9}$$

All 4 sublattice form factors can now be added with taking their phase shift $\mathbf{p}_{hkl}(m) \equiv \exp\left[m \cdot i\frac{\pi}{2}(h+k+l)\right]$ with $m = 0,1,2,3$ into account, which is a consequence of eq. 7:

$$\mathbf{F}_{hkl} = F^{A}_{hkl} + F^{B}_{hkl}\mathbf{p}_{hkl}(1) + F^{C}_{hkl}\mathbf{p}_{hkl}(2) + F^{D}_{hkl}\mathbf{p}_{hkl}(3). \tag{10}$$

Eq. 8 is applied to obtain the final intensity for the (hkl) reflex. $|\mathbf{p}_{hkl}(m)\mathbf{p}_{hkl}(m)^*| = \pm 1$ and the sign depends on m and the choice of h, k and l. This creates multiple combinations, but they can be broken down into three main cases:

$$I_{hkl} = 16\left[\left(f^{A} - f^{C}\right)^2 + \left(f^{B} - f^{D}\right)^2\right] \quad \text{h+k+l is odd,} \tag{11}$$

$$= 16\left[\left(f^{A} + f^{C}\right) - \left(f^{B} + f^{D}\right)\right]^2 \quad \text{(h+k+l)/2 is odd,} \tag{12}$$

$$= 16\left(f^{A} + f^{C} + f^{B} + f^{D}\right)^2 \quad \text{(h+k+l)/2 is even} \tag{13}$$

Eqs. 11–13 demonstrate how an element contributes to a specific $L2_1$ reflex intensity. This helps to identify the impact of disorder on I_{hkl} by swapping the atomic form factors within the equation and it will be the basis for identifying the minimum ordering from later XRD measurements. The fundamental (004) peak (eq. 13) is unaffected by any type of disorder within the fcc-sublattices and thus quantifies random A2 order, see fig. 2 for Co_2MnSi. In a full Heusler, the most electropositive element[23] occupies both sublattices A and C and anti-sites between these two sublattices do not affect $L2_1$ order. Swapping atoms randomly from sublattices B and D however defines B2 order and this has no influence on the result of eq. 12, making the (002) reflex intensity unaffected (only) by B2 order, see fig. 3. The (111) peak (eq. 11) is affected by any other order than $L2_1$. For Co_2MnSi it increases for Co-Mn anti sites (lattice B/C), see fig. 4, and decreases for all other disorder types. The appearance of the (111) peak during the measurement in combination with high magnetization prove $L2_1$ structure, because Co-Mn anti-sites would drastically reduce the magnetization of the unit cell.
Lastly, the intensity I_{hkl} has to be corrected by following some considerations below. The factors in square brackets are only to be used for the evaluation of randomly oriented (hkl) reflexes of polycrystalline samples, not for epitaxial growth or fully textured films, as will be explained.

$$I_{hkl} = |\mathbf{F}_{hkl}|^2 \cdot T_{hkl} \cdot A_\theta \cdot [m_{hkl}] \cdot [G] \cdot \overline{C^2} \cdot L \cdot SCF \tag{14}$$

[22] specifically they are (0, 0, 0), $(\frac{1}{2}, \frac{1}{2}, 0)$, $(\frac{1}{2}, 0, \frac{1}{2})$ and $(0, \frac{1}{2}, \frac{1}{2})$

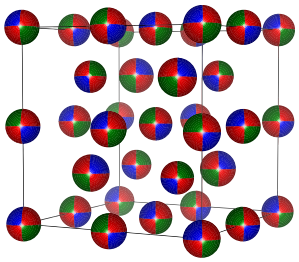

Figure 2: A2 (space group 229) disorder of a full Heusler. The sublattice is randomly occupied with Co (red), Mn (blue) and Si (green).

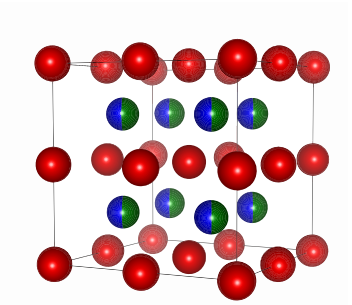

Figure 3: B2 (space group 221) disorder of a full Heusler, where there is random Mn (blue) and Si (green) occupation on the sublattice B and D. Co (red) is on the correct Heusler sublattice.

[23] T. Graf, C. Felser, and S. S. P. Parkin, *Progress in Solid State Chemistry* **39**, 1 (2011), pp. 1–50

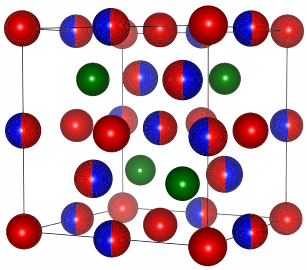

Figure 4: X (space group 216) disorder of a full Heusler. Co-Mn anti-sites, Co (red) and Mn (blue), occupy sublattice B and C.

Contribution of atomic thermal vibrations to $\mathbf{F}_{hkl}$

They effectively displace atoms within the lattice and therefore spatially extend the electronic charge distribution while reducing coherency. A temperature-dependent factor is introduced and multiplied with the atomic form factors f_n in eq. 7:

$$f_\mathrm{T} = f_\mathrm{n} \exp\left(-8\pi\overline{u^2}\sin^2\theta/\lambda^2\right) \tag{15}$$

with $\overline{u^2}$ being the mean quadratic variation of the atom around its average position and the diffraction angle θ. This correction is only relevant for temperature dependent XRD and is set to zero within the scope of this work since all measurements are performed at RT.

Preferred orientation (texture) T_{hkl}

Random orientation uses a factor $T_\mathrm{hkl} = 1$ for every hkl, but preferred orientation of specific grains can relatively increase corresponding Bragg reflexes, which is taken into account by introducing $T_\mathrm{hkl} \neq 1$, e.g. by setting this value to zero in case of an absent peak. On page 37 and following, the factor $Q^\mathrm{T}_\mathrm{hkl}$ is introduced, which resembles the measured intensity of a reflex (hkl), but multiplied by factor $I^0_\mathrm{max}/I^0_\mathrm{hkl}$, where I^0_hkl is the expected theoretical peak area and I^0_max is the strongest powder pattern reflex. In the case of a random orientation $Q^\mathrm{T}_\mathrm{hkl}$ then would have the same value for any hkl. $Q^\mathrm{T}_\mathrm{hkl}$ is therefore useful to quantize preferred orientation and $Q^\mathrm{T}_\mathrm{hkl} = T_\mathrm{hkl} \cdot \frac{I^0_\mathrm{max}}{t}$. t is the film thickness and I^0_max depends only on the measurement settings such chosen slits, which will be the same for all conducted $2\theta/\omega$ scans. It wouldn't make physical sense to utilize T_hkl for epitaxial samples.

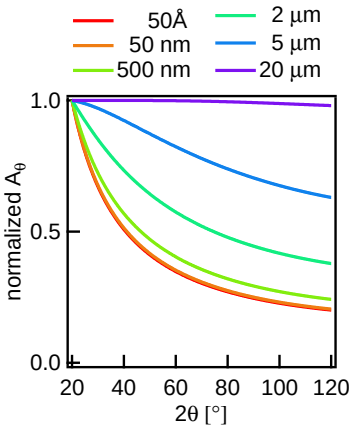

Figure 5: normalized A_θ illustrates the influence of eq. 16 on the evolution of the relative peak height with increasing scattering angle θ. It is shown for different thin film thicknesses with $\mu_\mathrm{CMS} = 1.7\text{+E3 cm}^{-1}$ and is normalized to the value $A_\theta(2\theta = 20°)$

Absorption factor A_θ

X-rays are absorbed in the specimen following the Lambert-Beer law. The absorption decreases with θ and is expressed as

$$A_\theta = 1 - \exp\left(-\frac{2\mu t}{\sin\theta}\right) \tag{16}$$

with the linear attenuation coefficient μ, which depends on the density of the material and the X-ray energy. Eq. 16 can alter the relative peak heights of thin films with nanometer thickness considerably when compared to a powder sample where $\lim_{t\to\infty} A_\theta = 1$, see figs. 5.

Lattice multiplicity m_{hkl}

Every lattice plane has a number of equivalent planes within the crystal, e.g. the plane ensemble $(\bar{1}11)$, $(1\bar{1}1)$ and $(11\bar{1})$. In fact, there are 8 equivalent planes the add to the (111) reflex intensity, defining it multiplicity $m_{111} = 8$. Symmetry-equivalent reflections can be measured

individually for epitaxial samples in $2\theta/\omega$ geometry, but for polycrystalline specimen (or samples with partial texture) the diffracted beam of randomly oriented crystallites is smeared out over a circle. Its intensity scales with m_{hkl} and has to be multiplied to each (hkl) reflex. E.g. $m_{002} = 6$, $m_{022} = 12$.

Geometry factor G

The circular smearing of the diffraction beam that has been mentioned when considering multiplicity for polycrystalline samples also has a geometrical effect: The circumference of the intensity ring scales with $\sin 2\theta$ and the dilution is inversely proportional. And the density of scattering vectors $\mathbf{Q}$ that lie on the cone scales with $\cos\theta$, thus

$$G = \frac{\cos\theta}{\sin 2\theta} = \frac{1}{2\sin\theta}. \tag{17}$$

$G = 1$ for single crystals[24].

[24] R. C. Reynolds, *Clays and Clay Minerals* **34**, 4 (1986), pp. 359–367

Polarization factor $\overline{C^2}$

X-ray tubes emit randomly polarized photons. Therefore there is a δ- and π-component of the scattered radiation leading to an angularly dependent polarization factor

$$\overline{C^2} = \frac{1 - K + K \cdot \cos^2 2\theta \cdot \cos^2 2\theta_{\mathrm{M}}}{2} \tag{18}$$

K is the fractional polarization of the beam and θ_{M} is the Bragg-angle of the Monochromator crystal. $K = 0.5$ and $\cos^2 2\theta_{\mathrm{M}} = 1$ for non-monochromatic radiation.

Lorentz factor L

The Lorentz factor arises from the finite spread of the diffraction cone width for a polycrystalline sample. Or in other words due to the fact that the reciprocal lattice does not consist of infinitesimal points in reality, but is rather smeared out.

$$L = \frac{1}{\sin 2\theta} \tag{19}$$

Instrumental scaling factor SCF

The SCF is a product of constants such as the volume of the unit cell and the used X-ray wavelength. It also combines all the instrumental settings like scan velocity and slit width and is irrelevant for relative peak height comparison.

Eq. 14 is evaluated for powder samples, random polycrystalline and epitaxial thin films ($t = 180$ Å) for four ordering types $L2_1$, X, B2, A2. The respective peak heights are shown for CMS in fig. 6. In the case

of thin films with pure (hkl) texture, all crystallites are oriented in the same direction with (hkl) planes (and multiples) parallel to the sample surface. Thus the factors m_{hkl} and G are not effective in eq. 14 for these particular reflexes, wherefore this case is treated analogously to the epitaxial case in $2\theta/\omega$ geometry.

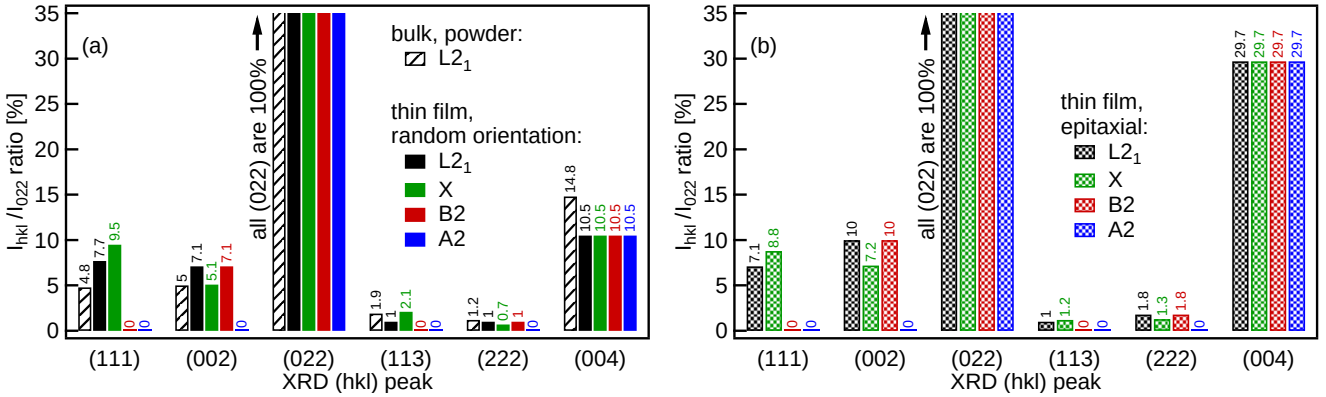

Figure 6: calculated XRD peak heights for Heusler compound Co_2MnSi in the $2\theta/\omega$ geometry with Cu K_α radiation. Four different types of order are shown: $L2_1$, B2, A2 and X, as previously introduced. (a) bulk (powder) and random polycrystalline thin films; (b) epitaxial thin films; all thin films have $t = 180$ Å.

XRF

X-ray fluorescence (XRF) is a non-destructive chemical analysis of materials. An incident X-ray beam (continuous and discrete spectrum of a single element source, e.g. Rh, W, Mo or others, depending on energy range needed) ionizes the atoms of the specimen by ejecting one or more electrons from inner atomic shells which are labeled by a capital letter (K, L, M, ...). This vacancy is filled with an electron from a higher orbital, releasing a photon with an energy equal to the difference of the two orbitals. The energy difference of the two participating orbitals is indicated by a small greek letter (α, β, γ, ...). Thus the emitted radiation is characteristic of the atoms present and the respective peak intensities are proportional to the elemental concentration. The absorption of X-rays in the sample follows the Lambert-Beer law (see absorption factor A_θ; previously explained in the XRD section) and in the case of thin films there is a considerable contribution from the substrate, which has to be accounted for. Choosing different spot sizes results in varying substrate background signals and calibration has to be performed for each spot size. The XRF technique can also be used for precise thickness measurements of single- or multilayers by comparing measured peak heights with the peaks in a spectrum of a thin film with known thickness. The term *fluorescence* generally describes the absorption of electromagnetic radiation of a specific energy and the re-emission of radiation of a different energy.

XRR

X-ray reflectometry (XRR) is a non-destructive method to measure thickness, roughness and density of a single or multilayer thin film of thickness $1 < t < 10000$ Å. The angle θ between incoming beam and surface is typically smaller than 5°, setting the probed length-scale as $d = \lambda/2\sin\theta$, where λ is the X-ray wavelength. The incoming beam gets reflected on the surface due to interference with the thin film interfaces. The scattering vector $\mathbf{k} \to k_z$ transfer is therefore perpendicular to the sample surface. The intensity I is proportional to the scattering function $S(k_z)$ which is the Fourier transform of the laterally averaged electron density $\rho(z) = \langle \rho(x,y,z) \rangle_{x,y}$ of the material:

$$S(k_z)^2 = \left| \int_0^t \rho(z) \exp(ik_z z) dz \right|^2 \tag{20}$$

The partial reflected intensity r of a wave on a surface is described by the resolution function R.

$$r(k_z) = |R(k_z)|^2 = \left| \frac{k_z - k_0}{k_z - k_0} \right|^2 \tag{21}$$

where $k_0 = \sqrt{k_z^2 - 16\pi\rho r_e}$ and r_e being the electron radius. To account for the roughness, eq. 21 is multiplied by the factor $\exp(-\sigma^2 k_z/2)$, where σ is the standard deviation of the roughness profile. For the total intensity, eq. 20 is convoluted with eq. 21 to obtain the intensity I:

$$I(k_z) = \int |S(k_z)|^2 R(k_z - k) dk \tag{22}$$

Below the critical angle $\theta_c \propto \sqrt{\rho}$ of the material there is total reflection, which limits the angular range for light materials. The interference of the reflected waves causes *Kiessig fringes*[25] of period $\Delta k_z = 2\pi/t$. The amplitude of the fringes increases sensitively with density.

[25] H. Kiessig, *Annalen der Physik* **402**, 7 (1931), pp. 769–788

FMR

Ferromagnetic resonance (FMR) is a spectroscopic technique to probe magnetic properties and spin dynamics of ferromagnetic materials. FMR arises from the precessional motion of the magnetization in a magnetic field and for materials that are magnetized in-plane the frequency of this precession is typically *radio frequency* (RF). The phenomenological basis is laid out by the Landau-Lifshitz-Gilbert[26] (LLG) equation for a magnetization $\mathbf{M}(t)$ in an effective magnetic field $\mathbf{H}_{\text{eff}}$

$$\frac{d\mathbf{M}}{dt} = -\gamma \mathbf{M} \times \mathbf{H}_{\text{eff}} + \frac{\alpha}{M_s} \mathbf{M} \times \frac{d\mathbf{M}}{dt} \tag{23}$$

where γ is the gyromagnetic ratio in Hz/Oe, α is the dimensionless damping parameter and M_s is the saturation magnetization. γ of an electron includes the *g-factor*, i.e. $\gamma = g\mu_B/\hbar$. The equation describes

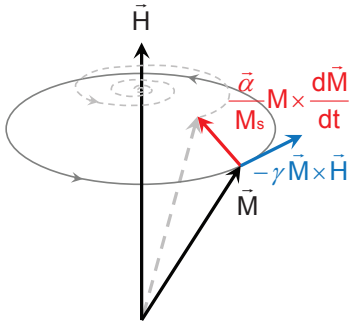

Figure 7: magnetization dynamics as described by the LLG equation.

[26] T. L. Gilbert, *Phys. Rev.* **100** (1955), p. 1243, L. Landau and Lifshitz, *Phys. Z. Sowj.* **8**, 153 (1935), link, pp. 101–114

the precessing motion of $\mathbf{M}(t)$, while a damping torque (second term on the right hand side) is acting perpendicularily on the magnetization vector which ultimately reduces its angular momentum, see fig. 7. The resonance condition is governed by $\mathbf{H}_{\text{eff}}$ and is obtained by minimizing the total energy

$$\mathbf{H}_{\text{eff}} = \delta\mathcal{E}_{\text{tot}}/\delta\mathbf{M} \tag{24}$$

$\mathcal{E}_{\text{tot}}$ is a sum of three contributions:

- demagnetization energy: if $\mathbf{M}$ has a component along the thin film normal: $\mathcal{E}_{\text{dem}} = 2\pi D M_s^2 cos\theta_M^2$, with the demagnetizing factor D and θ_M being the angle of the magnetization with respect to the surface normal.
- anisotropy energy: is composed of the fourfold (cubic) crystalline and uniaxial anisotropy K_1 and K_U, respectively. $\mathcal{E}_{\text{ani}} = -\frac{K_1^{\parallel}}{2}\left(\alpha_1^4 + \alpha_2^4\right) - \frac{K_1^{\perp}}{2}\alpha_3^4 - K_U^{\perp}\alpha_3^2 - K_U^{\parallel}\frac{(\hat{\mathbf{n}}\cdot\mathbf{M})^2}{M_s^2}$ where α_i are directional cosines of the magnetization vector in respect to the crystallographic axes. $K_U^{\perp}$ and $K_1^{\perp}$ are the second and fourth order terms of the perpendicular anisotropy. $K_1^{\parallel}$ is the fourfold in-plane magnetocrystalline anisotropy and $K_U^{\parallel}$ is an optional in-plane uniaxial anisotropy. The anisotropy field can then be derived as $\mathbf{H}_{\text{ani}} = \delta\mathcal{E}_{\text{ani}}/\delta\mathbf{M}$
- Zeeman energy: interaction of the magnetization with the external field $\mathbf{H}_0$ gives rise to $\mathcal{E}_{\text{zee}} = -\mathbf{H}_0 \cdot \mathbf{M}$

In-plane configuration (IP)

$K_1^{\perp}$ plays a negligible role in the in-plane configuration, since it scales with the third power of the perpendicular magnetization component, it is therefore dropped here.
The directional cosines α_i can be parameterized by using polar coordinates for the direction of $\mathbf{M}$ and $\mathbf{H}_0$ relative to the crystallographic axis and expressing the motion of $\mathbf{M}$ in its own coordinate system $\mathbf{M} = (M_x, M_y, M_z)$. With this parameterization the differentiation of the total energy via eq. 24 is possible and gives $\mathbf{H}_{\text{eff}}$ which enters the LLG equation (eq. 23). Furthermore setting $\mathbf{M} = M_s\vec{\mathbf{x}} + m_y^{RF}\vec{\mathbf{y}} + m_z^{RF}\vec{\mathbf{z}}$ (small angle approximation $M_x \gg M_y, M_z$) leads to set of coupled equations, that ultimately define the resonance condition[27]:

$$f = \frac{\gamma}{2\pi}\sqrt{\mathfrak{B}_{\text{eff}}\mathfrak{H}_{\text{eff}}} \tag{25}$$

$$\begin{aligned}\mathfrak{B}_{\text{eff}} =& H_0\cos\left(\varphi_M - \varphi_H\right) + 4\pi D M_s - \frac{2K_U^{\perp}}{M_s} \\ &+ \frac{2K_U^{\parallel}}{M_s}\cos^2\left(\varphi_M - \varphi_U\right) + \frac{K_1^{\parallel}}{2M_s}\left[3 + \cos 4\varphi_M\right]\end{aligned} \tag{26}$$

$$\mathfrak{H}_{\text{eff}} = H_0\cos\left(\varphi_M - \varphi_H\right) + \frac{2K_U^{\parallel}}{M_s}\cos 2\left(\varphi_M - \varphi_U\right) + \frac{2K_1^{\parallel}}{M_s}\cos 4\varphi_M \tag{27}$$

[27] M. Belmeguenai et al., *J. Magn. Magn. Materials* **321**, 7 (2009), pp. 750–753

Where φ_M and φ_H are the in-plane angles of $\mathbf{M}$ and $\mathbf{H}_0$ with the [001] crystallographic direction, respectively. By assuming a saturated sample, i.e. $\mathbf{M} \parallel \mathbf{H}_0$ one may further set $\varphi_M = \varphi_M \equiv \varphi$, leading to $\cos(\varphi_M - \varphi_H) = 1$.
Eq. 25 with eqs. 26 and 27 are usually applied to epitaxial samples, where there is an in-plane angular dependency of the anisotropy fields. For polycrystalline samples simplifications can be made: with an absence of in-plane uniaxial anisotropy and random in-plane orientation of the crystallites, the terms in eq. 26 and 27 containing $K_U^{\parallel}$ and $K_1^{\parallel}$ are no longer dependent on φ. In this case and with using the resonance location H_{res}, $H_0 \rightarrow H_{res}$ eq. 25 leads to

$$f(H_{res}) = \frac{\gamma}{2\pi}\sqrt{(H_{res} + 4\pi M_{eff} + H_K)(H_{res} + H_K)} \tag{28}$$

with $H_K \equiv 2K^{\parallel}/M_s$ comprising averaged in-plane anisotropic field contributions. The values for H_K are typically small and are generally thickness dependent. The effective demagnetizing field is defined as $4\pi M_{eff} = 4\pi D M_s - 2K_U^{\perp}/M_s$.

In the case of non-zero in-plane anisotopy, the resonance condition can be recorded for varying in-plane field angles φ at fixed frequency f. For the investigations here it is convenient to choose a frequency for which the sample is saturated, i.e. $\mathbf{M} \parallel \mathbf{H}_0$. 20 GHz is a good choice for the materials used in this work. Eq. 25, 26 and 27 are rewritten to express the resonance position versus the in-plane magnetic field angle, i.e. $H_{res}(\varphi)$, so again with $H \rightarrow H_{res}$:

$$H_{res}(\varphi) = \sqrt{\left(\frac{2\pi f}{\gamma}\right)^2 + \left(\frac{A-B}{2}\right)^2} - \frac{A+B}{2} \tag{29}$$

$$A - B = \frac{K_U^{\parallel}}{M_s}(\cos 2(\varphi - \varphi_U) - 1) + \frac{3K_1^{\parallel}}{2M_s}(\cos 4\varphi - 1) - 4\pi M_{eff} \tag{30}$$

$$A + B = 4\pi M_{eff} + \frac{K_U^{\parallel}}{M_s}(3\cos 2(\varphi - \varphi_U) + 1) + \frac{K_1^{\parallel}}{2M_s}(5\cos 4\varphi + 3). \tag{31}$$

Additional interface anisotropy at the two interfaces A and B can arise from the exchange interaction in the case of ultrathin films, and can be separated from the bulk contribution by performing thickness dependent measurements:

$$K = K^{bulk} + \frac{K^A}{t} + \frac{K^B}{t}. \tag{32}$$

K can be any kind of anisotropy except magnetocrystalline, with $K_U^{\perp}$ generally being the strongest contribution.
The *full width half maximum* (FWHM) ΔH of the resonance peak is

connected to the damping parameter α via

$$\Delta H_{\shortparallel}(f) = \frac{4\pi\alpha}{\gamma\sqrt{3}} f + \Delta H_{0,\shortparallel} + \Delta H_{2\mathrm{M}}(f) \tag{33}$$

where the first part denotes the intrinsic Gilbert damping (with the intrinsic damping parameter α) due to magnon-electron scattering and $\Delta H_{2\mathrm{M}}(f)$ is the extrinsic broadening connected to *two-magnon scattering* (2M). The latter arises from weak interactions between the spin-wave modes that effectively allow energy dissipation of the uniform precession into other modes[28]. Additionally, imperfections generate the frequency-independent extrinsic contribution $\Delta H_{0,\shortparallel}$, due to microstructural differences such as local anisotropies or magnetostriction. Eddy current damping[29], where random inhomogeneities spread the linewidth by the superposition of multiple local FMR absorption profiles[30] is negligible for the thicknesses to be investigated here. The 2M contribution can be expressed as[31]

$$\Delta H_{2\mathrm{M}}(f) = \Gamma \sin^{-1}\sqrt{\frac{\sqrt{f^2+(f_0/2)^2}-(f_0/2)}{\sqrt{f^2+(f_0/2)^2}+(f_0/2)}} \tag{34}$$

where Γ is the strength of the two-magnon scattering (units are Oe) and $f_0 = 2\gamma M_{\mathrm{eff}}$. This linebroadening type reveals itself when $\Delta H(f)$ data features a curvature.

[28] R.D. McMichael and P. Krivosik, *IEEE Transactions on Magnetics* **40**, 1 (Jan. 2004), pp. 2–11

[29] J. M. Lock, *Brit. J. Appl. Phys.* **17**, 12 (1966), p. 1645

[30] R. Arias and D. L. Mills, *Phys. Rev. B* **60**, 10 (1999), pp. 7395–7409, B. Heinrich, J. F. Cochran, and R. Hasegawa, *J. Appl. Physics* **57**, 8 (1985), pp. 3690–3692

[31] D. L. Mills and R. Arias, *Physica B* **384**, 1-2 (2006), pp. 147–151

Out-of-plane configuration (OP)

The resonance condition again follows eq. 25, but with **H** and **M** oriented perpendicularly to the sample surface. The LLG-equation gives a different set of coupled equations for the components M_x and M_y[32], that lead to the solution:

[32] B. Heinrich and J. A. C. Bland, *Ultrathin Magnetic Structures II* (2006)

$$\mathfrak{B}_{\mathrm{eff}} = H\cos(\theta_{\mathrm{M}}-\theta_{\mathrm{H}}) - \left(4\pi M_{\mathrm{eff}} + \frac{2\left(K_{\mathrm{U}}^{\shortparallel}-K_1^{\perp}\right)}{M_{\mathrm{s}}}\right)\cos 2\theta_{\mathrm{M}} \tag{35}$$

$$\mathfrak{H}_{\mathrm{eff}} = H\cos(\theta_{\mathrm{M}}-\theta_{\mathrm{H}}) - \left(4\pi M_{\mathrm{eff}} + \frac{2\left(K_{\mathrm{U}}^{\shortparallel}-K_1^{\perp}\right)}{M_{\mathrm{s}}}\right)\cos^2\theta_{\mathrm{M}} \tag{36}$$

Now, analogously to $K_1^{\perp}$ in the IP configuration, in the OP case both the in-plane fourfold $K_1^{\shortparallel}$ and in-plane uniaxial anisotropy $K_U^{\shortparallel}$ have negligible effect, leading to:

$$\mathfrak{B}_{\mathrm{eff}} = H\cos(\theta_{\mathrm{M}}-\theta_{\mathrm{H}}) - \left(4\pi M_{\mathrm{eff}} - \frac{2K_1^{\perp}}{M_{\mathrm{s}}}\right)\cos 2\theta_{\mathrm{M}} \tag{37}$$

$$\mathfrak{H}_{\mathrm{eff}} = H\cos(\theta_{\mathrm{M}}-\theta_{\mathrm{H}}) - \left(4\pi M_{\mathrm{eff}} - \frac{2K_1^{\perp}}{M_{\mathrm{s}}}\right)\cos^2\theta_{\mathrm{M}}. \tag{38}$$

In the case of $\mathbf{M} \parallel \mathbf{H}_0$ with $\theta_M = \theta_M \equiv \theta$, $\mathbf{H}_0$ perpendicular to the sample plane and thus $\cos\theta_M = 0$ one obtains from eqs. 25, 37 and 38, and $H \to H_{res}$:

$$f(H_{res}) = \frac{\gamma}{2\pi}\left(H_{res} - 4\pi M_{eff} + \frac{2K_1^{\perp}}{M_s}\right) \tag{39}$$

The OP fit cannot distinguish between the two summands in eq. 39 containing M_{eff} and $K_1^{\perp}$, since they both contribute linearly. Thus the unseparated sum is labeled $M_{eff}^{\perp}$, which contains $K_1^{\perp}$ and is the output of the fit to the FMR measurement. The separation of a usually negligible $K_1^{\perp}$ is accomplished by comparing $M_{eff}^{\perp}$ with M_{eff} from IP measurements. For a polycrystalline film one would expect $K_1^{\perp} = 0$, but in the case of a strong texture there might be a contribution to $K^{\perp}$ by an mixed-averaged magnetocrystalline anisotropy[33]. $K_U^{\perp}$ is separated from M_{eff} by measuring M_s via BHLooper or VSM. Thickness-dependent IP measurements help to separate interface from bulk contribution of $K_U^{\perp}$ after eq. 32.

[33] U. F. Kocks, C. N. Tome, and H.-R. Wenk, Texture and Anisotropy, Cambridge University Press, 2000

Quenching of the 2M contributions in the OP FMR configuration[34] leads to a simplified expression of eq. 33 for the OP linebroadening

[34] R. Arias and D. L. Mills, *Phys. Rev. B* **60**, 10 (1999), pp. 7395–7409

$$\Delta H_{\perp} = \frac{4\pi\alpha}{\sqrt{3}\gamma} f + \Delta H_{0,\perp} \tag{40}$$

The superscripted symbols $_{\parallel}$ and $\perp$ for α will be used to indicate the used measurement configuration (in theory these quantities are the same).

FMR setup

The FMR system comprises a custom made coplanar microwave guide designed by Prof. Tim Mewes at the University of Alabama[35] and a RF source that generates up to 40 GHz. The RF signal is fed into a coplanar waveguide[36] which creates an RF magnetic field parallel to the thin film surface. The static field $\mathbf{H}_0$ is generated by an electromagnet (up to 12 kOe). A Gaussmeter is used to monitor the external magnetic field. The samples will be measured in saturation. The magnet is closed-loop-controlled with a LabView program. A lock-in amplifier and Helmholtz-modulation coils[37] are used to superpose a small alternating magnetic field ($\sim$10 Oe) over $\mathbf{H}_0$ in order to increase *signal to noise ratio* (SNR) via the lock-in method[38]. The setup is sketched in fig. 8. The FMR output is the derivative of the absorbed power, i.e. the imaginary part of the magnetic susceptibility $d\chi''/dH$, and is fitted to an asymmetric Lorentzian, which takes coupling between the sample and the waveguide into account[39]. Data points can be collected for in- and out-of-plane geometry ($_{\parallel}/\perp$). $z = 0$ is the sample plane.

[35] homepage

[36] Y. Ding, T. J. Klemmer, and T. M. Crawford, *J. Appl. Physics* **96**, 5 (2004), pp. 2969–2972

[37] S. S. Kalarickal et al., *J. Appl. Physics* **99**, 9, 093909 (2006)

[38] ThinkSRS, Lock-in detection method, 2010 (accessed Sept. 30)

[39] G. Woltersdorf, link, PhD thesis, 2004

A special in-plane holder was designed as part of this work that allows for angular dependent in-plane measurements, see fig. 9. The complete holder is fixated onto the FMR electromagnet mount. The specimen is

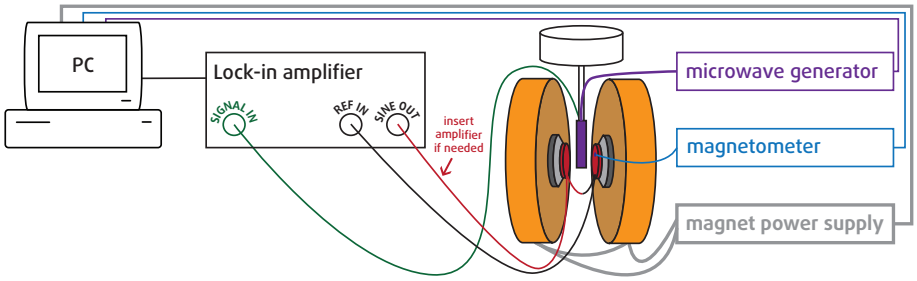

Figure 8: FMR setup used for the experiments.

then taped with its backside onto the sample stamp. After attaching the waveguide mount to the waveguide via teflon screws, this stamp then gently presses the sample onto the waveguide due to an integrated spring and allows for rotation without losing direct contact. The in-plane holder can be retracted via a ball bearing slide to move it out of the way if not needed when using the system for regular in- or out-of plane measurements.
The data collection is set up to be fully automated and the formulas introduced on page 21 are fitted to the data via MatLab routines. The whole system has been set up and the control and measurement programs have been written during the preparation of this work.

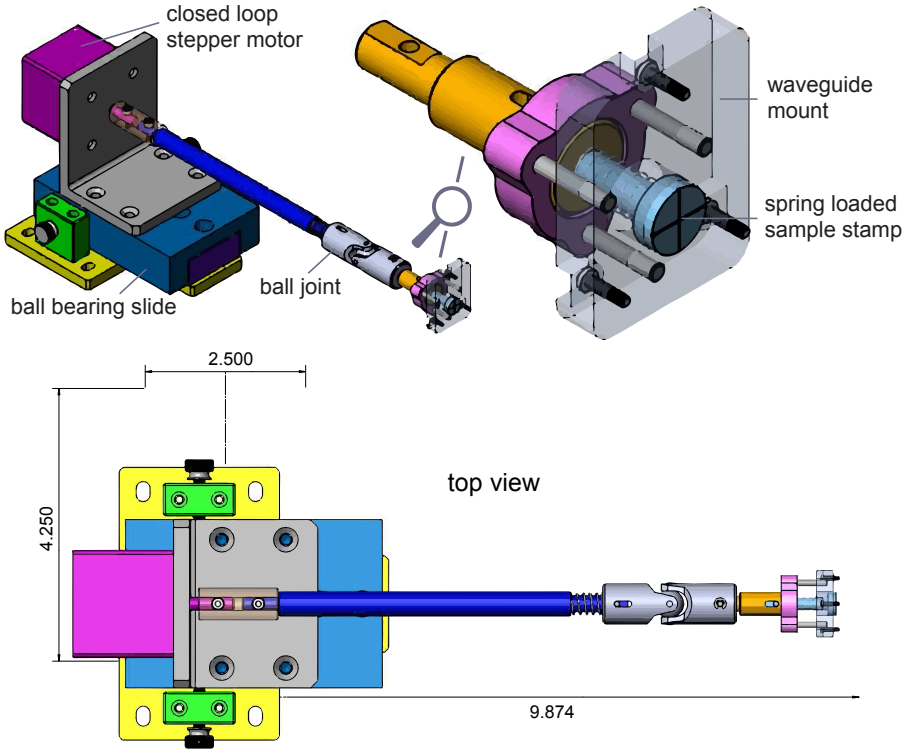

Figure 9: FMR in-plane rotational add-on that is attached to the magnet mount via a base plate (yellow). A closed-loop stepper motor (purple) on a slidable ball bearing stage controls the rotation that is translated via a aluminum rod (blue). A ball joint (blue-gray) accepts minor positioning offsets, prevents jamming and connects it to the head (magnified on the top right). The thin film sample is attached to a spring loaded stamp (light blue) via double sided tape. Then the head is connected to the waveguide via the waveguide mount (gray). The spring behind the stamp guarantees that the sample is always in contact with the waveguide during the rotation as it presses it gently onto it. Numbers are in inches.

AFM

Atomic force microscopy (AFM) is a type of *scanning probe microscopy* (SPM) and it measures forces between a sharp probe (radius is less than 100 Å; supported by flexible cantilever, see fig. 10) and surface atoms at a distance of $\sim$1 nm. A laser is reflected on the cantilever to record the motion of the probe, which can be plotted versus its position in a pseudocolor image. *Surface texture* describes the repetitive or random deviation from a flat surface that forms a 3D topography and is not to be confused with *crystallographic texture*, which addresses the distribution of crystallite orientation. Surface texture can be separated into *roughness* and *waviness*, where the latter describes long range fluctuations. Waviness can be evaluated via a length that expresses profile changes where the shorter roughness characteristics are filtered out. This can be achieved via Fourier transformation of the roughness profile. There are different values that measure roughness. Most commonly used are R_z, R_a and R_q that each are illustrated in fig. 11 and defined within a chosen sampling length as:

- R_z: sum of the maximum peak and minimum valley value, measured from the average height line.
- R_a: the arithmetic average of the absolute values of the surface height deviations measured from the mean plane. It is easy to obtain from a surface profile but makes no distinction between peaks and valleys and surfaces with different types of undulations are not distinguished.
- R_q: the root mean square average of height deviation taken from the mean image data plane. R_q is more sensitive then R_a towards outlier values.

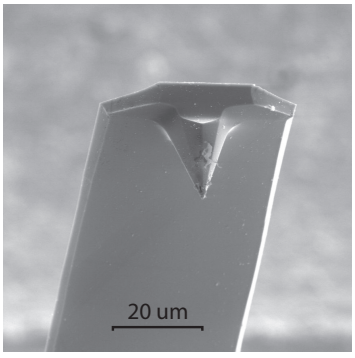

Figure 10: Scanning Electron Microscope image of a typical AFM tip on a cantilever.

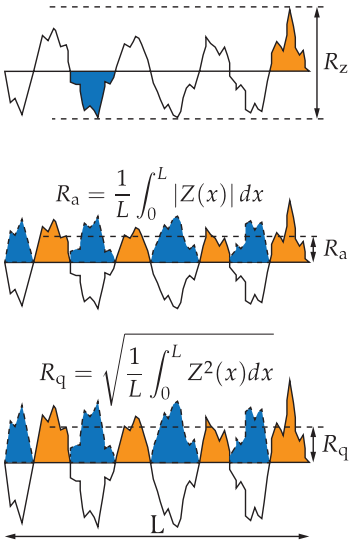

Figure 11: commonly used roughness parameters. Z is height and L is sampling length; further explanation see text.

BHLooper and VSM

A BHLooper measures flux density B versus field intensity H of a magnetic thin film sample. This is achieved by placing the sample into a sense coil, which senses the magnetic flux of the sample and that is connected to a voltage amplifier and a analog/digital converter for data acquisition via PC software. Whole 8″ Si-wafers are loaded into the BHLooper. Two larger Helmholtz coils that generate an external AC magnetic field ($H_{max} = 5$ kOe, $f \approx 1$–100 Hz) are aligned along the same axis as the sense coil. A Hall effect sensor outside of the sense coil is used to read and control the applied field. Following Faraday's law the induced voltage is $U = NA\,dB/dt$, where N is the number of turns and A is the cross-sectional area of the sense coil. Therefore, integrating $U(t)$ over time t gives the magnetic flux density B.
A *vibrating sample magnetometer* (VSM) also uses electromagnetic induction to measure the magnetization of a sample and it consists of an electromagnet ($H_{max} = 17.5$ kOe), a vibration unit with a quartz glass

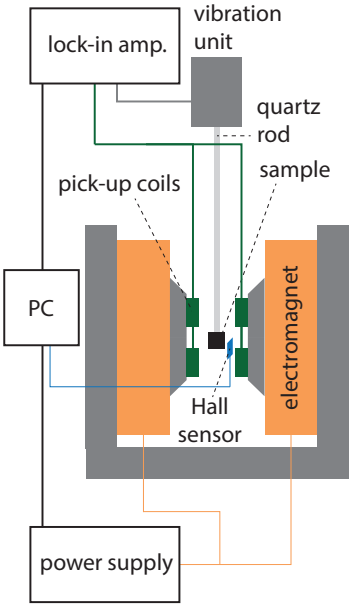

Figure 12: typical VSM setup.

sample holder, two small Helmholtz pick-up coils in proximity to the sample and a field sensor, see fig. 12. The sample with $A \approx 10\text{x}10\ \text{mm}^2$ is placed in the center of the electromagnet and vibrates perpendicularily to the applied field. This induces an electromagnetic field E in the pick-up coil and $E = 3/2 K \mu_0 M_s f$, where f is the frequency and K is an instrument factor which is determined with a calibration measurement of a standard sample. The output of the VSM is therefore a MH-loop - in contrast to the BHlooper.

MOKE

The *magneto-optic Kerr effect* (MOKE) is the change of the polarization of light when reflected from a magnetized surface. The effect arises from the off-diagonal components of the dielectric tensor which leads to an anisotropy of permittivity in the magnetic material. Therefore, the speed of light depends on the direction and causes a change in polarization. Linearly polarized light becomes elliptically polarized and the rotation of the plane of polarization is sensed with a polarizer. MOKE can be divided into different geometries that are defined by the direction of the magnetization, i.e. *longitudinal*, *transversal* and *polar*. The magnetization is measured by a laser and the wafer can be mapped, allowing for the investigation of gradient wafers. The longitudinal MOKE at WD measures the magnetization which is parallel to the surface and the plane of incidence.

ANELVA sputter system and experimental methods

ANELVA sputter system

The ANELVA Sputter system is comprised of a cluster of UHV module. All Heuslers and Ag are sputtered from 4″confocally arranged targets in a chamber with no stage heating capabilities. All the other materials are in chambers that utilize 6″targets. Cr, Ti, MgO and IrMn are in chambers that allow for stage heating. The base pressure of the system is typically $p_{\text{base}} \leq 3 \cdot 10^{-9}$ torr. In-situ thermal treatment without breaking the vacuum is performed with a heating chamber ($p_{\text{base}} \leq 8 \cdot 10^{-9}$ torr; 500°C max) and a *rapid transfer annealing* (RTA) chamber ($p_{\text{base}} \leq 2 \cdot 10^{-9}$ torr; 700°C max). Other modules are a cryogenic cooling and an ion-sputter etching chamber. All chambers are connected via a fully automated transfer system that is designed for processing 8″wafers. RTA allows for in-situ shot anneals with ramp times below 60 s and is *proportional-integral-derivatively* (PID) controlled.
DC (co-)sputtering of up to three targets is possible in the main chamber. The stage has no heating capabilities. However, the chambers equipped with other elements/compounds used in this work allow for substrate heating. Three types of substrates have been utilized within the scope of this work:

Si/SiO_2: 8″thermally oxidized Si wafers with typically 300 nm thermal oxide. Si-wafers are comparably cheap and are preferred for high throughput investigation purposes. Ultimately it is the goal to transfer results from Si/SiO_2 onto AlTiC wafers.

AlTiC: Aluminium Titanium Carbide is a high price industrial standard substrate for e.g. *hard disk drive* (HDD) read head fabrication. Before the deposition of the sensor film the 8″AlTiC wafer is plated with an ultra-smooth semi-amorphous ∼2 µm thick permalloy (Py, a NiFe compound) film, that will later act as a magnetic shield in the device. The small Py grains prevent magnetic domain formation and effectively shield unwanted external stray fields. The wafer is then treated with *Chemical Mechanical Processing* (CMP) to obtain a roughness of about 5 Å.

(001)-MgO: 1x1 cm^2 sized single side polished monocrystalline MgO substrates with a (001) crystal orientation. These are popular sub-

strates for epitaxial growth of a manifold of materials, including Heuslers. In order to enable the system to handle the MgO substrates, they are placed into a 8″AlTiC carrier with a specifically milled 1x1 cm^2 cutout. However, they cannot be annealed in-situ, since the infrared sensor-based PID control inside the RTA monitors the wafers temperature from their backside and a lack of thermal contact between the carrier and substrate would lead to a temperature overshoot of the latter.

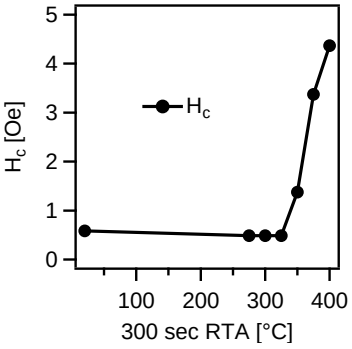

Figure 13: impact of RTA annealing on the AlTiC's Py shield. Recrystallization increases H_c.

[40] O. Gaier et al., *J. Appl. Physics* **103**, 10, 103910 (2008)

[41] N. Tal et al., *J. Appl. Physics* **114**, 16 (2013), p. 163904

Considerations and limits for industrial implementation

The first obstacle is the temperature tolerance of the Py shield concerning annealing. Unfortunately, post-annealing of the device can lead to recrystallization and coercivity H_c increases, see fig. 13. The upper shield temperature limit is about $T_{\mathrm{AlTiC}} = 325°C$ for 10 min in-situ RTA. CMS and $Co_2Fe_{0.4}Mn_{0.6}Si$ (CFMS) both have reported optimal annealing temperatures for increasing $L2_1$ crystallization of $T_a \geq 400°C$[40] on Cr buffer and $T_a \geq 450°C$ for deposition on MgO[41]. However, these studies were utilizing single crystalline MgO substrates and we will find that XRD peaks will reveal ordering at lower temperatures and M_s will show values close to bulk when annealing the films at temperatures not significantly higher than 325°C on amorphous substrates with appropriate seed and buffer layers.

Wafer temperature

Due to the incapability of heating in the main chamber during deposition it is necessary to develop process routes which only include in/ex-situ post-annealing. Preheating the wafer prior to transfer into the main chamber is also possible. The thermal response of both AlTiC- and Si-wafers is very different, which is an issue concerning reproducibility and the transfer times for each type of substrate has to be taken into account. There is calibration data available for the cooling of AlTiC but not for Si wafers. Furthermore one has to distinguish between lightly and heavily doped silicon. Both feature different emissivity spectra, which will determine their temperature evolution. Supposing that the wafer has been heated up until the set point of the RTA/heating chamber, one can connect the Stefan-Boltzmann law with the rate of heat flow via a differential equation to determine the cooling during transfer:

$$\rho c D \frac{dT}{dt} = -E_{\mathrm{eff}} \sigma T^4 \tag{41}$$

where ρ in $[g/cm^3]$ is the wafer density, c specific heat capacity in $[Jg^{-1}K^{-1}]$, E_{eff} the coefficient describing the efficiency of power loss by thermal radiation (total emissivity), D the wafer thickness and σ the Stefan-Boltzmann constant. Solving eq. 41 by separating variables and

then decomposing it into partial fractions, one obtains the solution

$$\frac{1}{4}\left[\ln\left(\frac{T+T_1}{T-T_1}\right)-\ln\left(\frac{T_0+T_1}{T_0-T_1}\right)+2\tan^{-1}\left(\frac{T}{T_1}\right)-2\tan^{-1}\left(\frac{T_0}{T_1}\right)\right]=\frac{E_{\text{eff}}\sigma}{\rho c D}T_1^3 t \tag{42}$$

with T_0 and T_1 being the initial temperature of the wafer and the chamber temperature (usually 14°C), respectively. When plotting temperature versus time $T(t)$, one obtains a cooling curve of the wafer which will help to estimate the desired transfer time just before starting deposition with a specific temperature or to just estimate the temperature after a given cool-down time. Here, thermal conduction through the transfer arm and stage pins of the sputter tool is neglected. The only unknown coefficient in eq. 42 is E_{eff}, which is obtained for the AlTiC wafer by fitting cooling calibration data. This gives $E_{\text{eff}} \cong 0.5$ (with $\sigma_{\text{AlTiC}} = 750\ \text{Jkg}^{-1}\text{K}^{-1}$) see fig. 14. This value is a combination of the

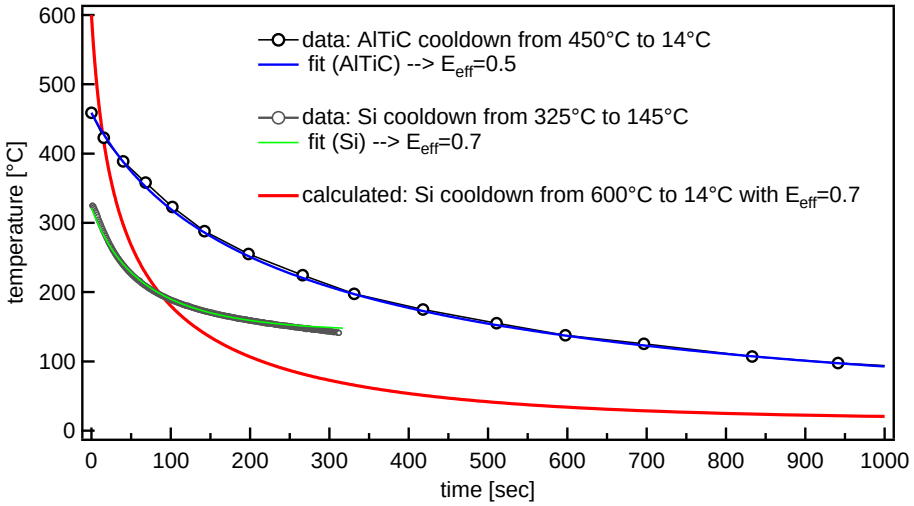

Figure 14: cooling curves of Si/SiO_2 and AlTiC wafers with fits and plots following eq. 42.

front and the back of an empty wafer. To obtain an estimate for E_{eff} of Si, an empty Si/SiO_2-wafer is heated up in the RTA up until 325°C. Then the RTA is shut off and the temperature development of the wafer is recorded. The data is then fitted to eq. 42, where E_{eff} is, aside from all the other known constants on the right hand side of the equation, determining the curvature. T_1 resembles the asymptote of the curve, which in this case is about 145°C - the temperature of the RTA chamber. This approach gives $E_{\text{eff}} \approx 0.7$ for Si (with $\sigma_{\text{Si}} = 700\ \text{Jkg}^{-1}\text{K}^{-1}$), see fig. 14. Reports for highly doped silicon support this value[42]. Therefore, this value is used for creating the $T(t)$ curve for Si/SiO_2-wafers which will help to estimate the wafer temperature at any given transfer time.

[42] P. J. Timans, *J. Appl. Physics* **74**, 10 (1993), pp. 6353–6364

Gradient wafer deposition

The ANELVA sputter system provides the possibility to turn off rotation during deposition. In the case of a single (composite) target this allows for the deposition of a thickness wedge. A small compositional change

due to different path lengths of the sputtered particles to the wafers are neglected here[43]. Co-sputtering from multiple targets on the other hand will lead to a combined composition *and* thickness gradient since sputter rates from each target generally differ. In this case it is not possible to fabricate compositional gradients without a featured thickness wedge. However, an optimal target configuration will allow for the minimization of this drawback, i.e. it is recommended to arrange the targets circularly equidistant to each other to minimize the thickness gradient.

[43] XRF measurements on several samples (not shown here) proved that the target distance as a parameter indeed has negligible impact on the film composition for the materials and pressure ranges under investigation here.

The composition of the films is measured via XRF as explained on page 20. Additionally, *Rutherford backscattering* (RBS) data from stoichiometric films is used to calibrate in-house XRF data. For the compositional gradient wafers it is impractical to measure multiple spots on the 8″wafers, since (a) the contracted RBS measurements are expensive and (b) in-house XRF takes multiple hours if the spot size is reduced to a feasible diameter of 1 cm. Furthermore, the calibration for XRF is spot-size dependent: the commonly used diameter of 3 cm results in a different background signal than for 1 cm. Therefore the local composition $c_j(x, y)$ [at%] of an element j across the wafer will be estimated based on the following framework:

1. The composition and thickness of the gradient wafer is calculated based on calibrated local deposition rates that will be established for each target and stage position.
2. The center point of the gradient wafer has the same composition and thickness as a thin film sample deposited with activated rotation. Therefore the latter will be sent to RBS and the results will be used to reference the center point of the gradient wafer.
3. the deposit of each target has the same density and composition as the target and differential sputter rates will be neglected.

In the case of a single phase crystalline target i made up of j different elements one can express its density as

$$\rho_i = \frac{\sum_{uc} N_{i,j} A_j}{V_i^{(uc)} N_A} \tag{43}$$

where $N_{i,j}$ are the atoms of type j per unit cell of the target compound i, A_j is the relative atomic mass of element j, $V_i^{(uc)}$ is the volume of the unit cell of target material i and N_A is Avogadro's constant. It should be noted that this expression is precise only for targets with homogeneous density ρ_i.

It is now important to realize that in the case of a co-sputtering process it would be wrong to simply add the deposition rates of each target. The deposit of low density targets such as Al contains less atoms per thickness than denser materials. By simple addition of deposition rates, their contribution would then be overestimated and Al therefore would

be underpopulated in the final Heusler phase. Instead, it has to be calculated how many atoms of element j in relation to all other atoms reach the substrate. $d_i(x,y)$ is the *local deposition rate* of target i with respect to the wafer coordinates x and y, where $(0,0)$ describes the center of the substrate. Now $d_i(x,y)\cdot N_{i,j}/V_i^{(uc)}$ is the rate of atoms of element j that are deposited on the substrate [$s^{-1}cm^{-}2$], coming from target i. And the total rate for atoms reaching the substrate from target i is $d_i(x,y)\cdot N_i/V_i^{(uc)}$, with $N_i = \sum_{uc} N_{i,j}$ being the total number of atoms in the unit cell of the compound of target i. Therefore, the at% of element j in the film only from target i are

$$c_{j,i}(x,y) = \frac{d_i(x,y)\cdot N_{i,j}/V_i^{(uc)}}{d_i(x,y)\cdot N_i/V_i^{(uc)}} = \frac{N_{i,j}}{\sum_{uc} N_{i,j}} \tag{44}$$

which is unsurprisingly the same composition as for the target. Extending this approach to multiple targets with individual phases and thus different $V_i^{(uc)}$ leads to the elemental composition of the co-sputtered film

$$c_j(x,y) = \frac{\sum_i d_i(x,y)\cdot N_{i,j}/V_i^{(uc)}}{\sum_i d_i(x,y)\cdot N_i/V_i^{(uc)}} \tag{45}$$

Assuming furthermore a linear correlation between sputtering power P_i and deposition rate, which is a first order approximation, allows us to use a calibrated deposition rate $\tilde{d}_i$ at power $\tilde{P}_i$ for each target i so that eq. 46 becomes

$$c_j(x,y) = \frac{\sum_i \frac{\tilde{d}_i(x,y)}{\tilde{P}_i} P_i\cdot N_{i,j}/V_i^{(uc)}}{\sum_i \frac{\tilde{d}_i(x,y)}{\tilde{P}_i} P_i\cdot N_i/V_i^{(uc)}} \tag{46}$$

The calibrated deposition rate $\tilde{d}_i$ can be derived from a normalized local deposition rate $\lambda_i(x,y) = \tilde{d}_i(x,y)/\tilde{d}_i(0,0)$ [%], specific for target i. A reference sample is created by sputtering from target i with no rotation and $\lambda_i(x,y)$ values are obtained via XRR mapping, see fig. 15. Generally, sample thickness can be extracted either via AFM step height measurements or XRR. XRR scans are preferred here since it is possible to map the wafer fully automated with multiple scanning points. The local deposition rate from target position i for any installed target is then simply the calibrated and normalized local deposition rates times the uniform regular deposition rate from a rotating sample, i.e. $\tilde{d}_i(x,y) = \lambda_i(x,y)\cdot\tilde{d}_i$.

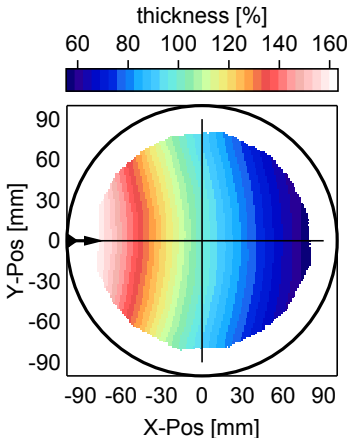

Figure 15: thickness measurements via XRR on reference wafer used for the gradient wafer calculations. The arrow indicates the position of the target, in this case Fe.

Seed layers and texture

The main task for the thin film experimentalist is to control all different stages of layer growth. Nucleation is influenced by the energetic surface conditions at the start of deposition and it defines how the subsequent atomic arrangement will develop, e.g. the direction of the crystal unit cell or a specific 2D/3D growth mode. This perspective suggests that the initial stage of thin film growth is ultimately determining the final result and therefore demands careful preparation and highest attention. When growing polycrystalline materials onto amorphous substrates such as Si/SiO_2, recrystallization through e.g. annealing will not reorient the deposited crystallites, contrary to the use of single crystalline substrates, such as (001)-MgO, which will act as a template and render recrystallization possible.
Standard scientific approach towards exploiting the properties of various materials is high quality epitaxial growth. However, standard industrial production typically uses semi-amorphous substrates (polycrystalline with amorphous separation layer, e.g. *am.*-Ta) and the transfer of results from epitaxial samples is deemed tough. A change of substrate will alter experimental conditions and thus will shift the thin film growth optimum regarding parameter space. Utilizing differing laboratory frameworks is the most prominent reason for the variation of experimental results for *magnetoresistance* (MR) utilizing Heusler materials as *ferromagnetic* (FM) layers in *spin-valves* (SV) and MTJs.
A few concepts of thin film growth have to be taken into account in order to plan the choice of seed and buffer layers and to generally understand the crucial variables of the experiment. The *structure zone model* and *Ehrlich-Schwöbel barrier* will be explained in the oncoming next sections, which will elucidate some important aspects in the growth evolution of thin films.

Structure zone model

Ultimately, the final texture depends on the orientation of the nuclei at the early growth stage. This can be understood by considering the extended *structure zone model* (SZM) and the impact of faceting on the evolution of texture. *Mahieu et al.*[44] gives a good overview for the zones used in the SZM. It essentially categorizes thin films growth types by the fundamental dependency of their main driving parameters on surface conditions. These are *sticking coefficient*, *surface mobility*,

[44] S. Mahieu et al., *Thin Solid Films* **515**, 4 (2006), pp. 1229–1249

[45] P. Hartman and W. G. Perdok, *Acta Cryst.* **8**, 1 (Jan. 1955), pp. 49–52

[46] H. Huang, G. H. Gilmer, and T. Díaz de la Rubia, *J. Appl. Physics* **84**, 7 (1998), pp. 3636–3649

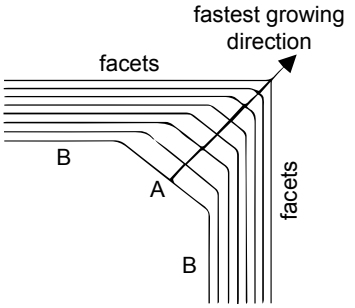

Figure 16: schematic evolution of crystallographic plane growth. Plane A has a higher growth rate than B, which creates a B-faceted grain.

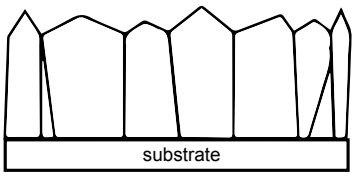

Figure 17: faceted, columnar and random texture of zone *Ic* growth.

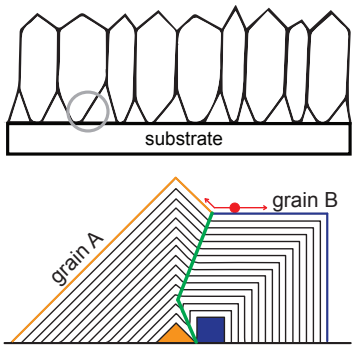

Figure 18: zone *T*, (top): anisotropy in growth rate leads to V-shaped and facetted columns. This is possible because of allowed intergranular diffusion and grain growth competition; (bottom): magnification of the gray circled region from the top sketch, where an adatom (red) is able to diffuse from grain B (blue line) to grain A (orange line). Both grains grew from differently oriented nuclei (blue and orange) which are however terminated by the same facets, giving A the faster perpendicular growth rate. A grain boundary is formed in the process (green).

re-sputtering and *impurities*. The first two generally depend on:

- *temperature*, often given as ratio of substrate temperature to melting point T_s/T_m;
- *deposition rate*, which can *trap* and *bury* adatoms and therefore counteract the mobilizing effect of temperature;
- *kinetic energy* of the impinging particles;
- *nearest neighbors*: the larger the number of dangling bonds (or nearest neighbors) - the higher the sticking coefficient[45]. Thus the adatom mobility is inversely proportional to the number of nearest neighbors as an increasing potential well reduces the mobility on a specific crystallographic plane[46]. This results in a perpendicular growth anisotropy for different planes. This concept is also applicable to vacancy diffusion and will be important for defining the Ehrlich-Schwöbel barrier later.

The structure zones are labeled *Ia*, *Ib*, *Ic*, *T* and *II*, with an increase of thermal energy in that order. Faceting starts in zone *Ic*, where thermally induced mobility enables adatoms to nucleate by overcoming the diffusion barrier E_{diff}, allowing the adatom to move across different types of surface planes. Then, from a geometrical argument, grains will be terminated by planes providing highest adatom mobility and thus lowest crystallographic growth rate, see fig. 16. Because the mobility is not high enough to allow for diffusion from grain to grain, no competitive overgrowing takes place and the final film in the *Ic* zone consists of randomly oriented columns separated by grain boundaries with a faceted termination, see fig. 17.

Preferential orientation can be found in zone *T* and higher, where inter-granular diffusion leads to overgrowing, as depicted in fig. 18. This can be understood in the following way: imagine a set of randomly oriented nuclei that are already fully faceted, with the result that now all of these nuclei are terminated with the same facet type which featured the slowest growth rate. Geometrically, the fastest growth rate perpendicular to the substrate is now dominated by facets that are tilted towards the substrate plane. The most tilted facets thus will overgrow the flat ones. V-shaped faceted, polycrystalline columns are created and a change of texture with increasing thickness is possible. Zone *T* is generally active in the temperature interval $0.2 < T_s/T_m < 0.4$[47], while zone *II* is above $0.4T_m$.

Ag as an example crystallizes fcc and the plane with the highest packing density and lowest surface energy is (111), which makes it the fastest growing plane. Therefore, following the SZM, the [111] direction is the generally preferred orientation in zone *T* which is within $250-500$K for Ag ($T_m = 1235$K). The high Ag-adatom mobility can be reduced e.g. by introducing monolayers of Sn[48]. This however can sacrifice preferential orientation. Cr crystallizes bcc, wherefore the [011] is the fastest growing plane and (011) the preferred orientation for Zone *T* which is within

about 440−1100K for Cr ($T_m = 2180$K). For Cr however, (001)-texture can be achieved within this temperature range. This is due to another mechanism, which leads to a preferential (001) island formation over (011), wherefore overgrowing by (011) is simply prevented by a lack of such islands before impingement. The reason for preferred (001)-oriented nucleation is because as increasing temperature is promoting surface diffusion, the critical size of nuclei is drastically increased while their formation rate is decreased. The Cr film thus maintains an islandlike character with increasing thickness. The total surface energy for equiaxed islands is then minimal if the (001)-plane is parallel to the surface while (011) with minimal energy covers the sides[49]. The same argument holds for Ag thin films, where island agglomeration within zone T is even more drastical. In the case of Ag, (001)-oriented nuclei with (111) sides are actually prominent before coalescence[50] and (111)-texture will dominate only for thicker films due to overgrowth. The main problem of manufacturing ultrathin (001)-textured Ag films is heavy 3D-island growth which calls for surfactant materials, like Ti[51], which will be discussed later.

[47] P.B. Barna and M. Adamik, *Thin Solid Films* **317**, 1-2 (1998), pp. 27–33

[48] A. Romanyuk et al., *Surf. Sci.* **602**, 9 (2008), pp. L49–L52

[49] Y. C. Feng, D. E. Laughlin, and D. N. Lambeth, *J. Appl. Physics* **76**, 11 (1994), pp. 7311–7316

[50] Y. S. Jung, *Appl. Surf. Sci.* **221**, 1 (2004), pp. 281–287

[51] A. Romanyuk et al., *Surf. Sci.* **602**, 9 (2008), pp. L49–L52

Ehrlich-Schwöbel barrier

Essentially the SZM is the result of how adparticles and vacancies occupy energetic states on the thin film surface with respect to geometric boundary conditions, such as terrace dimensions or step facetting. When an adatom (it can also be an ion or molecule) arrives at the surface with kinetic energy E_{kin}, it is confronted with a periodic set of potentials of the neighboring atoms. By overcoming the diffusion barrier E_{diff} that is specific to the surface material the adatom achieves mobility. However, at the edge of a terrace the energy potential is distorted and the adatom has to overcome an additional barrier in order to descend or ascend the step. It is termed *Ehrlich-Schwöbel barrier*[52] E_{ES} and is defined as the difference between the activation energy to overcome the step edge potential wall E_B and the diffusion barrier E_{diff}, i.e. $E_{ES} = E_B - E_{diff}$, see fig. 19. In the case $E_{diff} < k_B T < E_B$ diffusion between existing nuclei/terraces is blocked which results in 3D growth and island formation. E_{ES} is active for both adatoms and vacancies and generally has different values for both. The nature of inter-atomic forces on surfaces is however complicated and the dominance of adatom or vacancy transport is difficult to predict[53]. When discussing island formation it also has to be taken into account that islands themselves can diffuse on the surface[54].
Taking these considerations into account leads to the conclusion that both structure and surface morphology of a thin film are determined in the very beginning of the growth and therefore highly dependent on the underlayers.

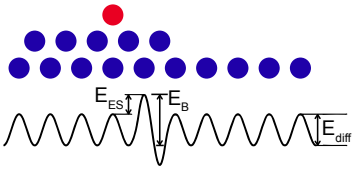

Figure 19: Ehrlich-Schwöbel barrier for an adatom (red) at a step edge.

[52] G. Ehrlich and F. G. Hudda, *J. Chem. Phys.* **44**, 3 (1966), pp. 1039–1049

[53] M. I. Haftel, *Phys. Rev. B* **64** (12 2001), p. 125415

[54] J. Heinonen et al., *Phys. Rev. Lett.* **82** (13 1999), pp. 2733–2736

Controlling and tuning texture

For the sake of simplicity, stacks will have the following nomenclature throughout this thesis: [...]xA/yB/zC[...], where x, y, z are the individual thicknesses in Å of the respective materials A, B, C. The substrate type will be noted on the left hand side of the stack. Annealing steps and other deposition parameters will be denoted in each individual case.
There are numerous reports on seed and buffer[55] layer combinations that promote textured growth of Heusler compounds. The first reported oriented CMS thin films had a (011)-texture obtained with a V seed[56]. However, only the (001) interface preserves half-metallicity of CMS[57], which explains the generally higher TMR for this orientation. For GMR, the (001)-orientation can serve for a better interface and band structure matching and can thus lead a higher MR due to an increased interface spin-scattering asymmetry γ (see *CPP-GMR* section)[58], especially when choosing Ag as spacer material[59]. This created the need for (001)-textured films on amorphous substrates. The control of the (001)-textured Heusler growth is therefore a necessary step for a successful integration into a TMR or CPP-GMR device.
Roughly within the last 20 years, research on controlled textural growth of (001)-FePt for high *perpendicular magnetic ansiotropic* (PMA) recording media lead to the discovery of a variety of seed and buffer materials for ultrathin films. It was found that 20–200 Å MgO seed layers on glass substrates would generate the best (001)-texture[60] (apart from epitaxial growth). Other efforts include oxidized NiTa seeds[61].
CrRu as seed has been reported to introduce a high PMA of 1.8 Merg/cc for (001) FePt films[62] and 2.2 Merg/cc for CoCrPt:C granular media[63]. There are also reports on preparing TiN for (001)-texture of Heuslers (CMS[64]). However, the (001)-texture can also be achieved with Cr on glass substrates and adjusted sputter parameters.
Here, a variety of different seed combinations is investigated where the resulting texture is monitored via the crystalline quality of a Cr *detector* layer ($a_{\mathrm{Cr}} = 2.88$ Å), which can later be used as a buffer for the Heusler layers. The amount of (hkl)-texture is quantified by a normalized relative *texture quality factor* $Q^{\mathrm{T}}_{\mathrm{hkl}}$, which helps to quantify the results within this work:

$$Q^{\mathrm{T}}_{\mathrm{hkl}} = I_{\mathrm{hkl}} \cdot \frac{I^0_{\mathrm{max}}}{I^0_{\mathrm{hkl}}} \cdot t^{-1} [\mathrm{cps/Å}] \tag{47}$$

where I_{hkl} is the integrated measured peak intensity of reflex (hkl), I^0_{hkl} is its theoretical value and I^0_{max} is the theoretical value of the most dominant reflex, i.e. (011) for bcc and (111) for fcc metals. t is film thickness. The scaling to the predominant reflex intensity serves for a better qualitative comparison between e.g. a (011) and (001)-texture of the same material. A higher $Q^{\mathrm{T}}_{\mathrm{hkl}}$ in general denotes a better texture. Since $Q^{\mathrm{T}}_{\mathrm{hkl}}$ serves a relative quantification purpose, its units will be dropped from here on. The following requirements are set upon the

[55] The following differentiation will be made: *seed:* a thin ($t \approx 20$ Å) starting layer that both supports adhesion. It generates varying energetic conditions for adatoms and thus acts as a growth mode catalyst having specific impact on texture, grain size, roughness and ordering. A *buffer* layer is a material, that has a similar projected lattice constant as the adjacent main layer and is used to support its crystallization, wherefore it preferably has to be grown thicker ($t > 100$ Å).

[56] U. Geiersbach, A. Bergmann, and K. Westerholt, *J. Magn. Magn. Materials* **240**, 1-3 (2002), pp. 546–549, S. Kämmerer et al., *J. Appl. Physics* **93**, 10 (2003), pp. 7945–7947

[57] M. Oogane, *ATI and IFCAM International Workshop on spin-currents* **Tohoku University** (2007)

[58] J. Chen et al., *J. Appl. Physics* **117**, 17, 17C119 (2015), Y. Du et al., *Appl. Phys. Lett.* **103**, 20, 202401 (2013), M. Li et al., *Appl. Phys. Lett.* **103**, 3 (2013)

[59] Y. Sakuraba et al., *Phys. Rev. B* **82** (9 2010), p. 094444

[60] L. Lee et al., *Appl. Phys. Lett.* **67**, 24 (1995), pp. 3638–3640, T. Suzuki et al., *J. Magn. Magn. Materials* **193**, 1-3 (1999), pp. 85–88, M. Weisheit, L. Schultz, and S. Fähler, *J. Appl. Physics* **95**, 11 (2004), pp. 7489–7491

[61] T. Maeda, *IEEE Transactions on Magnetics* **41**, 10 (Oct. 2005), pp. 3331–3333

[62] J.S. Chen et al., *J. Magn. Magn. Materials* **303**, 2 (2006), pp. 309–317

[63] Y. Xu, J. S. Chen, and J. P. Wang, *Appl. Phys. Lett.* **80**, 18 (2002), pp. 3325–3327

[64] A. Sugihara et al., *Jap. J. Appl. Phys.* **50**, 2R (2011), p. 028001

development of the seed layers on amorphous substrates:

- Generally deliver optimal thin film properties, such as M_s and damping α, as compared to other (reported) substrates or seed/buffer combinations.
- Provide a strong texture with a reasonable roughness to prevent unwanted pinhole formation or exchange coupling. The latter would effectively disturb the $\perp/\parallel$ configuration of the bottom to top *ferromagnet* (FM_b and FM_t) and have implications on the dynamic response of the device.
- Ultimately present a route to transition from Si/SiO_2 to AlTiC wafers while maintaining the film properties.

Sputter rates λ [Å/s] for $Co_{40}Fe_{40}B_{20}$ (CoFeB), CMS, Cr, $Ir_{20}Mn_{80}$ (IrMn), MgO, Ru, Ta, Ti are 0.7, 0.3, 0.3, 0.1, 0.01, 0.4, 1.2, 0.2 respectively. For all films the substrate temperature T_s is at ambient conditions during deposition, except for Cr and IrMn: $T_s = 185°C$.

High-RA and low-RA seeds

The developed seed layers will be categorized into two types, i.e. by the magnitude of their *resistance area product* (RA): high–RA and low-RA, where the former contain an insulator (MgO) and the latter don't. During the texture investigations of this work it has been confirmed, that Q^T_{001} is largest, when a thin layer of MgO is introduced into the seed. However, ultimately CPP-GMR devices typically have $RA \sim 0.05\ \Omega\mu m^2$, which limits the utilization of oxides within the stack. Both Q^T_{001} and RA sensitively depend on the thickness t_{MgO} of the inserted MgO within the range 0-10 Å. RA vs. t_{MgO} follows an exponential increase[65] and is generally sensitive to the type of material of the adjacent layers. Fig. 20 shows the relation between measured RA and MgO thickness on a double wedge wafer measured by CIPT, with MgO being sandwiched between CoFeB (the purpose of that will be explained later on) and Cr. RA exponentially increases after about four monolayers of MgO, while Q^T_{001} increases linearly. Therefore a trade-off situation presents itself, where high (low) Q^T_{001} leads to high (low) RA, respectively. This situation calls for the development of a seed system free of oxides to obtain the (001)-texture. Conclusively, the following seed layers have been developed within the scope of this work:

(**001**) **high-RA:** Early TMR stacks generally featured $RA \sim 1\ k\Omega\mu m^2$ or higher[66]. Modern TMR devices however exhibit $RA \sim 1\ \Omega\mu m^2$. A thin MgO seed on amorphous substrates generates the (001)-texture for Cr-buffered Heusler. However, from fig. 20 it follows, that the MgO thickness has to be kept below 9 Å for $RA < 0.5\ \Omega\mu m^2$, which is thinner than in the previously cited reports. Of course, a thick MgO seed can be deposited to generate highest Q^T_{001}, but this creates the demand of

stack types:
high-RA → with MgO
low-RA → no MgO

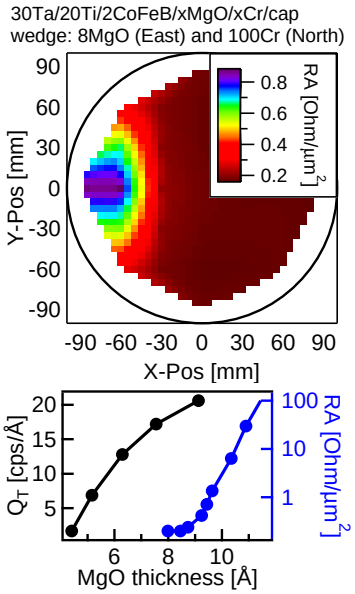

Figure 20: (top): MgO- and Cr-wedge on AlTiC, rotated by 90° to each other. RA sensitively depends on the thickness of the inserted MgO, whereas the thickness gradient of Cr has no influence on the value of RA; (bottom): RA vs. MgO thickness.

[65] S. Yuasa et al., *Nat. Mat.* **3** (2004), pp. 868–871

[66] S. S. P. Parkin et al., *Nat. Mat.* **3** (2004), pp. 862–867

a subsequent thick bottom electrode, i.e. ≈300 Å for a low-ρ material like Ag or Cu. This will result in very thick and rough stacks, which will have detrimental impact on the device performance[67].
All following films are annealed via RTA at 325°C for 600 seconds, unless noted otherwise. In this thesis, 10 Å MgO grown onto a Si/SiO_2-wafer does not lead to any distinct (001)-texture, see fig. 21. Furthermore, there is a MgO-thickness dependence of the magnetization and coercivity of CMS when annealed at rather low annealing temperatures, like 325°C as shown in fig. 22. Providing better adhesion with *amorphous* Ta (*am.*-Ta) seed under the MgO improves the texture only incrementally. A 20 Å Ti seed just before MgO however leads to an increase in Q^T_{001}, see fig. 21. To even further improve the (001)-texture,

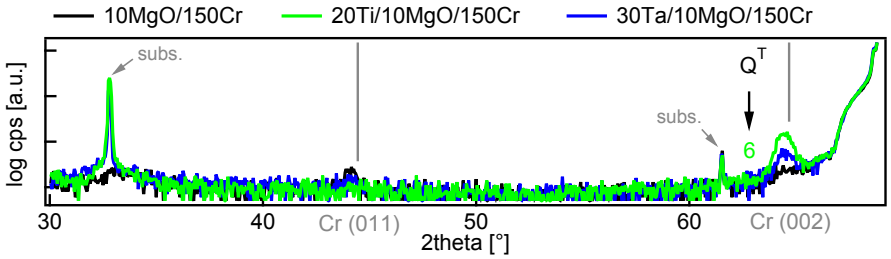

Figure 21: $2\theta/\omega$ XRD scan: a seed layer combination has to be chosen in order to obtain reasonable (001)-texture with an ultrathin 10Å layer of MgO. Films are grown on a Si/SiO_2-wafer. The reflex around 33° is from the substrate.

a CoFeB/MgO combination is introduced. CoFeB is amorphous when deposited at RT, but will start to crystallize when annealed at $T_a > 250$°C, with the optimal temperature ultimately depending on the thickness. MgO is reported to promote the crystallization of CoFe (out of amorphous CoFeB) due to a *template effect*[68], i.e. the formation of nucleation sites for CoFe grains. During the crystallization, Boron will partly diffuse into adjacent layers, but preferably not into MgO[69] (however, elsewhere it has been reported to form Boron oxide[70]). A very smooth and well matched interface between MgO and CoFeB is created with little concentration of B (∼1%) in CoFe[71]. In a seed layer perspective the CoFeB layer acts here as a (001)-volume extension, promoting better (001) growth for the Cr buffer on MgO. Furthermore it prevents the formation of amorphous MgO, which is known for depositing MgO directly onto SiO_2[72]. Thus Q^T_{001} for SiO_2/MgO/150Cr can be increased from 6 to 16 when introducing only 5 Å of CoFeB just before 10 Å MgO (fig. 23), with a proportional effect when using thinner MgO. Additionally, 20 Å Ti or 30 Å *am.*-Ta below CoFeB serve as an adhesion layer for CoFeB and support the annealing-induced template crystallization of CoFeB and MgO. With Ti instead of Ta insertion, Q^T_{001} is further increased by about 50% for t_{CoFeB} =3 Å, see fig. 23. CoFeB is reported to have an amorphization effect on Ti, while exhibiting a reduced crystallization temperature with adjacent Ti[73]. This has two positive effects: (a) better (001) MgO layer thermal stability during hot-Cr deposition due to the extension of amorphous seed (no additional strain exerted

[67] Y. Du et al., *Appl. Phys. Lett.* **103**, 20, 202401 (2013)

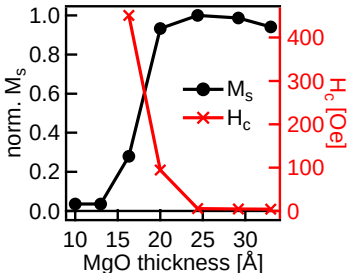

Figure 22: dependence of M_s (normalized to maximal value) and H_c of CMS on the thickness of the MgO seed on Si/SiO_2. For this system, a minimum of about 25 Å MgO is needed for magnetic low temperature crystallization of CMS at 325°C for 600 seconds.

[68] D. D. Djayaprawira et al., *Appl. Phys. Lett.* **86**, 9 (2005)

[69] K. Mizunuma et al., *Appl. Phys. Express* **4**, 2 (2011), p. 023002

[70] J. Y. Bae et al., *J. Appl. Physics* **99**, 8, 08T316 (2006), V. Harnchana et al., *J. Appl. Physics* **113**, 16, 163502 (2013)

[71] C. Y. You et al., *J. Appl. Physics* **104**, 3, 033517 (2008)

[72] S. Yuasa and D. D. Diayaprawira, *J. Phys. D: Appl. Phys.* **40**, 21 (2007), R337

[73] T. Miyajima et al., *Appl. Phys. Lett.* **94**, 12, 122501 (2009)

on MgO from Ti/CoFeB layers below) and (b) improved CoFe-MgO template crystallization. It is reported that Ti also supports (001) orientation for fcc Co/Cu multilayers and the large adhesion energy for Ti[74] promotes a smoother film growth. It is pointed out that CoFeB is non-magnetic if its thickness is below 4.2 Å and shows PMA for the CoFeB/MgO combination in the range [4.2, 12] Å[75]. Because for 6 Å CoFeB its PMA is destroyed at $T_a > 300°C$, the developed CoFeB/MgO seed combination is non-magnetic. Fig. 24 shows the HRTEM image for a Ti/CoFeB/MgO/Cr combination with additional Ag and CMS as successive layers that follow the (001)-texture (in the case of Ag with a 45° in-plane unit cell rotation[76], $a_{Ag} = 4.085$ Å). One can clearly see the smooth and highly ordered CoFeB/MgO combination. The CoFeB- and MgO-thickness dependence of Q^T_{001} is furthermore investigated via thickness-wedges while $RA < 0.6\ \Omega\mu m^2$. The largest $Q^T_{001} = 23.6$ is found for 12CoFeB/10MgO, see fig. 25. Modern *magnetic read and memory* (MRAM) MTJs[77] with up to $RA \sim 1\ M\Omega\mu m^2$ are perfect candidates for the high-RA seed/buffer combinations developed here, which allow for an even thicker MgO seed layer.

[74] H. Chihaya et al., *Solid State Commun.* **128**, 6-7 (2003), pp. 225–228

[75] J. Sinha et al., *J. Appl. Physics* **117**, 4, 043913 (2015)

[76] K. Kyuno et al., *J. Phys.: Condens. Matter* **4**, 22 (1992), p. 5125

[77] J. Jeong et al., *Nat. Mat.* **7**, 10276 (2016)

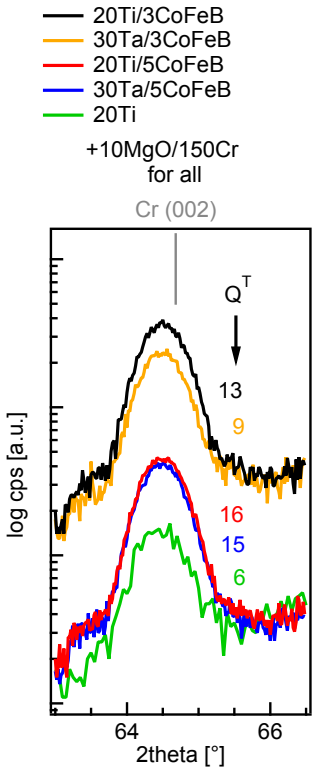

Figure 23: $2\theta/\omega$ XRD scan: the CoFeB combination gives superior Q^T_{001}.

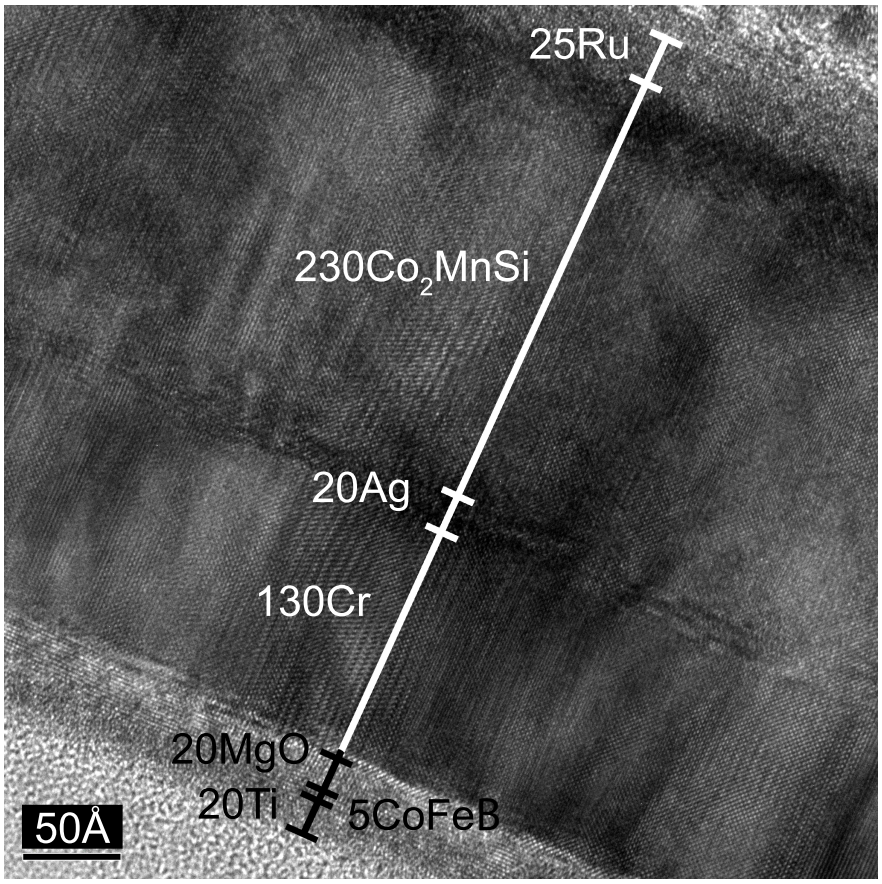

Figure 24: HRTEM cross section of Ti/CoFeB/MgO seed sample promoting strong (001) columnar texture. Numbers are in Å.

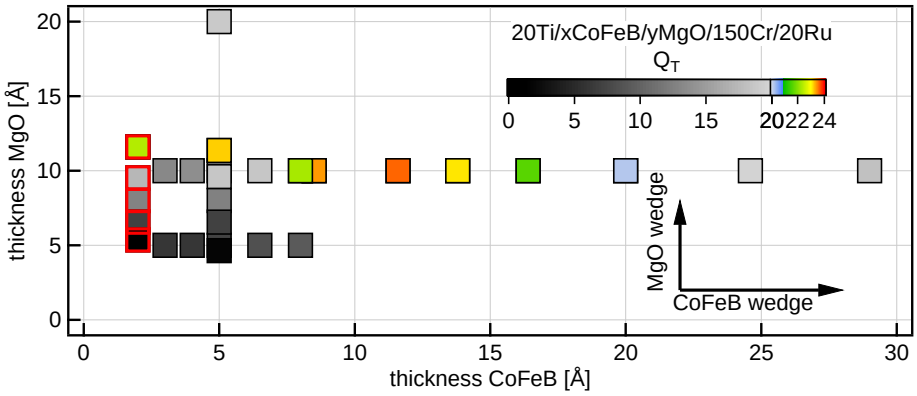

Figure 25: Q^T_{001} of a 150 Å thick Cr film for different CoFeB- and MgO-seed thickness combinations. All films are post-annealed at 325°C for 600 seconds except points with a red outline (2400 seconds). The longer annealing time does not necessarily guarantee better Q^T_{001}. In a case in which a magnetic CoFeB seed is detrimental to the targeted application one has to stay below the critical thickness for the CoFeB seed, which is 4.2 Å. Since the rotation of the substrate was turned off in order to obtain thickness gradients, deposition conditions were slightly different than for samples of the results from fig.23, i.e. here Q^T_{001} tends to be even more enhanced.

(**001**) **low-RA:** Cr is known to grow mainly (011) or (001) on amorphous substrates, sensitively depending upon the deposition parameters: growing Cr directly onto *am.*-Ta leads to a mixed texture with dominating (011), but also can lead to a pure (001)-texture at elevated temperatures as previously discussed, compare figs. 26 and 27. The key here is the deposition temperature T_s of Cr, where it is reported that $T_s > 250°C$ can generate (001)-texture[78]. Q^T_{001} is found to be highest for $T_s \approx 185°C$. It is important to notice that Cr enters Zone *T* of the SZM at this temperature, meaning that intergranular diffusion is active which supports textured and columnar growth. Further improved (001)-texture on SiO_2 can be generated by utilizing a simple Ti seed, see fig. 26.

[78] Y. C. Feng, D. E. Laughlin, and D. N. Lambeth, *J. Appl. Physics* **76**, 11 (1994), pp. 7311–7316, D. E. Laughlin et al., MRS Proc. **343** (1994), pp. 327–336

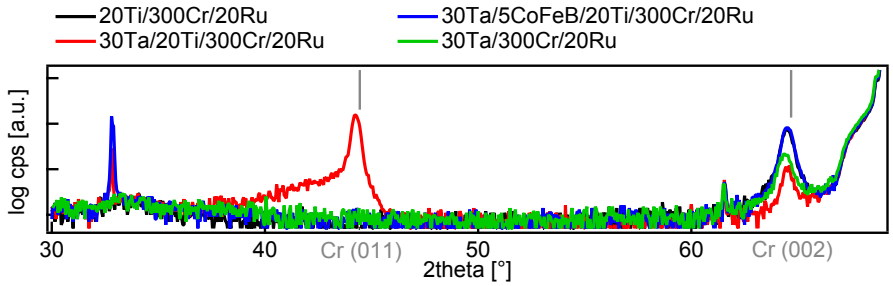

Figure 26: $2\theta/\omega$ XRD scan: different low-*RA* seed+buffer combinations on Si/SiO_2 with Cr deposited at 185°C. For Ta this leads to degraded (001)-texture (green). With Ti inserted between Ta and Cr a mixed (011)/(001)-texture evolves (red). A thin CoFeB insertion (blue) finally generates the same texture as on Si/SiO_2 (black).

(**011**) **bufferless low-RA:** There are several reported materials that generate a strong (011)-texture for Heusler materials, for example the previously mentioned V. Also, 30 Å *am.*-Ta lead to a strong (011)-texture. An additional layer of 20 Å Ru onto a Ta seed increases Q^T_{011} of Cr by 450% towards 18. Subsequent deposition of 20 Å Ti analogously to the (001)-textured version shows no further effect, see fig. 27.

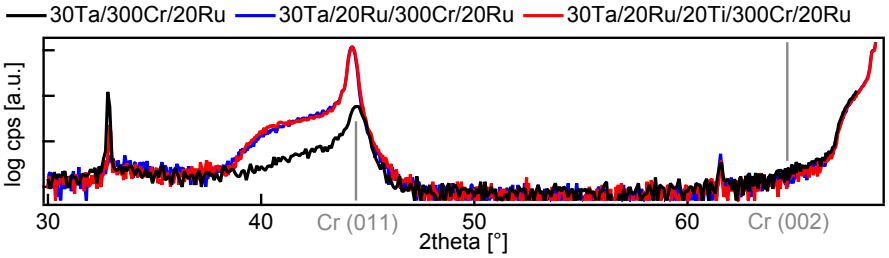

Figure 27: $2\theta/\omega$ XRD scan: low-RA (011)-textured seed with Cr deposited at 185°C, except for 30Ta/300Cr/20Ru where it is grown at RT: the Ta/Ru combination provides the strongest (011)-texture for Cr buffers. There is no change when using Ti.

Transition from Si/SiO$_2$ to AlTiC wafers

For the AlTiC wafer an ultrathin *am.*-Ta separation layer ($t \approx 10$Å) is sufficient to eliminate the influence of the NiFe shield on the thin film growth. The starting point from this AlTiC/NiFe/*am.*-Ta is however different from the Si/SiO$_2$ situation. Differing surface tension and wettability of insulators such as SiO$_2$ or MgO when compared to metals such as Ta affect the nucleation and growth mode. To match the conditions on the AlTiC wafer for a later transfer of the deposition process Si/SiO$_2$ $\rightarrow$ AlTiC, 30 Å amorphous Ta are deposited onto Si/SiO$_2$, which however ultimately change the texture of the complete stack as compared to w/o Ta. The resulting Q^{T}_{001} is therefore not optimized for the AlTiC substrate and it is necessary to restore the previously generated Si/SiO$_2$-wafer-based textures on Si/SiO$_2$/*am.*-Ta:
(**001**) **high-RA on AlTiC:** We will find for the low-RA that a CoFeB insertion after *am.*-Ta is sufficient to restore the texture. Since CoFeB is sputtered before MgO in the high-RA case, a *am.*-Ta/CoFeB/MgO combination provides highest (001)-texture on AlTiC.
(**001**) **low-RA on AlTiC:** inserting Ta below 20 Å Ti - the best (001) seed obtained on Si/SiO$_2$ - leads to degraded (011)-texture. To restore Q^{T}_{001} (as compared to deposited on Si/SiO$_2$), the combination *am.*-Ta/CoFeB/Ti is introduced. An insertion of amorphous 5Å CoFeB is sufficient to match the texture of the same films on Si/SiO$_2$ and leads to the highest Q^{T}_{001}. This approach even slightly increases Q^{T}_{001} on Si/SiO$_2$ (fig. 26) and gives a smoother film surface (AFM in fig. 28). Imaging via *high resolution transmission electron microscopy* (HRTEM) in fig. 75 (later chapter) shows such a Ta/CoFeB/Ti/Cr combination with a Heusler film on top on Si/SiO$_2$.
(**011**) **low-RA on AlTiC:** since the starting point for this texture on Si/SiO$_2$ wafers is *am.*-Ta, a change to AlTiC substrate will not affect it.

Tab. 1 summarizes all the different seed combinations and their resulting texture. Note, that high-RA seeds use only 150 Å Cr buffer, whereas the low-RA types use 300 Å Cr in this investigation. AFM images of selected seed+buffer systems are shown in fig. 28, where it is noticeable that different seed layers have a varying impact on the Cr morphology and grain size.

Table 1: seed/buffer layer combinations deposited on Si/SiO_2 substrates. The line separates seed types w/o (top) and with (bottom) MgO (low-RA and high-RA, respectively). The numbers in squared brackets denote thickness values or ranges. Q^T_{hkl} for Cr is evaluated following eq. 47 and (hkl)* denotes the dominating orientation in case of a mixed (001)/(011)-texture. All Cr layers are deposited at 185°C, except in the case for the 20 Å Ta seed that leads to (011)-texture, where it is deposited at RT. **Bold numbers** denote best values.

seed system [Å]	Cr [Å]	texture	Q^T_{hkl}	AFM
-	[150]	(011)	0	-
Ti [20]	[300]	(001)	12	(a)
Ta [20]	[300]	(001)	4	-
Ta [20]	[300]	(011)	2	-
Ta/Ti [20/20]	[300]	(011)*	2	-
Ta/Ru [20/20]	[300]	(011)	**18**	(b)
Ta/Ru/Ti [20/20/20]	[300]	(011)	18	(c)
Ta/CoFeB/Ru [20/20/20]	[300]	(011)	11	-
Ta/CoFeB/Ti [30/5/20]	[300]	(001)	**13**	(d)
MgO [10]	[150]	(001)	8	(e)
Ta/MgO [20/10]	[150]	(001)	3	-
Ti/MgO [20/10]	[150]	(001)	6	-
Ti/CoFeB/MgO [20/2-13/6-10]	[150]	(001)	2-**24**	(f)

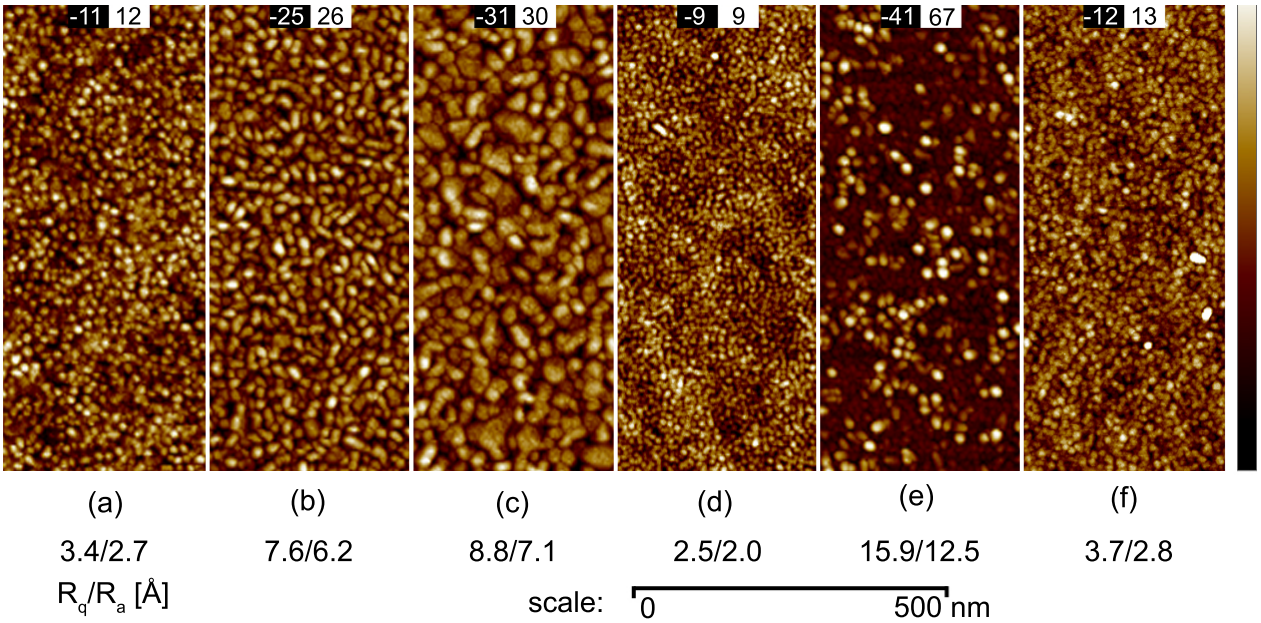

Figure 28: AFM images of the seed types as denoted in tab. 1. The numbers at the top denote the depth profile minimum and maximum (their difference is therefore R_z). The roughness values R_q/R_a are at the bottom. The thicknesses for (f) are 20Ti/5CoFeB/10MgO.

Engineering ultrasmooth thin films

Apart from tuning texture, minimized nanoscale roughness for seed/buffer layer combinations is important. This requirement extends further into the stack, especially atomic smoothness of the *ferromagnet/non-magnet* (FM/NM) interface is a crucial condition for GMR and TMR device performance. The following agenda needs to be addressed in order to obtain a feasible spacer for CPP-GMR devices:

- reduction of grain size and roughness
- decrease of interlayer exchange coupling
- maintaining a long spin-diffusion length $l_{sf} > 10$ nm

A prominent material used as spacer layer for CPP-GMR is Ag (see later chapter on page 93). Ag thin films tend to exhibit rough surfaces due to poor wettability (especially on glass) and agglomeration[79] that can be described by vacancy and adatom distribution models. When used as a spacer layer this can give rise to increased interlayer or pinhole coupling, which is detrimental to an independent switching of the FM layers. The problem of sputtering atomically smooth Ag ultrathin films complicates its utilization for novel applications (owing to its advantageous electric and optical properties) for decades. The activation energy of grain growth for Ag is comparable to the surface diffusion energy[80]. Thus grain evolution for Ag is dominated by surface diffusion mass transport and leads to a Volmer-Weber[81] growth mode with agglomeration which worsens during thermal processing. Furthermore, the Ehrlich-Schwöbel barrier for vacancies on step edges is very high, which produces a downhill vacancy current or a corresponding uphill mass current and promotes pitting and mounding. The *step-attachment barrier* E_{att} is the energy difference of a diffusing surface adatom (or vacancy) on an upper terrace to an adatom (or vacancy) that is attached to a downward edge of that same terrace (prior to descending). For both (001) and (111) Ag surfaces there is a large discrepancy for E_{att} of vacancies and adatoms, meaning that there is a preferred downflow of vacancies and upflow (clustering) of adatoms. This clustering effect is more dramatic for (001)- than for (111)-textured Ag films, because in addition to E_{att} the ascent of adatoms from a lower terrace up is energetically favored by a factor of 3 for (001) as compared to (111)[82].

[79] M. Kawamura et al., *Vacuum* **87** (2013), pp. 222–226

[80] R. Dannenberg et al., *Thin Solid Films* **379**, 1-2 (2000), pp. 133–138

[81] J. A. Venables, G. D. T. Spiller, and M. Hanbucken, *Reports on Progress in Physics* **47**, 4 (1984), p. 399

[82] M. I. Haftel, *Phys. Rev. B* **64** (12 2001), p. 125415

Ag roughness on high Q^{T}_{001} low-RA seed/buffer

50 Å thick Ag films are deposited onto the low-RA seed + Cr buffer combination which gave the highest Q^{T}_{001}, see tab. 1, on both Si/SiO_2 and AlTiC, to investigate their morphology. Ultimately, the aim is to stride towards CPP-GMR implementation by offering low RA and using the most suitable buffer materials for Heuslers. Specifically terminating the buffer with Ag is important to prevent detrimental Cr diffusion into

[83] Y. Sakuraba et al., *Phys. Rev. B* **82** (9 2010), p. 094444

the Heusler[83].
Before the deposition of Ag, the AlTiC wafer temperature can be reduced below RT via an in-situ cryogenic cooling module. Temperature is the primary parameter in the SZM and different temperatures will render specific mobilities. This makes it possible to move to Zone *Ic* by reducing the thermal activation of Ag adatoms. It has to be taken into account that the wafer warms up during transfer and its temperature at the start of Ag deposition should be calculated via eq. 42. Cryo-deposition will not be conducted on Si/SiO_2 since the low thermal capacity of Si will lead to an accelerated warm-up during transfer as compared to AlTiC and may lead to incomparable and unreproducible results. Some of the samples are in-situ post-annealed just after the Ag deposition in order to trigger recrystallization. The final stacks are capped with 20 Å Ru. A sample ID is assigned and a summary is given in tab. 2. Sample S5 is the roughness reference on Si/SiO_2 without Ag.

Table 2: 50Å thick Ag thin film are deposited using the (001) low-RA seed 30Ta/10CoFeB/20Ti/150Cr. The Cr buffer is grown at 185°C. The stacks are identical, but they differ in substrate type, deposition temperature and in-situ annealing treatment. T_s, T_a are substrate temperature at start of Ag deposition and in-situ annealing temperature after Ag deposition, respectively. The corresponding AFM scans are shown in fig. 29.

sample ID	substrate	T_s [°C]	comment
S1	Si/SiO_2	RT	$T_a = 410$
S2	Si/SiO_2	RT	$T_a = 325$
S3	Si/SiO_2	RT	$T_a = 150$
S4	Si/SiO_2	RT	no anneal after Ag
S5	Si/SiO_2	RT	no Ag, reference
A1	AlTiC	RT	no Ag, reference
A2	AlTiC	−45	no anneal after Ag
A3	AlTiC	−125	no anneal after Ag

Fig. 29 shows the corresponding AFM images. Post-annealing between 150−410°C (sample S1-S3), leads to considerable agglomeration of Ag. The resulting clusters have increased height with higher temperature and recrystallization is inevitably linked to 3D growth, which thereby partially exposes Cr. This can be seen by comparing similar roughness contrasts of particular regions of S2, S3 and S5 in fig. 29. Deposition of Ag at RT (sample S4) leads to a smaller lateral cluster size of ≈30 nm and a height of ≈ 10 nm. Sample A1 is the roughness reference (no Ag) on AlTiC. It is about three times as rough as the analogous sample S5 on Si/SiO_2. However, cryo-deposition on AlTiC at $T_s = -125$°C helps to achieve a minimal roughness for Ag. The capabilities of the ANELVA sputter system allow for deposition as low as $T_s = -140$°C, which potentially will lead to even smoother Ag films.

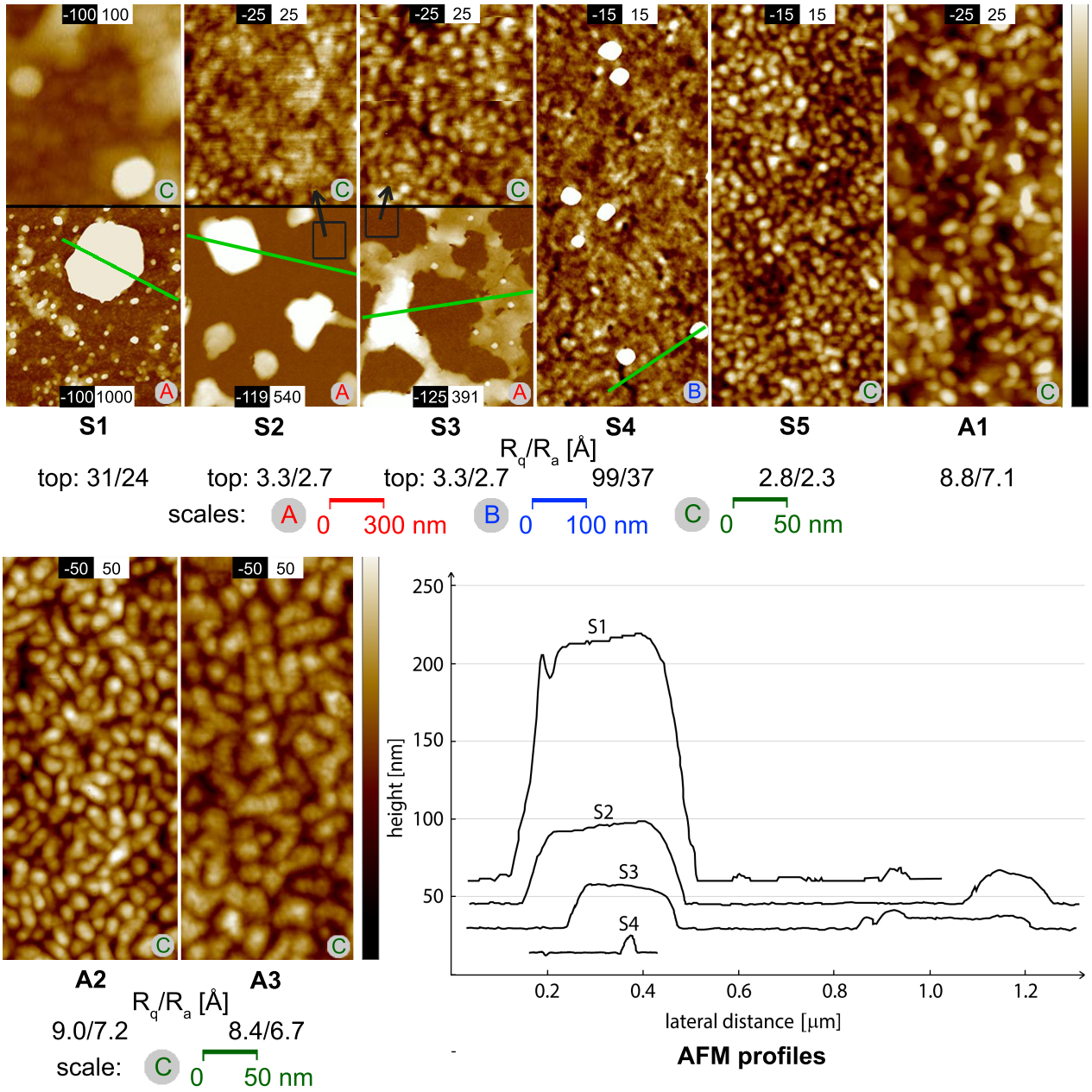

Figure 29: samples as depicted in tab. 2. The numbers within the images denote the AFM measurement ranges, which are also expressed in the contrast of the images. Below the images are the values R_q and R_a. The colored letters represent the corresponding scale used for a particular image. The green lines denote cross sections that are collectively graphed in the lower right graph. Exceptionally tall islands that comprise most of the deposited Ag form as a result of agglomeration exhibit larger dimensions with increasing annealing temperature. Cryo-deposition of Ag on AlTiC substrate shows little improvement in roughness parameters R_q and R_a, but overall leads to larger islands and decreased clustering.

Ag roughness on high Q^{T}_{001} high-RA seed/buffer

Apart from a comparably thin insertion of 50 Å Ag between Cr and the Heusler for the low-RA system, thicker Ag film of ≈ 300 Å are needed for the high-RA system in order to provide a reasonable bottom electrode resistance for e.g. a CPP-GMR device (see chapter on p. 93). Therefore the morphology of thicker Ag thin films is investigated for the high-RA seed combination 20Ti/5CoFeB/20MgO on Si/SiO_2 which resulted in the highest (001) orientation and lowest roughness, see tab. 1 and fig. 28 (f). Ag films are grown at RT, unless specified otherwise. All samples are listed for comparison in tab. 3. The texture drastically degrades whenever the Cr buffer is not included. Ti as underlayer and cap has been reported to dramatically reduce Ag agglomeration, even under elevated temperatures[84]. Other underlayer types that increase wettability by decreasing interface energy and therefore reducing roughness are TaN[85]. Utilizing a 20 Å Ti seed generates the desired (001)-texture and reduces roughness notably, but the thin film has inferior crystallinity. The best (001)-texture is still obtained with an underlying Cr buffer. However, the surface exhibits significant roughness due to Ag 3D growth, as it has been explained and demonstrated in the previous section. Cryo-deposition helped to reduce the roughness for 50 Å thick Ag films, but there have also been successful reports on increasing Ag film smoothness by adding impurities (<10 at%) to Ag, i.e. Sn[86], Mg[87] or Ti[88]. While this increases the resistivity, some elemental impurities retain a long *spin diffusion length* l_{sf} of the alloy, such as Sn, Mn and Pt[89], which makes these combinations a feasible candidate for CPP-GMR spacer materials. The addition of light elements is preferred since l_{sf} is reduced mainly by increased spin-orbit coupling[90].
Another approach towards engineering smooth Ag thin films is by alloying a combination of Ag with Cu[91] or Al[92] or to use an interlayer insertion strategy as this proves to increase surface smoothness while maintaining a long l_{sf}. For $Cu_{80}Ag_{15}Au_5$[93] the increased mobility of Ag (0.14 eV) and Au (0.11 eV) adatoms on (111) Cu surface, compared to Cu (0.25 eV), effectively reduces the Ehrlich-Schwöbel barrier. Furthermore, Ag on the edge of a Cu terrace supports the descend of Cu by reducing E_{ES} from 0.35 eV to 0.28 eV. This is about the same value as for regular hopping on close packed Cu. Furthermore, Ag shows reduced alloying with Cu, leading to an Ag-rich surface which then continues to lower E_{ES} for Cu on ledge edges. This drastically reduces 3D growth, supports interdiffusion and prevents pinhole generation, which in turn leads to a smoother film. The higher surface energy of Cu can be utilized to initiate a smoother growth of Ag films which is especially interesting for ultrathin films with thicknesses in the range of island coalescence. One report describes the successful reduction of the critical thickness for a continuous Ag thin film with improved uniformity by a 10 Å Cu underlayer[94].
A set of samples is deposited to investigate possible benefits of a Cu in-

[84] M. Kawamura et al., *Vacuum* **87** (2013), pp. 222–226

[85] S. R. Akepati, H.l Cho, and K. Lee, *Electronic Mat. Lett.* **9**, 2 (2013), pp. 231–235

[86] J. C. Read et al., *J. Appl. Physics* **118**, 4, 043907 (2015)

[87] H. Narisawa, T. Kubota, and K. Takanashi, *Appl. Phys. Express* **8**, 11 (2015), p. 119201

[88] M. Kawamura et al., *Vacuum* **87** (2013), pp. 222–226

[89] Q. Yang et al., *Phys. Rev. Lett.* **72** (20 1994), pp. 3274–3277

[90] J. Bass and W. P. Pratt, *J. Phys.: Condens. Matter* **19**, 18 (2007), p. 183201

[91] Z. Yeongseok, H. Han, and T. L. Alford, *J. Appl. Physics* **102**, 8, 083548 (2007)

[92] H. C. Kim, N. D. Theodore, and T. L. Alford, *J. Appl. Physics* **95**, 9 (2004), pp. 5180–5188, H. C. Kim et al., *Mat. Research Soc. Symp. Proc.* Ed. by R.J. Carter et al., vol. 812, link, 2004, pp. 209–214, K. Sugawara et al., *Vacuum* **83**, 3 (2008), pp. 610–613

[93] W. Zou et al., *Mat. Res. Soc. Symp. Proc.* **674** (2001), T1.5.1

[94] N. Formica et al., *ACS Appl. Mat. & Interfaces* **5**, 8 (2013), pp. 3048–3053

terlayer insertion. Since the Cr buffer is needed to obtain (001)-texture, but the Ag island formation is dramatic on Cr, a 150Cr/10Cu/300Ag combination is grown on the high-RA 20Ti/5CoFeB/20MgO trilayer. The results are compared to 150Cr/300Ag combinations without Cu. Mapping of the sheet resistance $R_{\square}$ as shown in fig. 30 reveals a drastically improved uniformity of the film with Cu insertion. Fig. 31 (a) shows XRD scans of three (001)-textured stacks without Cu insertion layer. Two of them are in-situ post-annealed at high temperature (500°C for 600 seconds) in order to fully crystallize the stack and to trigger Ag agglomeration. Of these annealed samples, one has been capped after the anneal and the other before. There is no significant difference in crystallinity. 10 Å Cu insertion improves the (001)-texture as the (111) Ag peaks almost vanishes, see fig. 31 (b). The Cu insertion is also tested for (111)-textured Ag films on the low-RA 30Ta/20Ru seed system and XRD scans in fig. 32 show a Q^{T}_{111} improvement. Generally, the Ru cap *traps* Ag and prevents surface diffusion and thus agglomeration during annealing, see AFM height profiles of the (001)-textured films in

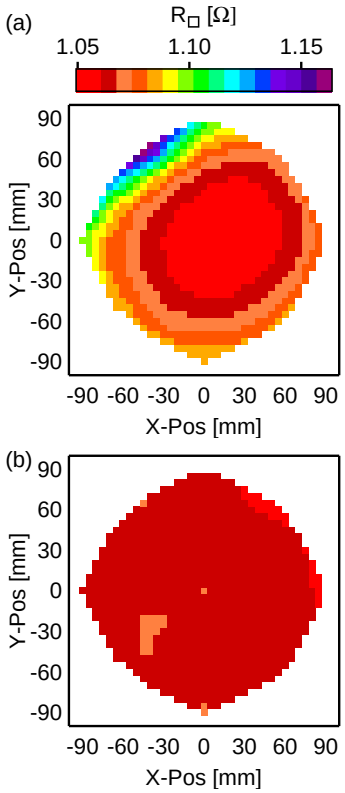

Figure 30: $R_{\square}$ maps of (a): 150Cr/300Ag/20Ru/RTA and (b): 150Cr/10Cu/300Ag/20Ru/RTA. The Cu interlayer improves film uniformity.

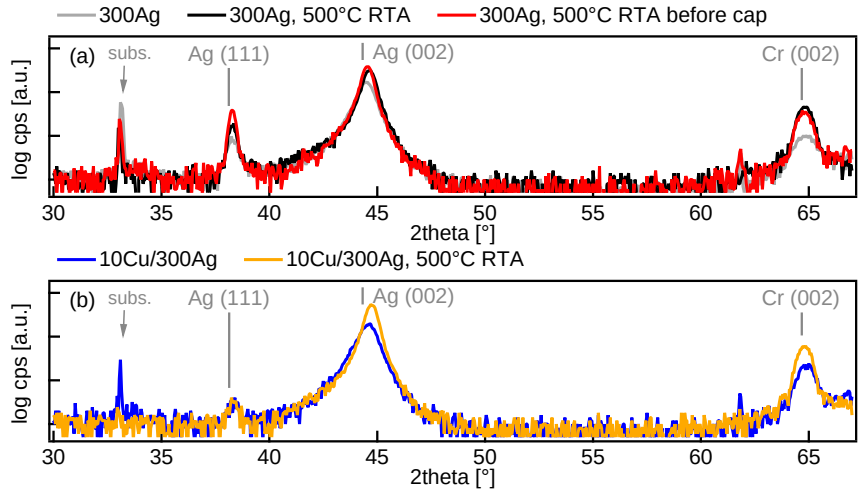

Figure 31: samples on Si/SiO_2 with high-RA seed and (001) Cr buffer (20Ti/5CoFeB/20MgO/150Cr); (a): 300Ag added: no annealing (gray), in-situ RTA after (black) and before (red) capping with Ru. There is no significant difference in crystallinity; (b): 10 Å Cu interlayer improves Q^T_{001}.

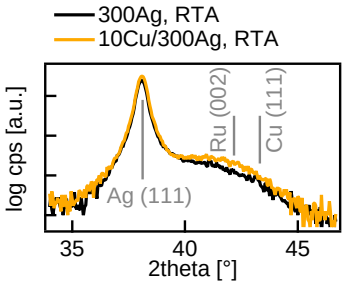

Figure 32: $2\theta/\omega$ XRD scan: samples on Si/SiO_2 with low-RA (111) seed (30Ta/20Ru). Both samples have been annealed at 500°C. There is an improvement of Q^T_{111} with Cu insertion.

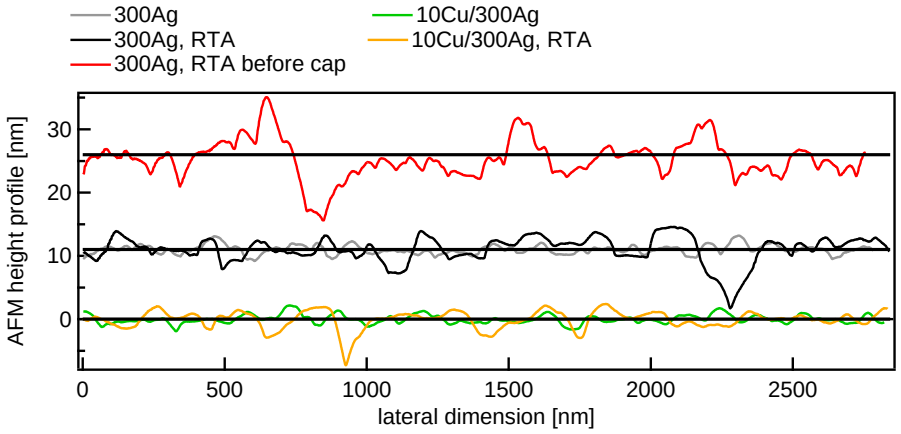

Figure 33: height profiles from the same specimen as in fig. 31 (same coloring). The curves are offset for a better visibility.

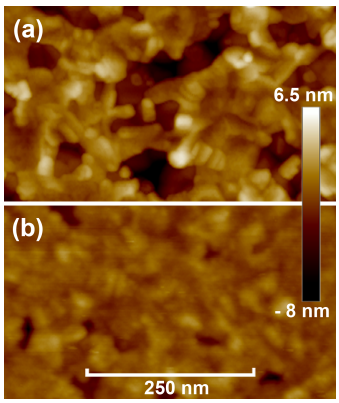

Figure 34: AFM images of (a): the corresponding black and (b): yellow profiles in fig. 33.

Table 3: Properties for Ag thin films on (001)-textured high-RA Si/SiO_2/20Ti/5CoFeB/20MgO and on (111)-textured low-RA 30Ta/20Ru, separated by a double line. R_z is the maximum height of the roughness profile. Texture and Q^T_{hkl} values address the Ag layer. Cr is grown at 180°C. RTA is at 500°C for 600 seconds. The bold numbers denote the significantly better values of each pair of samples. σ is the standard deviation of $R_\square$

layers [Å]	R_z [Å]	R_a/R_q [Å]	texture	Q^T_{001}/Q^T_{111}	$R_\square/\sigma$ [Ω]/[%]
…/300Ag/20Ru +300°C	436	31/41	(001)/(111)	0.6/1	n.a.
…/20Ti/300Ag/20Ru +300°C	100	10/35	(001)/(111)	6/0.5	n.a.
…/150Cr/300Ag/20Ru	62	6/7	(001)/(111)	**22.2**/0.6	1.24/0.24
…/150Cr/10Cu/300Ag/20Ru	**54**	**5**/**7**	(001)/(111)	16.9/**0.0**	1.19/0.32
…/150Cr/300Ag/20Ru/RTA	201	13/18	(001)/(111)	18.7/0.3	1.07/2.08
…/150Cr/10Cu/300Ag/20Ru/RTA	**143**	**7**/**10**	(001)/(111)	**29.6**/**0.1**	1.06/**0.23**
…/150Cr/300Ag/RTA/20Ru	464	28/44	(001)/(111)	20.4/0.5	0.96/1.83
30Ta/20Ra/300Ag/20Ru/RTA	194	11/17	(111)	45	1.013/0.67
30Ta/20Ra/10Cu/300Ag/20Ru/RTA	**69**	**8**/**10**	(111)	**56**	1.00/0.63

fig. 33. A further advantage of Cu insertion becomes apparent when comparing the film roughnesses. The Cu insertion also preserves the initial film roughness after the high temperature anneal, see figs. 33 and 34, as it reduces both the roughness and the maximum height R_z of the profile. Also, Q^T_{001} of Cr increased from 17 to 22, possibly due to Cu diffusion into grain boundaries and support of crystallization. For the (111)-texture AFM imaging shows that Ag agglomeration is considerably suppressed with Cu insertion after 500°C RTA, see fig. 35. The uniformity of the films is unchanged however, see $R_\square$ and σ in tab. 3. The table summarizes all results obtained with XRD, AFM and 4-probe sheet resistance measurements and highlights the best results. (001) Cu/Ag has a higher R_z than (111) Cu/Ag due to some residual deep pinhole-like valleys, see AFM in fig. 34. Overall, Cu insertion leads to more desirable results for both Ag texture types but shows a more dramatic improvement for the (001)-texture as compared to the (111)-type. The large Ag thickness and high 500°C annealing temperature are not optimal and are only chosen to exaggerate the effect of Cu insertion on the Ag morphology. The roughness shown here is not yet usable for a CPP-GMR device. However, the results are expected to scale for thinner ≈50 Å Ag films and cryo-deposition + Cu insertion will be implemented for CPP-GMR devices. Furthermore, the optimum annealing temperature for the Heuslers used will prove to be only $T_a \approx 370$°C, which will be in favor of reduced agglomeration.

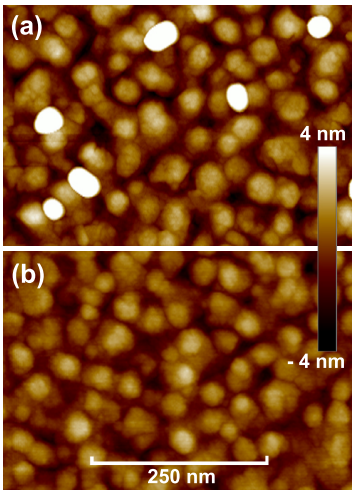

Figure 35: AFM images of the same samples as in fig. 32; (a): no Cu interlayer; (b): Cu insertion successfully suppresses agglomeration on (111) Ag.

PMA thickness dependence of $Mn_{3-x}Ga$

The purpose of this chapter is to investigate the applicability of Mn-Ga Heusler thin films exhibiting high PMA for spintronic devices. The key for industrial integration into a *perpendicular magnetic tunnel junction* (pMTJ) is a film thickness $t < 100$ Å. Therefore, a key question is the effect of lattice strain on PMA. The PMA thin films here are grown epitaxially on (001)-MgO substrate, but a transfer to the developed seed layers for polycrystalline (001)-texture is the next step towards industrial application.

PMA

The PMA of a monocrystalline thin film is the sum of an interface $K^{\perp,\mathrm{A}}$ and an intrinsic contribution $K^{\perp,\mathrm{bulk}}$, see eq. 32. The latter arises from the unit cell configuration and is therefore a uniaxial magnetocrystalline anisotropy $K_1^{\perp}$. This sum also is commonly referred to as K_U. When grown as thin films with the uniaxial anisotropy perpendicular to the substrate, high PMA materials show an out-of-plane orientation of M_s because they typically exhibit $K_1^{\perp} \sim 10$ Merg/cc while $K^{\perp,\mathrm{A}}$ is negligible. This can lead to an exceptionally large thermal stability factor $K_\mathrm{U}V/k_\mathrm{B}T \geq 40-100$ that ensures non-volatility of the stored information. This is in contrast to interface-dominated PMA reported for e.g. CoFe[95], CoFeB[96], Co_2FeAl[97], $Co_2Fe_xMn_{1-x}Si$[98] where the PMA is too weak to stabilize nanoscale devices. Combined with a high spin polarization P$\sim$ 100%, high-PMA materials are promising candidates for STT-MRAM[99], which utilizes pMTJs as core structure. Further requirements are high $T_\mathrm{C} > 700°$C for thermal stability and low damping constant $\alpha < 0.01$ with small $M_\mathrm{s} \sim 100$ emu/cc for fast and high-SNR switching at low switching current.

High-PMA Heuslers

Tetragonal Heuslers[100] and Heusler-like compounds such as Mn-Ga[101], Mn-Ge[102] are in the focus of research for such high-PMA applications, as they fulfill all of the above requirements. Many Mn-rich Heusler compounds feature a tetragonal distortion which is the origin of this anisotropy. A van-Hove-singularity around E_F results in high peaks of the *density of states* (DOS) which ultimately causes a structural instability of the cubic phase of the material. In the cubic phase, Mn_3Ga is

[95] J. Zhang et al., *Phys. Rev. B* **90** (18 Nov. 2014), p. 184409

[96] S. Ikeda et al., *Nat. Mat.* **9** (2010), pp. 721–724, L. Reichel et al., *J. Phys.: Condens. Matter* **27**, 47 (2015), p. 476002, J. Sinha et al., *J. Appl. Physics* **117**, 4, 043913 (2015)

[97] Y. Cui et al., *Appl. Phys. Lett.* **102**, 16, 162403 (2013)

[98] T. Kamada et al., *IEEE Transactions on Magnetics* **50**, 11 (2014), pp. 1–4

[99] J.C. Slonczewski, *J. Magn. Magn. Materials* **159**, 1-2 (1996), pp. L1–L7

[100] L. Wollmann et al., *Phys. Rev. B* **92** (6 2015), p. 064417

[101] H. Kurt et al., *Phys. Rev. B* **83** (2 Jan. 2011), p. 020405

[102] H. Kurt et al., *Appl. Phys. Lett.* **101**, 13, 132410 (2012), Y. Miura and M. Shirai, *IEEE Transactions on Magnetics* **50**, 1 (Jan. 2014), pp. 1–4, S. Mizukami et al., *Appl. Phys. Express* **6**, 12 (2013), p. 123002

predicted to be a fully compensated half-metallic ferrimagnet. However, the compound is only stable in the tetragonal phase with a calculated spin polarization of 88%[103] and hard out-of-plane magnetic properties[104] with $T_C = 730°C$. The composition of $Mn_{3-x}Ga$ ranges from the instable cubic $D0_3$ phase ($x = 0$), which is the binary equivalent of the cubic Heusler $L2_1$, to the tetragonal $D0_{22}$ phase ($0 < x < 1.14$) and lastly to the Mn poor $L1_0$ phase of Mn-Ga. Through reduction of Mn below Mn_2Ga a stable tetragonal $L1_0$ phase is attained, which is practically a $D0_{22}$ with reduced symmetry due to the (partial) occupation of Ga atoms at the Wyckoff 2b positions[105], thus halving the lattice constant c. All phases are shown in fig. 36. The blue (MnI, $m = -2.9\mu_B$) and red (MnII, $m = 2.36\mu_B$) positions of the Mn atoms are inequivalent and with the reduction of Mn from Mn_3Ga, mainly but not exclusively MnI is replaced by Ga[106]. However, the bulk vacancy distribution model is not entirely consistent with the thin film model[107] and the detailed mechanism is still unclear. *Mizukami et al* found that the 4d Wyckoff position (MnII) for thin films is occupied with Mn with a 93% chance when increasing x in order to fit their magnetization data. For bulk $Mn_{3+x}Ge$, the stability of the $D0_{22}$ is within a narrow range of $0.26 < x < 0.55$[108]. The properties of Mn-Ga and Mn-Ge from the cited references are summarized in tab. 4.

Here the focus will be on Mn-Ga. Many groups have been investi-

Table 4: Properties of $D0_{22}$ Mn-Ga and Mn-Ge. See text for references.

		$Mn_{3-x}Ga$	$Mn_{3+x}Ge$
x		0–1.14	0.26–0.55
M_s	[emu/cc]	200–600	73–130
T_C	[°C]	730	> 500
α		0.008–0.015	0.0009
K_U	[Merg/cc]	10–24	9–24
P	[%]	40–88	77–100

gating varying composition ranges in bulk and thin films[109] ranging from $Mn_{1.63}Ga$[110] to $Mn_{3-x}Ga$ ($0 \leq x \leq 1$)[111]. The reports about Mn-Ga however are mostly limited to a film thickness of $200-1000$ Å and while discussing the role of underlayers[112] don't examine the effects of reducing the layer thickness. Additionally to the requirements mentioned above, the thickness of the MTJ ultimately needs to be reduced as much as possible for industrial applications. This is crucial for the implementation of this Heusler into devices with high information density. The thickness dependence of the PMA for films with $t < 100$ Å will be investigated in this chapter.

$Mn_{3-x}Ga$ thin films

To obtain a sufficient signal for magnetization measurements with a *superconducting quantum interference device*-VSM (SQUID-VSM), a com-

[103] B. Balke et al., *Appl. Phys. Lett.* **90**, 15, 152504 (2007), J. Winterlik et al., *Phys. Rev. B* **77** (5 2008), p. 054406, S. Wurmehl et al., *J. Phys.: Condens. Matter* **18**, 27 (2006), p. 6171

[104] E. Krén and G. Kádár, *Solid State Commun.* **8**, 20 (Nov. 1970), pp. 1653–1655

[105] T. Graf, C. Felser, and S. S. P. Parkin, *Progress in Solid State Chemistry* **39**, 1 (2011), pp. 1–50

[106] J. Winterlik et al., *Phys. Rev. B* **77** (5 2008), p. 054406

[107] S. Mizukami et al., *Phys. Rev. B* **85** (1 Jan. 2012), p. 014416

[108] A. B. Gokhale and R. Abbaschian, *Bulletin of Alloy Phase Diagrams* **11**, 5 (1990), pp. 460–468

[109] S. Mizukami et al., *Phys. Rev. B* **85** (1 Jan. 2012), p. 014416

[110] K. M. Krishnan, *Appl. Phys. Lett.* **61**, 19 (Jan. 1992), p. 2365

[111] M. Glas et al., *J. Magn. Magn. Materials* **333** (Feb. 2013), pp. 134–137, H. Kurt et al., *physica status solidi (b)* **248**, 10 (2011), pp. 2338–2344, F. Wu et al., *Appl. Phys. Lett.* **94**, 12, 122503 (2009), F. Wu et al., *J. Phys. Conference Series* **266**, 1 (2011), p. 012112

[112] M. Li et al., *Appl. Phys. Lett.* **103**, 3 (2013)

position close to Mn_2Ga is targeted here, where the magnetic moment of MnII is not compensated due to a lack of MnI. This leads to a comparably high M_s. Offstoichiometric Mn_2Ga films with and without Co doping are prepared by sputtering with an Ar pressure of 10^{-3} mbar. The base pressure is less than 10^{-10} mbar. The films are grown on two different buffer types: Cr and a Cr/Pt combination. The deposition steps on single crystalline (001)-MgO substrates for the respective buffer layers are:

Cr: 400Cr/$Mn_{1.9}Co_{0.1}$Ga/2h@400°C/30Ta

400Cr/$Mn_{1.86}$Ga/2h@400°C/30Ta

Cr/Pt: 100Cr/1h@700°C/100Pt@500°C/$Mn_{1.9}Co_{0.1}$Ga@450°C/30Ta

A step is conducted at RT when not indicated otherwise. The Ta layer serves as protective capping. The composition of the films is analyzed by a system that combines RBS with *particle-induced X-ray emission* (RBS/PIXE) with a precision of 1 at%. The lattice constant of MgO ($a = 4.21$ Å) leads to an epitaxial 45° in-plane rotated growth of Cr ($a = 2.88$ Å). The Pt buffer ($a = 3.92$ Å) then grows again 45° rotated on Cr.

When $Mn_{1.9}Co_{0.1}$Ga samples are deposited on the Cr/Pt buffer at RT they are nonmagnetic even after post-annealing at 400°C or 450°C. Therefore those samples are deposited at 450°C instead, which has been found to be the optimal substrate temperature[113].

[113] M. Li et al., *Appl. Phys. Lett.* **103**, 3 (2013)

In accordance with the chosen $D0_{22}$ unit cell in fig. 36 the XRD (011) reflex is scanned to estimate the structure of the films. An absence of this reflex would suggest the $L1_0$ structure, because there the structure factor is zero. For the sake of consistency and to reduce confusion the planes are indexed referring to the unit cell shown in fig. 36, e.g. the $L1_0$-(001) reflex is the same as $D0_{22}$-(002).

For the estimation of the in-plane lattice constant a, an energy-dispersive

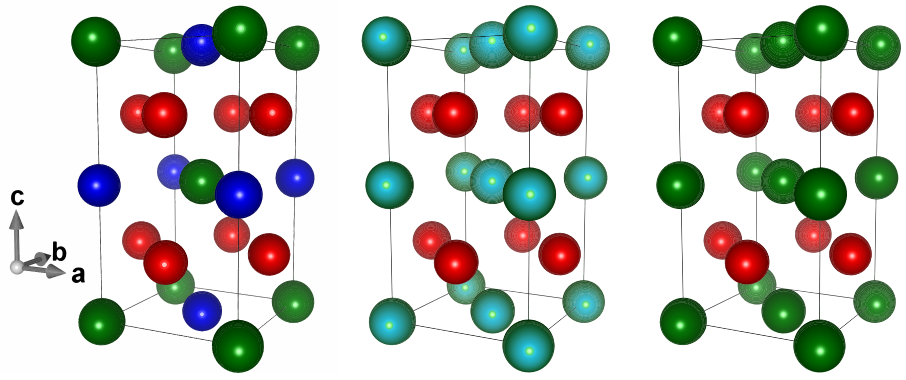

Figure 36: left: binary Mn_3Ga or Mn_3Ga with Ga/Ge (green), MnI (blue) and MnII (red) in the $D0_{22}$ structure. The axis of the unit cell are indicated by arrows. Center: with $0<x<2$ the cyan colored atoms are either Ga/Ge or Mn, depending on the specific composition and the symmetrie is still $D0_{22}$. Right: $L1_0$ structure of MnGa or MnGe with two stacked unit cells.

1D detector was utilized in order to create a 2D $2\theta/\omega-\chi$ scan map in

which the (112)-reflection appears as a 3D gaussian shape. The (112)-reflex was chosen, since its intensity is the strongest[114] thus making the investigation by XRD down to a thickness of 20 Å possible. For the films on Cr/Pt-buffer the (224)-reflex had to be chosen for the estimation of a due to peak overlap of the sample-(112) with the Pt-(111) reflex at $2\theta = 39.8°$. Due to its reduced intensity it is not possible to appropriately estimate both lattice constants of the 30 Å Cr/Pt-buffered $Mn_{1.9}Co_{0.1}Ga$ film.

[114] to prevent confusion it has to be mentioned that some databases identify the (022) reflex as the one with the highest intensity, since they refer to the Heusler-type $L2_1$ unit cell

Fig. 37 shows excerpts of the $2\theta/\omega$ scans of the films. In the full range

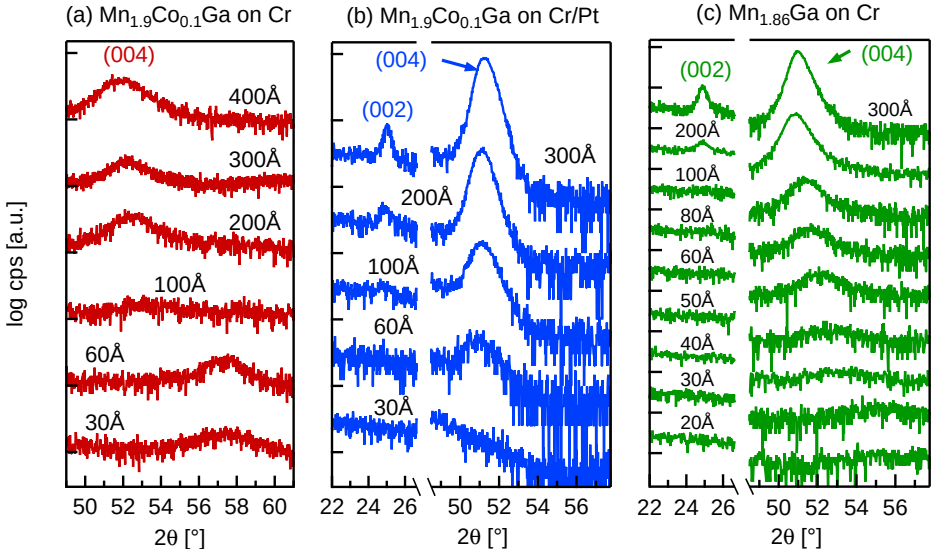

Figure 37: $2\theta/\omega$ scan excerpt of the (002)/(004) reflexes of (a): $Mn_{1.9}Co_{0.1}Ga$ on Cr buffer, no (002) was observed; (b): $Mn_{1.9}Co_{0.1}Ga$ on Cr/Pt buffer; (c): $Mn_{1.86}Ga$ on Cr. The numbers denote the film thickness in nm.

only the (001)/(002) substrate and (002) Cr reflexes are visible apart from the (002) and (004) reflexes of the Mn-Ga(-Co) film. For the Cr/Pt buffered samples also the (002) Pt reflex appeared. All films $t \leq 100$ Å show no (002) superlattice peak, because the signal is too weak. An important observation is the complete absence of the (002) superlattice peak for Cr buffered $Mn_{1.9}Co_{0.1}Ga$, whereas it appears for the same composition on the Cr/Pt buffer. This indicates a different ordering which is most likely due to the specific deposition temperature and not due to the choice of buffer layer. When changing the measurement geometry none of the films showed the (011) reflex. Therefore all films crystallized in the $L1_0$ structure. The lattice constant of the Cr buffer is $a_{Cr} = 2.885$ Å and for the Pt buffer $a_{Pt} = 3.946$ Å, both in agreement with bulk values from literature, $a_{Cr}^{lit} = 2.88$ Å, $a_{Pt}^{lit} = 3.92$ Å. Therefore, all films show epitaxial growth. A scan for the (111) Pt reflex proved its 45° rotated growth on the Cr buffer.

Fig. 38 (a)/(b) and (c) show the lattice constants and its ratios, respectively. It is noteworthy that the Cr/Pt-buffered thin films show a slight tetragonal elongation in c-direction when reducing the thickness. The lattice mismatch with Pt is $\Delta a = 0.5\%$ for all films.

The Cr-buffered Heusler films on the other hand are highly strained:

When reducing the thickness of $Mn_{1.9}Co_{0.1}Ga$ [$Mn_{1.86}Ga$] from 300 Å down to 30 Å, c decreases by 8.5% [8.0%] while a increases by 3.2% [4.6%] to values closer to the 45° rotated Cr lattice constant 2.88 Å$\cdot\sqrt{2}$ = 4.08 Å. The lattice mismatch of the 30 Å $Mn_{1.9}Co_{0.1}Ga$ [30 Å $Mn_{1.86}Ga$] with the Cr buffer is $\Delta a = 0.3\%$ [$\Delta a = 1.2\%$]. Noteworthy are the different regions of large strain gradient: the samples with Co attain highest strain towards a cubic-like structure at a larger thickness than the samples without Co. It has been found that $Mn_{1.92}Co_{0.42}Ga$ shows a phase transition from tetragonal to cubic when increasing Co content[115]. A possible dependence of strain on composition in the Mn-Co-Ga compounds should be investigated further.

Out-of-plane (OP) and *in-plane* (IP) magnetic measurements are conducted with a SQUID-VSM where $H_{max} = 70$ kOe. All OP scans saturate at higher fields around $H = 30$ kOe. It has been reported that thicker films (300 Å) of $Mn_{2.5}Ga$ are hard to saturate in the IP direction[116]. Indeed the IP curves don't saturate distinctively, which leads to a problem of a correct subtraction of the substrate background signal. With film thicknesses $t > 300$ Å it is convenient to measure a piece of reference substrate IP, weigh it and estimate the mass susceptibility, which can then be used to calculate the substrate contribution of the sample by weighing it and neglecting the weight of the film. However, when measuring ultrathin films $t < 100$ Å the contribution of the specimen to the overall measured signal can be negligibly small compared to the diamagnetic MgO substrate. The induced current in the pickup-coils of the SQUID-VSM is sensible to the precise substrate location, size and shape[117]. Therefore a different position of a sample creates a specific background signal in any repeated scan. To give an example, consider an IP scan and some linear reference curve used for correction: if the diamagnetic slope of this reference curve varies around 2% due to positioning, a simple linear reference background subtraction will lead to an error in M_s of ≈ 16 µemu (when using a 4.2x4.2 mm^2 MgO piece), which is about the same magnitude as the signal of a 30 Å thin film when using a similar sized sample piece. The less signal from that same specimen, the larger is the error induced by this method, which makes this approach impractical for this investigation.

The IP curves for the thickest films $t \geq 300$ Å with comparably large signal from the Mn-Ga(-Co) were obtained by subtracting a weighed MgO reference piece. When linearizing the IP curve they all saturated for $70\,\text{kOe} \leq H \leq 85\,\text{kOe}$, independently of the Co doping. To overcome the previously discussed problem effectively, all IP scans for the films $t \leq 200$ Å are expected to saturate when $H \geq 70$ kOe. This will tend to systematically underestimate the anisotropy field H_a for those films. This approach is encouraged by other reports, where for a 660 Å thick film of Mn_2Ga $H_a \approx 8$ kOe[118]. Wu et al. report $H_a \approx 6$ kOe for 300 Å $Mn_{65}Ga_{35}$ films on Cr or Cr/Pt buffer[119], which is the same compound as in our case, i.e. $Mn_{1.86}Ga$. $Mn_{1.9}Co_{0.1}Ga$ is somewhere between the

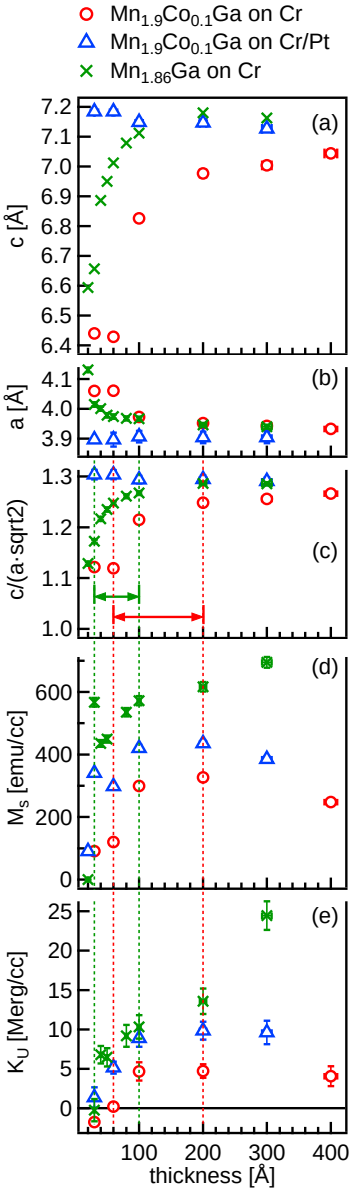

Figure 38: (a) and (b): lattice constants c and a versus thickness, respectively; (c): ratio $c/a\sqrt{2}$ versus film thickness. The regions of a large strain gradient are denoted by arrows that span extended lines throughout all the graphs. The Cr/Pt buffer films are unstrained within the whole range, whereas the Cr buffered compositions each show different strain vs. thickness behaviour; (d): M_s per volume; (e): uniaxial magnetic anisotropy K_U vs. thickness. It drops to zero within the indicated region of large strain. Error bars are included in all figures.

[115] T. Kubota et al., *J. Appl. Physics* **113**, 17, 17C723 (2013), S. Ouardi et al., *Appl. Phys. Lett.* **101**, 24 (Jan. 2012), p. 242406

two cited compositions when neglecting the Co-doping. This method will systematically include a thickness/strain dependence of K_U. Furthermore the geometry of the pick-up coils in the SQUID-VSM and the differing demagnetization fields for the OP and IP alignment will reduce the signal of any IP scan to around 80% of the same sample scanned OP[120]. Therefore the IP magnetic curves were scaled by a factor of 1.25. Selected hysteresis curves are shown in fig. 39 (a) for $Mn_{1.9}Co_{0.1}Ga$ on Cr and Cr/Pt buffer. Fig. 39 (b) shows M(H) curves for $Mn_{1.86}Ga$ on Cr. All 30 Å thick films show a dominating isotropic contribution

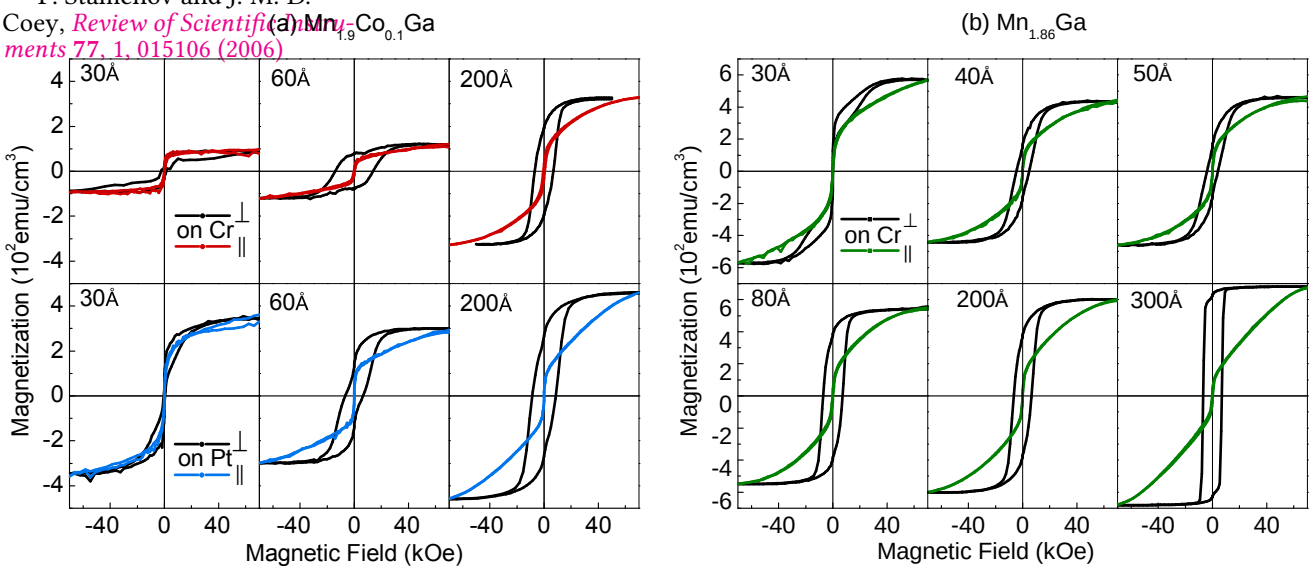

Figure 39: (a): hysteresis curves for $Mn_{1.9}Co_{0.1}Ga$ for various thicknesses deposited on Cr (top) and Cr/Pt (bottom) buffer layers. The superimposed magnetic moment can clearly visible for the Cr/Pt buffered films; (b): hysteresis curves for $Mn_{1.86}Ga$ for various thicknesses deposited on a Cr buffer layer.

when measured OP, indicating a loss of PMA. Some of the Cr buffered films feature a superimposed moment with almost zero hysteresis and small saturation field of ≈ 0.1 kOe in both IP and OP measurements. This isotropic moment systematically vanishes over time for the Cr buffered films, whereas it stays unchanged for the Cr/Pt buffered ones (not shown here). A canted magnetic moment was also previously reported for Mn_3Ga[121] and for $Mn_{2.1}Ga$[122]. The occurrence here is probably related to interface effects, oxidation or paramagnetic islands that form in the initial growth of the film.

M_s versus film thickness is shown in fig. 38 (d). For 300 Å $Mn_{1.86}Ga$ it is higher than previously reported[123].

Apparent is the effect of the Co content, as it drastically reduces the saturation magnetization. M_s for $Mn_{1.86}Ga$ is roughly doubled when compared to $Mn_{1.9}Co_{0.1}Ga$ (both on Cr buffer). It can be doubted that this effect is related to the 0.04 difference in Mn, a more realistic change related to this would be around 5%[124]. So this effect has its origin in the added Co[125], thus reducing M_s as it had been previously suggested. However, the reduction observed here is more dramatic and by arguing with the absence of the (002) reflex for $Mn_{1.9}Co_{0.1}Ga$ on Cr buffer, this might be caused by differing crystallinity through composition-

[116] F. Wu et al., *Appl. Phys. Lett.* **94**, 12, 122503 (2009)

[117] P. Stamenov and J. M. D. Coey, *Review of Scientific Instruments* **77**, 1, 015106 (2006)

[118] H. Kurt et al., *physica status solidi (b)* **248**, 10 (2011), pp. 2338–2344

[119] F. Wu et al., *J. Phys. Conference Series* **266**, 1 (2011), p. 012112

[120] P. Stamenov and J. M. D. Coey, *Review of Scientific Instruments* **77**, 1, 015106 (2006)

[121] H. Kurt et al., *Phys. Rev. B* **83** (2 Jan. 2011), p. 020405

[122] M. Li et al., *Appl. Phys. Lett.* **103**, 3 (2013)

[123] S. Mizukami et al., *Phys. Rev. B* **85** (1 Jan. 2012), p. 014416

[124] S. Mizukami et al., *Phys. Rev. B* **85** (1 Jan. 2012), p. 014416

[125] V. Alijani et al., *Appl. Phys. Lett.* **99**, 22, 222510 (2011)

dependent optimal deposition temperature.
K_U was estimated by using the area difference of the OP and IP curves by integration. It is plotted vs. thickness in fig. 38 (e). All films show a reduction of PMA when decreasing the film thickness. When focusing on the composition with Co and comparing the strained Cr buffered with the Cr/Pt buffered films the PMA loss is less dramatic for the latter and high PMA is retained down to a thickness of 60 Å. It is difficult to separate the effects of reducing thickness from a effect solely related to strain, since the curves in fig. 38 (e) show a constant shift in y-direction throughout the whole range of thickness, which in principle excludes a possible strain dependence. However, it is noticeable that K_U follows since it drops to zero with maximal strain for both compositions. M_s shows this peculiar behavior as well: for $Mn_{1.86}Ga$ it goes to zero at 20 Å and reduces to 100 emu/cm^3 for $Mn_{1.9}Co_{0.1}Ga$ at 60 Å. Strain has an impact on M_s. Unlike K_U it is rather constant for the unstrained films and only shows a drastic reduction with strain. M_s of the $Mn_{1.86}Ga$ films also reduces within the strained region, except for 30 Å where a dominating in-plane moment arises. This could be the result of the formation of super-paramagnetic islands.
Conclusively, this shows that Mn-Ga thin films lose their magnetic anisotropy when reducing thickness. By comparison of a strained with an unstrained composition of Mn-Co-Ga with low Co content it has been demonstrated that additional strain promotes the loss of anisotropy. The function of strain versus film thickness appears to be sensitively dependent on composition, i.e. Co concentration: the region of lattice distortion in $Mn_{1.86}Ga$ ultrathin films on Cr buffer is almost 50 Å shifted towards smaller thicknesses, when compared with $Mn_{1.9}Co_{0.1}Ga$ on a Cr buffer. The strain has been reduced by increasing the Mn-Ga film thickness or by introducing a Pt buffer layer. The integration of Mn-Ga thin films into devices which demands a film thickness of $t < 100$ Å is therefore only possible with the appropriate buffer layer, e.g. Pt. Conclusions drawn from thicker Mn-Ga films, e.g. 300 Å, should be regarded with caution when discussing about actual implementation into devices.

CMS and CFA thin films

This chapter aims at the investigation and optimization of fundamental properties of selected Heusler compounds, i.e. CMS and CFA. The first composite CMS target gave a thin film with 55.8 at% Co, 22.4 at% Mn, 21.8 at% Si via RBS analysis. This information about the differential sputter rates was used to order a composition-corrected CMS target. In contrary, CFA is co-sputtered from three elemental targets. RBS analysis of CFA gave 50.3 at% Co, 25.3 at% Fe, 24.4 at% Al.

Resistivity and magnetization

Polycrystalline CMS and CFA thin films of varying thickness are deposited onto Si/SiO_2 with Ta/Ru seed and annealed with RTA at 370°C for 10 min, which creates a strong (011)-texture with $Q^{T}_{011} = 18$ (see tab. 1). The resistivity at RT is measured by creating a set of different thicknesses and following the sum rule for the sheet resistance $R_\square = \rho / t$, with ρ and t being the film resistivity and thickness, respectively:

$$\frac{1}{R^{\text{tot}}_\square} = \frac{1}{R_\square} + \frac{1}{R^0_\square} = \frac{1}{\rho} t + \frac{1}{R^0_\square} \tag{48}$$

$R^0_\square$ is the sheet resistance of the seed and the cap layers. Plotting $R^{\text{tot}}_\square(t)^{-1}$ and fitting to eq. 48 gives $\rho_{\text{CMS}} = 95\ \mu\Omega\text{cm}$ and $\rho_{\text{CFA}} = 76\ \mu\Omega\text{cm}$, see fig. 40. Bulk CMS exhibits $\rho^{\text{bulk}}_{\text{CMS}} = 20\ \mu\Omega\text{cm}$ at RT[126] and reports for ρ^{film} of thin films range from 25–120 μΩcm at RT[127]. For CFA, epitaxial films obtained $\rho^{\text{film}}_{\text{CFA}} = 50\ \mu\Omega\text{cm}$ for 1000 Å[128] and 40–100 μΩcm for 200 Å thick films[129] - depending on annealing conditions.

When measuring M_s via VSM or BHLooper it is possible to underestimate its value due to magnetically dead layers at interfaces. therefore the uncorrected measured saturation magnetization M^*_s is introduced, which is calculated by using only the magnetic film thickness. Plotting $M^*_s \cdot t$ vs. t, see fig. 41, reveals a magnetically dead layer of $\tilde{t}_{\text{CMS}} = 8$ Å and $\tilde{t}_{\text{CFA}} = 5$ Å, which is used to correct $M^*_s \rightarrow M_s$ as $M_s = M^*_s \cdot t / (t - \tilde{t})$, where t and $\tilde{t}$ are the respective film and magnetically dead layer thickness. Furthermore one obtains bulk M_s with 1004 emu/cc for CMS and 1086 emu/cc for CFA, which is in very good agreement with reported bulk values for CMS[130] and CFA[131] and indicates high crystalline order. The thickness dependence of M_s for CMS is shown in fig. 42 (a). M_s is maintained at a high value down to a critical

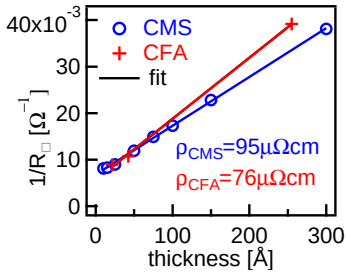

Figure 40: resistivity ρ of CMS and CFA obtained by sheet resistance measurements and fitted to eq. 48.

[126] L. Ritchie et al., *Phys. Rev. B* **68** (10 2003), p. 104430

[127] U. Geiersbach, A. Bergmann, and K. Westerholt, *J. Magn. Magn. Materials* **240**, 1-3 (2002), pp. 546–549, M. P. Raphael et al., *Phys. Rev. B* **66** (10 2002), p. 104429, Y. Sakuraba et al., *Phys. Rev. B* **82** (9 2010), p. 094444

[128] R. Kelekar and B. M. Clemens, *J. Appl. Physics* **96**, 1 (2004), pp. 540–543

[129] I.-M. Imort et al., *J. Appl. Physics* **111**, 7, 07D313 (2012)

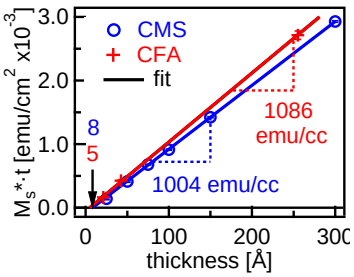

Figure 41: $M^*_s \cdot t$ vs. t of the (011)-textured films on Ta/Ru seed reveals a magnetically dead layer of 8 Å thickness for CMS and 6 Å for CFA. The slope of the fit equals M_s.

[130] M. P. Raphael et al., *Phys. Rev. B* **66** (10 2002), p. 104429

[131] K.H.J. Buschow, P.G. van Engen, and R. Jongebreur, *J. Magn. Magn. Materials* **38**, 1 (1983), pp. 1–22

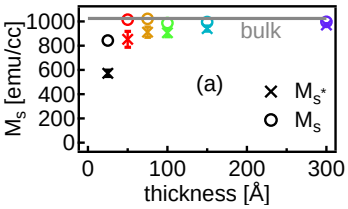

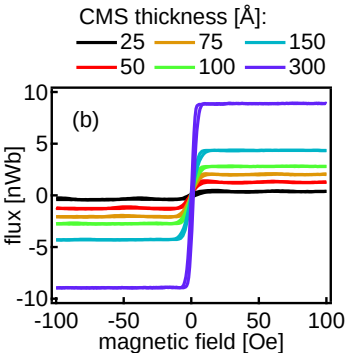

Figure 42: (a): thickness dependence of M_s for CMS films on a Ta/Ru seed layer with corrected values M_s^*; (b): corresponding magnetization curves (BHLooper raw data).

[132] K.H.J. Buschow, P.G. van Engen, and R. Jongebreur, *J. Magn. Magn. Materials* **38**, 1 (1983), pp. 1–22

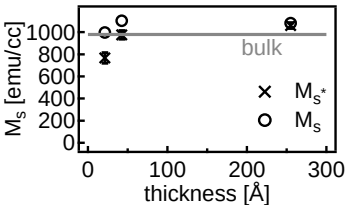

Figure 43: thickness dependence of the uncorrected M_s^* for CFA films on a Ta/Ru seed layer with corrected values M_s.

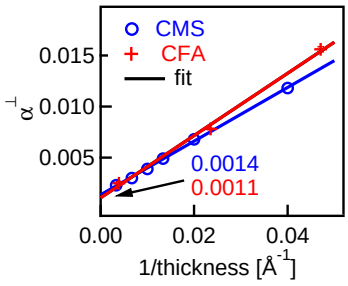

Figure 44: $\alpha^\perp$ scales inversely with the film thickness.

[133] A. Ruiz-Calaforra et al., *J. Appl. Physics* **117**, 16, 163901 (2015)

thickness of 50 Å. M_s for CFA is presented in fig. 43. The slightly larger values for M_s of the CFA thin films ($a_{CFA}^{film} = 5.7$ Å) as compared to bulk ($a_{CFA}^{lit} = 5.73$ Å[132]) might be a result of a smaller lattice constant in the films or a partial crystallization.

Magnetization dynamics and anisotropies

In- and out-of-plane FMR spectra for CMS on the Ta/Ru seed are shown in fig. 45. The evaluation of the CFA on the same seed is completely analogous and will not be shown here. Fig. 44 (b) shows the intrinsic damping of CMS and CFA for different thicknesses from OP FMR measurements. Similar behavior is reported by *Ruiz-Calaforra et al.*[133], where the intrinsic damping parameter is found to be dependent on the film thickness and one can phenomenologically write $\alpha_{eff} = \alpha_0 + b/t$ to fit for the bulk intrinsic damping parameter α_0, with a constant b and film thickness t. The intercept with the ordinate designates α for an infinite sample thickness (bulk), which is 0.0014 for CMS and 0.0011 for CFA.

As expressed by eq. 32 the total perpendicular anisotropy is expected to consist of a bulk and interface contribution $K_U^\perp = K_b^\perp + 2K_s^\perp/t$ with two equally contributing Ru/Heusler interfaces. By making use of the definition of M_{eff}, as already introduced for eq. 28, one obtains

$$4\pi M_{eff} = 4\pi M_s - \frac{2K_b^\perp}{M_s} - \frac{4K_s^\perp}{M_s t}. \tag{49}$$

By plotting M_{eff} vs. t^{-1} one obtains $K_s^\perp$ from the slope and $K_b^\perp$ from comparing the intercept value at the ordinate with M_s which has been previously measured with VSM/BHLooper, see fig. 46. One obtains a comparably small bulk contribution $K_b^\perp = -5 \cdot 10^5$ erg/cc and a dominating surface contribution $K_s^\perp = 0.24$ erg/cm^2 for CMS. CFA exhibits a similar surface anisotropy $K_s^\perp = 0.21$ erg/cm^2. $K_b^\perp$ of CFA is twice as large as for CMS but it important to notice that $K_b^\perp$ specifically includes a large error from this fitting method since it gets derived from the small difference of M_{eff} and M_s and thus relies on a very accurate measuring of these quantities.

To investigate the magnetocrystalline anisotropies, a 180 Å CMS film is epitaxially grown on (001)-MgO substrates. A 20 Å MgO seed layer is grown via RF-sputtering directly onto the MgO substrate before the deposition of the Heusler. No other buffer layer material is used and 20 Å Ru serve as capping layer. Deposition is at RT. Ex-situ post-annealing at 400°C for 5 hours at 10 kOe magnetic field along the $[1\bar{1}0]$ in-plane direction of the Heusler induces crystallization. Fig. 47 shows a $2\theta/\omega$ XRD scan for the MgO/CMS film. Only the (002) and (004) CMS peaks and the MgO substrate reflex are clearly visible and the lattice constant is 5.64 Å. The in-plane angular FMR spectrum for CMS at $f = 20$ GHz is shown in fig. 48. It is fitted to eq. 29 and using a $\varphi_0 = 10°$

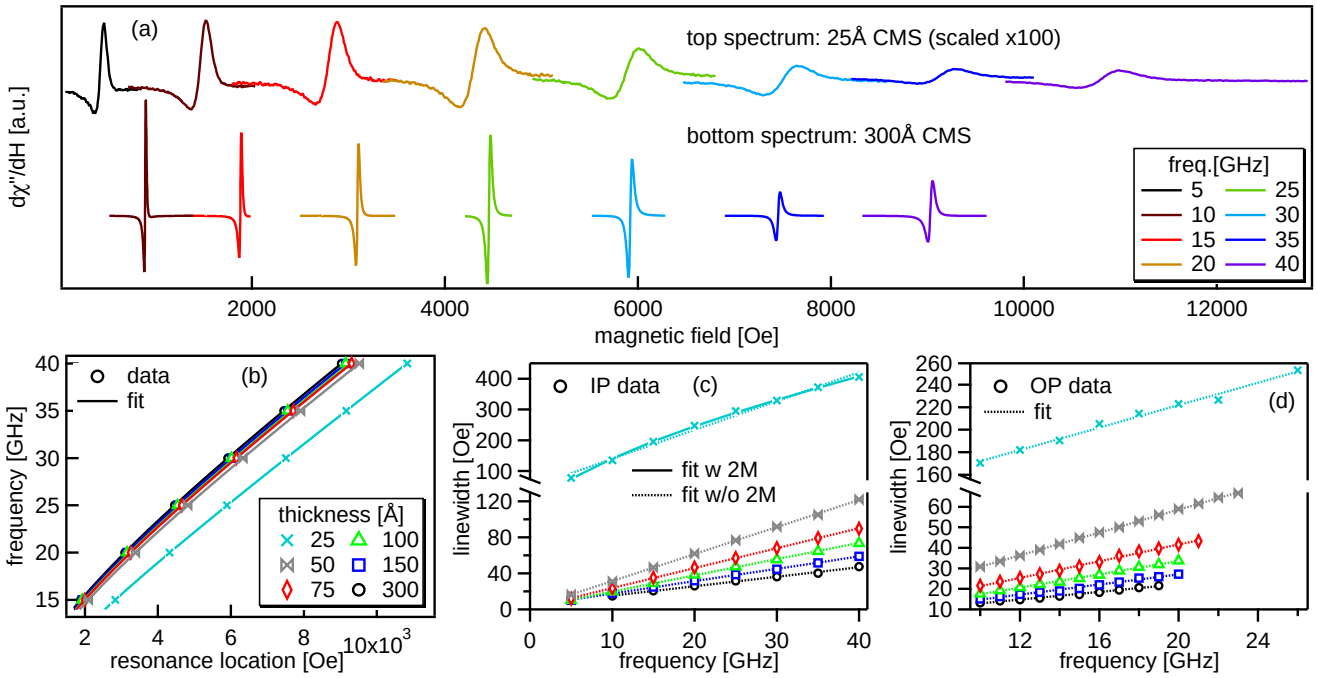

Figure 45: FMR measurements of CMS on Ta/Ru seed with different thickness ranging from 25-300 Å; (a): two exemplary FMR spectra (raw data, offset) for 25 Å and 300 Å thick samples; (b): IP frequency vs. resonance location plot and fit to obtain M_{eff} and γ following eq. 28. OP data, which is fitted by eq. 39 is not shown here; (c): IP linewidth ΔH vs. frequency to obtain α and $\Delta H_{0,\text{II}}$ by fitting to eq. 33. For 25 Å the two-magnon scattering term $\Delta H_{2\text{M}}$ is included due to a large curvature; (d): OP linewidth plot and fit via eq. 40.

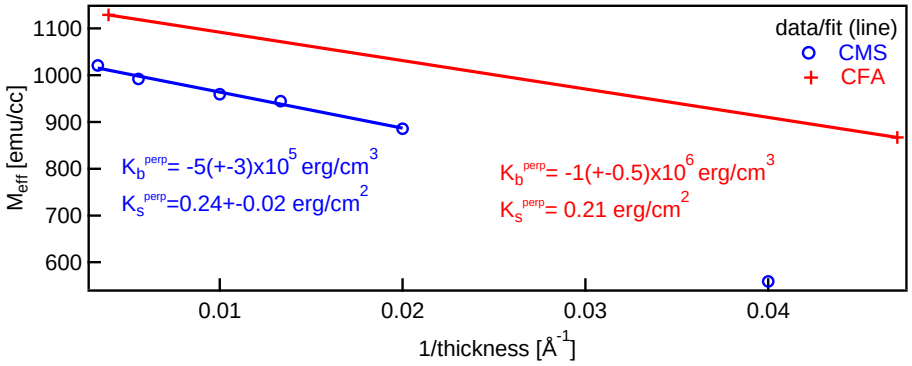

Figure 46: M_{eff} from FMR IP measurements. The sample with $t = 15$ Å is excluded from the fit due to degradation of M_{s} for $t < 50$ Å, as indicated in fig. 42 (a).

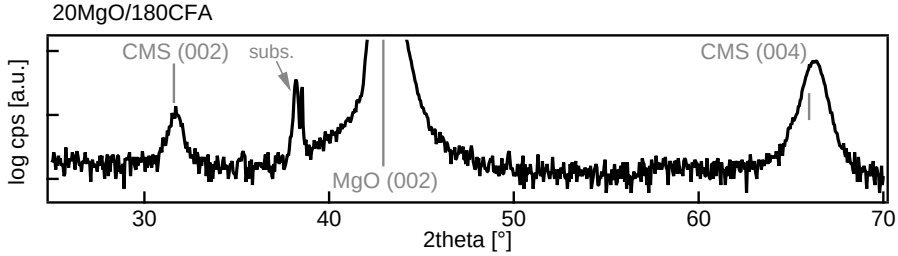

Figure 47: $2\theta/\omega$ XRD scan of the MgO/CMS film, discussion see text.

positioning offset caused by the measurement setup. Noticable is also the periodicity of absorption linewidth with the in-plane angle, hinting towards a fourfold anisotropy of a damping contribution. In addition

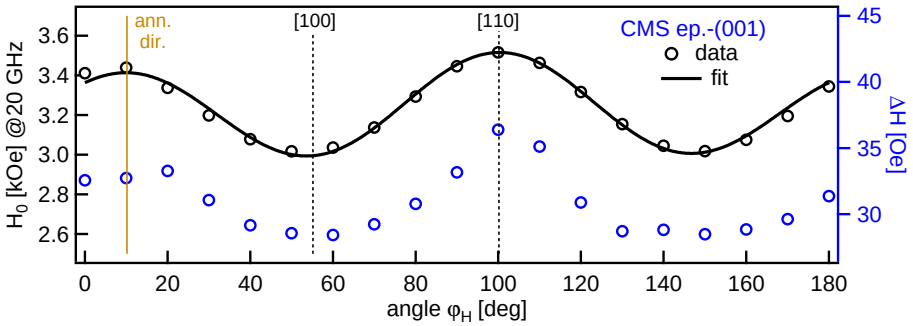

Figure 48: in-plane angular FMR scans of CMS. The fit gives for CMS: $K_U^{II} = 3 \cdot 10^4$ erg/cc and $K_1^{II} = 1.3 \cdot 10^5$ erg/cc.

to the epitaxial samples, two types of oriented polycrystalline films are grown on Si/SiO_2 to have a set of three differently grown CMS samples: The most accessible texture using close-to-standard industrial parameters: (011). And the developed (001)-texture with MgO seed compared to the highest structural quality the (001)-MgO substrate based epitaxial samples. Tab. 5 gives a comprehensive overview over the results of the investigated properties.

Table 5: magnetic parameters obtained by BHLooper, VSM and in- and out-of-plane FMR spectra for epitaxial and polycrystalline-textured CMS thin films. Different underlayers are utilized to realize the two textures. Hard/easy axis are along and perpendicular the annealing direction (in the case of field anneal). Since no 180CFA film for (011)-texture is available, 250CFA is presented instead. $K_b^\perp$ and $K_s^\perp$ are extracted from thickness dependent measurements on multiple samples as explained in the text. *fit omits in-plane anisotropy term. Unavailable data is denoted with '-'.

Data	**(001)-epitaxial**	**(011)-textured**		**(001)-textured**
	180CMS	180CMS	250CFA	180CMS
M_s [emu/cc]	1055	997	1081	938
H_c [Oe] hard/easy	10/1	0.5	12	10
g^{II}	2.032	2.025	2.082	2.041
M_{eff}^{II} [emu/cc]	957	1003*	1157	1406*
K_U^{II} [10^4 erg/cc]	3	-	-	-
K_1^{II} [10^5 erg/cc]	1.3	-	-	-
α^{II}	0.0025	0.0034	0.0042	0.0061
2M [Oe] (II only)	0	0	0	0
ΔH_0^{II} [Oe]	5	4	39	9
$g^\perp$	2.000	2.006	-	-
$M_{eff}^\perp$ [emu/cc]	1007	981	-	-
$K_U^\perp$ [10^5 erg/cc]	1.3	*see* $K_b^\perp$, $K_s^\perp$	*see* $K_b^\perp$, $K_s^\perp$	-2.8
$K_1^\perp$ [10^4 erg/cc]	-6.6	-	-	-
$\alpha^\perp$	0.0019	0.0030	0.0025	-
$\Delta H_0^\perp$ [Oe]	4	2.5	52	-
$K_b^\perp$ [10^5 erg/cc]	-	-5	-10	-
$K_s^\perp$ [erg/cm^2]	-	0.24	0.21	-

Exchange coupling

Interlayer exchange coupling (IEC) is the interaction of two bottom/top ferromagnetic layers separated by an ultrathin *non-magnetic* (NM) spacer, $FM_b/NM/FM_t$. Its consequence is a specific angle between the magnetizations of FM_b and FM_t. The discovery of IEC[134] and its interconnectedness with the GMR *effect*[135] triggered an intense interest in the studies of metallic layered structures. The decisive breakthrough of the IEC came with the discovery of its oscillatory nature that dependents on the spacer type and thickness[136].

There are several reports on IEC with Cr spacer layers, especially on the large biquadratic coupling of (001)-epitaxial CMS/Cr/CMS[137] and CMS/Cr/Fe[138]. To investigate IEC with the Heusler CMS as FM_b and FM_t and with Cr as NM, two (011)-textured reference CMS films are deposited onto a 30Ta/20Ru seed on amorphous substrates, both with an adjacent 17 Å Cr layer. The films are annealed in-situ at mild 370°C for 60 seconds to minimize Cr interdiffusion[139]. The magnetization loops are square both for low (BHLooper) and high (VSM) external magnetic fields, see fig. 49 (a). Then a series of $CMS_b/Cr/CMS_t$ sandwiches are created, where the thicknesses of Cr or CMS_t are varied from 8-67 Å and 50-200 Å, respectively. Fig. 49 (b) shows the low field BHLooper magnetization curves of sandwiches for different Cr thicknesses. Apparently the magnetization of some films seems unsaturated within the field range and even feature some curvature. One could argue now that

[134] P. Grünberg et al., *Phys. Rev. Lett.* **57** (19 Nov. 1986), pp. 2442–2445

[135] M. N. Baibich et al., *Phys. Rev. Lett.* **61** (21 Nov. 1988), pp. 2472–2475

[136] S. S. P. Parkin, N. More, and K. P. Roche, *Phys. Rev. Lett.* **64** (19 May 1990), pp. 2304–2307

[137] S. Bosu et al., *Phys. Rev. B* **81** (5 2010), p. 054426

[138] S. Bosu et al., *IEEE Transactions on Magnetics* **44**, 11 (Nov. 2008), pp. 2620–2623

[139] O. Gaier et al., *J. Appl. Physics* **103**, 10, 103910 (2008)

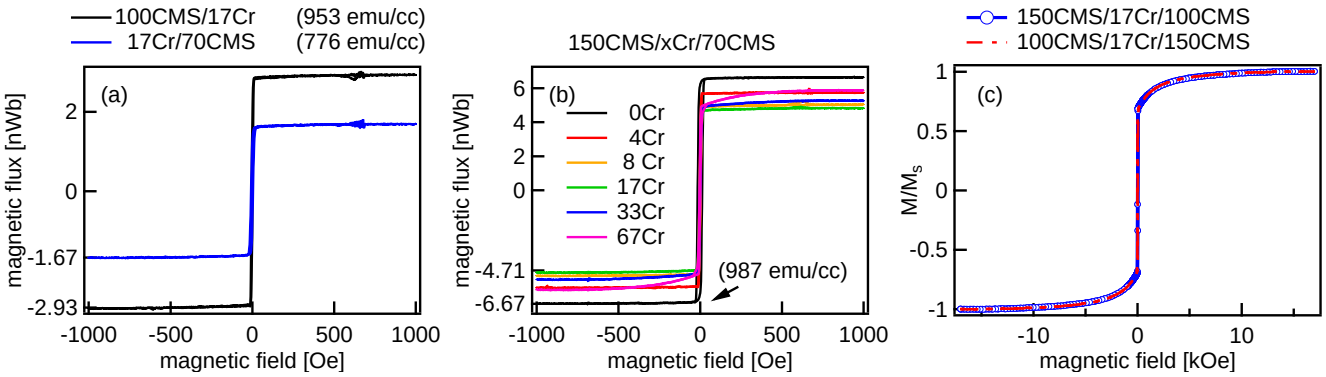

Figure 49: BHLooper raw data of (a): CMS with a Cr cap or Cr buffer layer. The saturation field is about 20 Oe; (b): data for CMS/Cr/CMS trilayers with varying Cr spacer thickness. Only the film without Cr insertion can be saturated within 1000 Oe; (c): Swapping the order of the CMS layers has no influence on the curve shape for high field VSM measurements.

the decreased magnetic flux around zero field and the slow saturation as soon as Cr is inserted is attributed to a deteriorated quality of CMS_t because it is grown on Cr and not on Ta/Ru. However, the loop shape of the reference sample 17Cr/70CMS rules this out. To further disprove the argument of film quality deviations, high field $M(H)$ curves of $150CMS_b/17Cr/100CMS_t$ and $100CMS_b/17Cr/150CMS_t$ are shown in fig. 49 (c). Both curves in the graph are identical, thus there is no differing quality between the CMS layers. From this follows that CMS_b is exchange coupled to CMS_t.

In order to evaluate the type and strength of the IEC, the energetic situa-

tion in the stack is analyzed. Initially, domain walls are neglected and it is assumed that the moment of each FM is uniform and confined to the sample plane and evolves into the energy minimum. The total energy E of an exchange coupled $FM_b/NM/FM_t$ can then be expressed by the *Stoner-Wohlfarth model* which includes terms for exchange coupling:

$$\begin{aligned} E &= E_K + E_Z + E_J \qquad \text{,where} \\ E_K &= K_b t_b \sin^2\alpha\cos^2\alpha + K_t t_t \sin^2\beta\cos^2\beta \\ E_Z &= -M_b t_b H\cos\alpha - M_t t_t H\cos\beta \\ E_J &= -J_1\cos(\alpha-\beta) + J_2\cos^2(\alpha-\beta)\,. \end{aligned} \tag{50}$$

E_K, E_Z and E_J are the magnetocrystalline anisotropy, Zeeman and exchange energy, respectively. J_1 and J_2 give the strength of the bilinear and biquadratic exchange coupling and α, β are the angles $\angle\mathbf{HM}_{b/t}$, respectively. M_b and M_t are the saturation magnetizations of the respective layer. From the phenomenological equation for E_J it can be seen that J_1 will align $\mathbf{M}_b \uparrow\downarrow \mathbf{M}_t$ ($J_1 < 0$) or $\mathbf{M}_b \uparrow\uparrow \mathbf{M}_t$ ($J_1 > 0$)[140].

The physics behind J_1: The Fermi surface of the spacer layer material governs the coupling periods. Here, a critical spanning vector (perpendicular to the interface) connects slices of the spacer Fermi-surface in an extended zone scheme. Spacer thickness variations can then cause long and short range exchange oscillations, corresponding to the length of these spanning vectors. The coupling strengths and periods ultimately depend on the description of the electronic structure of spacer and ferromagnets. An extrinsic mechanism for positive J_1 is pinhole-coupling, since a break in the spacer gives rise to direct exchange coupling.

The physics behind J_2: There is an intrinsic origin of biquadratic coupling as a higher order term in the model used to explain bilinear coupling, but this term is usually negligibly small[141]. *Slonczewski* proposed that interfacial loose spins of the FM at the FM/NM interface are weakly coupled to the remainder of the FM and thus declares this type of biquadratic coupling of intrinsic nature[142]. The magnitude is e.g. <0.1 erg/cc at RT for Fe/Al/Fe or Fe/Au/Fe epitaxial thin films.
Another separate extrinsic origin is based on thickness fluctuations[143] and the magnitude of J_2 is proportional to ΔJ_1, which is the change in the amount of bilinear coupling when going from odd to even ML of spacer thickness[144]. When the thin film interfaces are not atomically smooth, the J_2 contribution is therefore the effective coupling due to random fluctuations of the magnetizations around their average direction due to terrace-like spacer growth or *uncorrelated* roughness of both interfaces[145]. The effect is also termed *magnetostatic biquadratic coupling*, where the orange peel effect is zero and the fringing fields of e.g. FM_b minimize the field energy by aligning the magnetization of FM_t perpendicularly. The effect is of the order ~ 0.01 erg/cm^2 for amorphous spacer layers[146].
When the bilinear coupling is negative, pin holes can give rise to a biquadratic contribution. This mechanism is similar to the origin of J_2

[140] to detect the $\uparrow\uparrow$ case with VSM one needs a different stack design, which includes either a direct exchange coupled AFM/FM part or a FM1/NM1/FM2/NM2/FM3 stack with different coupling through NM1 and NM2.

[141] D. M. Edwards, J. M. Ward, and J. Mathon, *J. Magn. Magn. Materials* **126** (1-3 1993), pp. 380–383

[142] J. C. Slonczewski, *J. Appl. Physics* **73**, 10 (1993), pp. 5957–5962

[143] J. C. Slonczewski, *Phys. Rev. Lett.* **67** (22 Nov. 1991), pp. 3172–3175

[144] B. Heinrich and J. F. Cochran, *Adv. Phys.* **42**, 5 (1993), pp. 523–639

[145] S. O. Demokritov, *J. Phys. D: Appl. Phys.* **31**, 8 (1998), p. 925

[146] P. Fuchs et al., *Phys. Rev. B* **55** (18 May 1997), pp. 12546–12551

due to positive thickness-fluctuations, but instead of a distribution of roughness it requires a specific distribution of pin-holes[147].
Uncorrelated roughness creates a coupling which becomes smaller with decreasing spacer thickness. The opposite proportionality with t_s holds for the interaction described by *Slonczewski*.
M(H) loops are generated via a numerical simulation based on the Stoner-Wohlfarth model using two major energetic contributions from eq. 50, while the anisotropy term will be neglected for non-epitaxial films. The simulation that fits the experimental data best is chosen via the method of least squares. In order to receive a good fit, E_J needs to be adjusted by using a more general, phenomenological expression for E_J[148]:

[147] J. F. Bobo et al., *Phys. Rev. B* **60** (6 Aug. 1999), pp. 4131–4141

[148] J. C. Slonczewski, *J. Appl. Physics* **73**, 10 (1993), pp. 5957–5962

$$E_J = \sum_{i=1}^{n} J_i \cos^i(\alpha - \beta) \tag{51}$$

Normalized VSM M(H) loops for the same samples as in fig. 49 (b) are

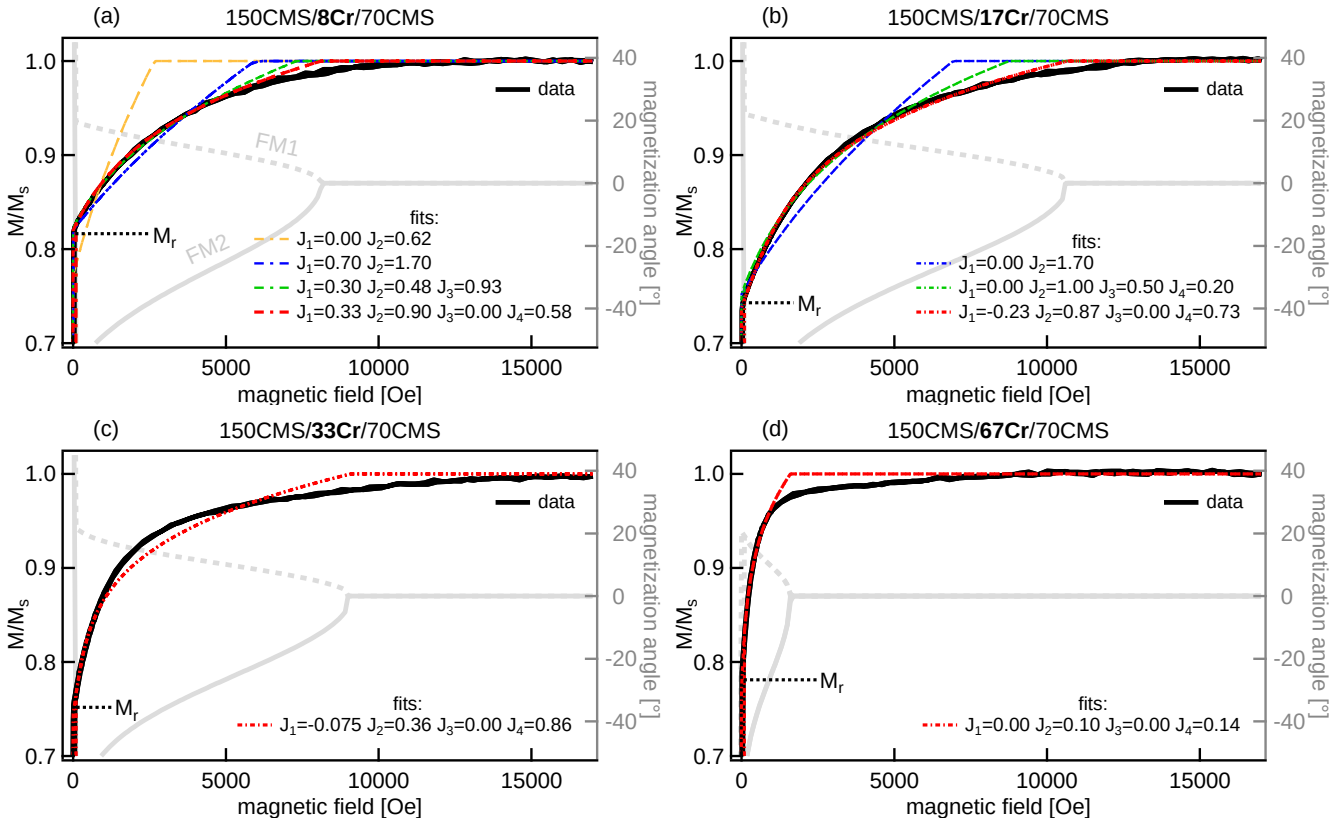

Figure 50: normalized VSM data (only one quadrant shown for visibility) and fits via eq. 50 using the expression in eq. 51 for the total energy E. From (a)-(d) there is an increasing t_{Cr}. The fits only converge reasonably by including higher order coupling contributions J_3 and J_4 as shown in (a) for t_{Cr} = 8 Å. Units of J_i are in erg/cm^2. The relative magnetization angle $\alpha - \beta$ for the best fit using parameters up to the fourth order (red) is plotted as well.

shown for one quadrant in figs. 50 (a)-(d). The graphs contain the best fits for the M(H) curves using different values for J_i, where the order is extended up to $i = 4$. It has to be mentioned, that $J_3 < 0$ would generate antiparallel coupling which doesn't make physical sense. Therefore parameter J_3 is restricted to $J_3 > 0$ during the fit. *Monchesky et al* also

[149] T. L. Monchesky et al., *Phys. Rev. B* **60** (14 Oct. 1999), pp. 10242–10251

reported bicubic (J_3) coupling on GaAs-subs./Fe/Cu/Fe trilayers[149] in a similar circumstance as here: as a need to explain and fit their experimental data. The red curve in figs. 50 (a)-(d) which floats all four coupling contributions shows the best agreement with the experimental data. It is peculiar that the fit result for the bicubic coupling is $J_3 = 0$ for all samples. Remanence M_r depends on the Cr thickness and hints towards $J_1 \neq 0$ for 17-67 Å thick spacers before it crosses zero within 8-17 Å for t_s. This is likely due to the development of a pin-hole free spacer layer with increasing spacer thickness. Fig. 51 summarizes J_i vs. t_{Cr}.

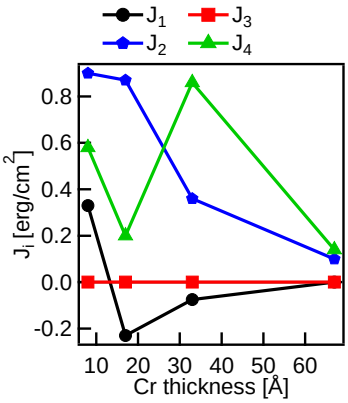

Figure 51: VSM Fitting results from fig. 50 for the coupling parameter up to the fourth order using the Stoner-Wohlfarth model via eq. 50.

[150] OOMMF website

The Stoner-Wohlfarth model assumes single domain magnetic states, which is generally not a good approximation for polycrystalline thin films. Therefore, a micromagnetic solver, i.e. the *Object Oriented MicroMagnetic Framework*[150] (OOMMF) is utilized to simulate hysteresis curves for multi domain films. Here local M_s canting (or fanning) around an average magnetization direction is taken into account. The cell size within the mesh (x,y,z) is (10,10,1) with units in nm. The trilayer stack is 400 nm long and 200 nm wide. Besides J_1 and J_2, another parameter serves as an input: A, which is the 6-nearest neighbor exchange interaction integral that is proportional to the exchange stiffness of the magnetic material. In contrast to J_1 and J_2, which resemble the coupling across a nonmagnetic spacer, A is the local sum of the direct exchange interaction acting on a defined cell by its surrounding neighbors. Example simulations shown in fig. 52 reveal the impact of the three parameters J_1, J_2 and A: the remanence is determined primarily by J_1 while the curvature jointly depends on J_2 and A. The saturation field is dependent on all three parameters.
For $A \to \infty$ all cells are tightly coupled and form a single domain where the result of the simulation coincides with the analytical expression given by the Stoner-Wohlfarth model. For smaller A the curvature increases. With the right choice of these three input parameters the experimental hysteresis loops can be modeled, see fig. 53. With in-

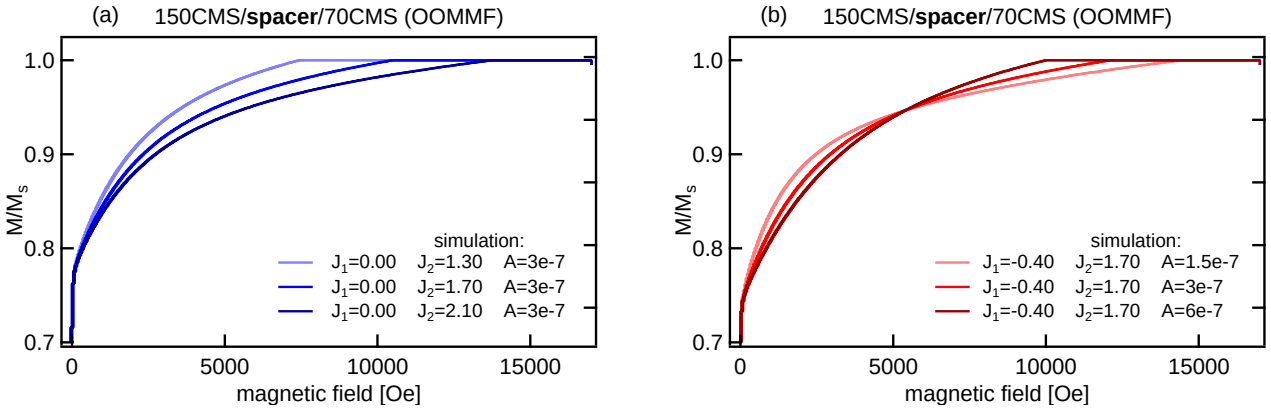

Figure 52: OOMMF hysteresis simulations with different values for input parameters J_1, J_2 and A; (a): FM layers are coupled via biquadratic coupling of differing strength and fixed nearest neighbor exchange; (b): fixed J_1 and J_2 with varying nearest neighbor exchange effecting the curvature of the hysteresis. Units are erg/cm^2 for J_i and erg/cm for A.

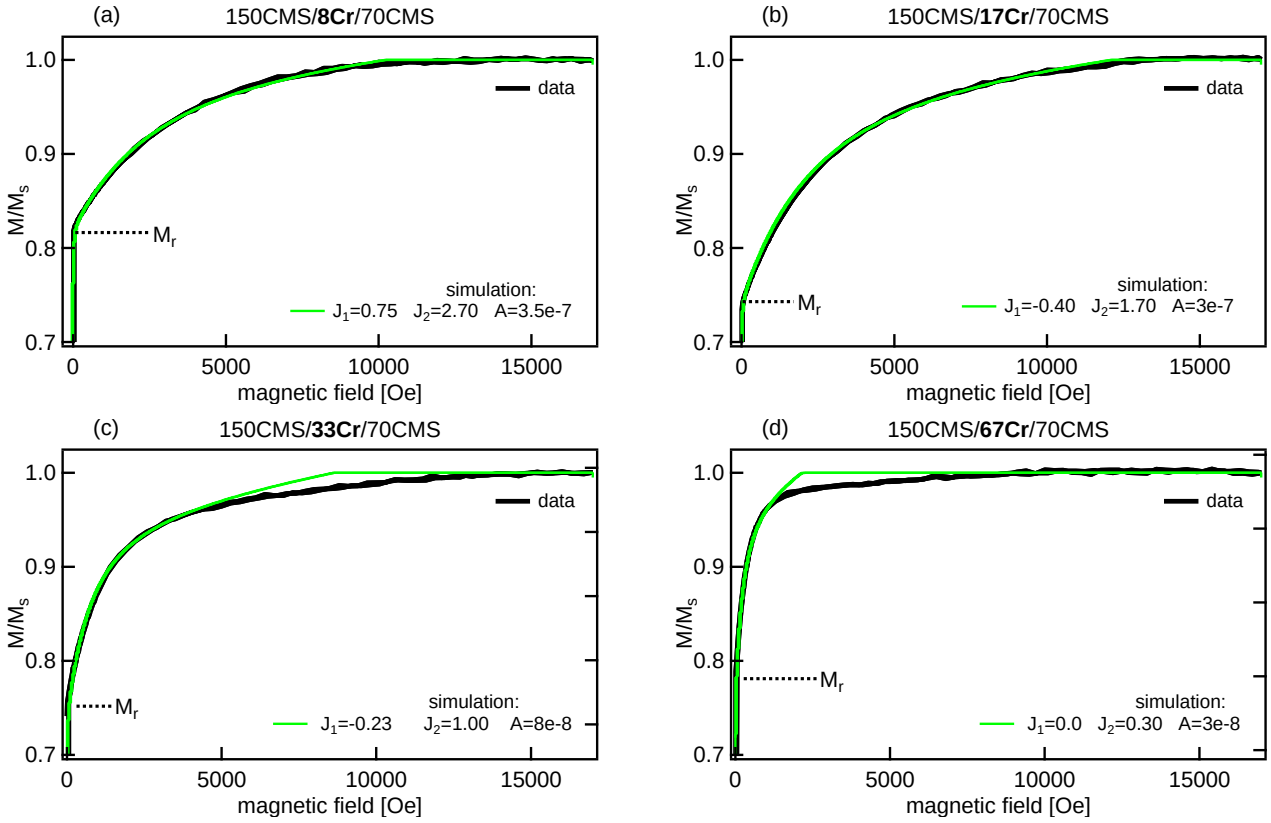

Figure 53: same experimental data as in figs. 50 (a)-(d). Multiple simulations via OOMMF led to an optimized choice of parameters to model the VSM data. Units are erg/cm^2 for J_i and erg/cm for A.

creasing Cr spacer thickness 33 Å $\rightarrow$ 67 Å however the optimal choice of a set for J_1, J_2 and A reveals a systematical mismatch with the data: experimentally larger curvature with increasing spacer thickness indicates decreasing A while a flat tail towards the saturation field hints sufficiently large J_2. Simulated curves with higher J_2 however generally feature a steeper slope. Since one would further expect a heavily reduced J_2 at $t_s = 67$ Å, the measured flat saturation tail has its origin most likely in spatial coupling strength fluctuations. This complicates modeling via OOMMF since the program is only able to assign global and uniform J_1/J_2 coupling strengths to the trilayer and A to the interfaces. A lower estimate for J_2 and A is chosen in the simulations in figs. 53 (c) and (d) which appropriately models the curvature at low magnetic fields. Fig. 54 displays parameters for the simulations that fit the experimental data best. Biquadratic coupling decreases linearly with thickness while the bilinear term experiences a change of sign around $t_{Cr} \approx 14$ Å. A also decreases with increasing thickness of the spacer layer.

Conclusively, the signatures in hysteresis loops which can be mistaken for higher coupling contributions J_i with $i > 2$ of FM/NM/FM trilayers are merely a consequence of finite exchange stiffness which itself is a result of film imperfections such as grain boundaries that give rise to smaller magnetic domains. Due to the limitations of the Stoner-Wohlfarth model, a micromagnetic simulation is recommended with

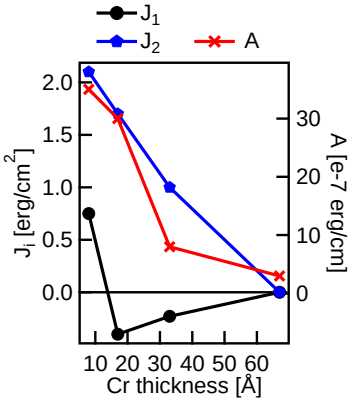

Figure 54: best choice of parameters J_1, J_2 and A to model the VSM data via OOMMF simulation.

results appropriately explaining the measured data.

The magnitude of J_2 observed here is comparable with reports on epitaxial CMS/Cr/Fe[151] and CMS/Cr/CMS[152] trilayers, the range of t_{Cr} with active coupling is however larger here.
The observed non-oscillatory behavior of J_2 speaks for the extrinsic residual interface roughness contribution caused by roughness/terraces (long-period coupling[153]) as suggested by *Slonczewski* and not for the short-period intrinsic J_2 as observed for e.g. Fe/Cr/Fe atomically smooth epitaxial samples grown by MBE[154]. The large magnitude however is likely caused by the specific nature of Cr. Strictly speaking Cr is not non-magnetic, but rather tends to exhibit bulk antiferromagnetism in the form of incommensurate spontaneous colinear spin density waves. In other words, atomic monolayer steps cause larger oscillation amplitudes of the exchange coupling[155] than a non-magnetic spacer. Therefore, the magnetostatic biquadratic coupling based on terraces that cause a situation where bilinear coupling is frustrated can be expected to be magnitudes larger with Cr. Interestingly, 90° coupling has also been observed for (001)-epitaxial $Co_2FeAl_{0.5}Si_{0.5}$/Cr/$Co_2FeAl_{0.5}Si_{0.5}$ samples[156], but a factor of 20 smaller, probably due to smoother interfaces. Furthermore the same stacks but polycrystalline on SiO_2 only exhibit weak *antiferromagnetic* (AFM) coupling.
Exchange coupling through roughness generally constitutes a problem for polycrystalline CPP-GMR spin-valves. For example in the case of *pseudo spin valves* (PSV) where there is no AFM layer that pins the *reference layer* (RL) through exchange coupling. There the *antiparallel* (AP) state is achieved with shape anisotropy by patterning the top layer in the form of an elongated ellipsoid or rectangle. Uncorrelated roughness coupling will disturb the switching. For very smooth films of course, IEC can be used to obtain the AP state via negative J_1, but this is very difficult to achieve with polycrystalline thin films. Furthermore, the two prominent spacer layer materials, Ag and Cr, each have a critical disadvantage in combination with CMS: during growth, Ag strives towards island agglomeration which drastically increases roughness and demands for a comparably thicker spacer to meet film coalescence. And a Cr spacer renders unprecedented 90° coupling strengths.
However, the strength of these coupling contributions could be interesting for applications. It could potentially be utilized in a field stabilizing TMR/GMR sensor, where the *free layer* (FL) FM1 is 90° coupled to an FM2 layer with higher $M_s \cdot t$. FM2 then is field-stabilized by the conventional *hard-bias*.

Magnetostatic coupling

This type of coupling is based on the stray fields produced by FM layers and is therefore not limited only to the FM_b/NM/FM_t multilayer type. 'Magnetic poles' at the edges of e.g. a patterned MTJ give rise

[151] S. Bosu et al., *IEEE Transactions on Magnetics* **44**, 11 (Nov. 2008), pp. 2620–2623

[152] H. Wang et al., *Appl. Phys. Lett.* **90**, 14, 142510 (2007)

[153] U. Rücker et al., *J. Appl. Physics* **78**, 1 (1995), pp. 387–391

[154] B. Heinrich and J. F. Cochran, *Adv. Phys.* **42**, 5 (1993), pp. 523–639

[155] J.C. Slonczewski, *J. Magn. Magn. Materials* **150**, 1 (1995), pp. 13–24, H. Zabel, *J. Phys.: Condens. Matter* **11**, 48 (1999), p. 9303

[156] T. Furubayashi et al., *J. Appl. Physics* **105**, 7, 07C305 (2009)

to a nonuniform demagnetizing field which depends specifically on the geometry and size of the device. For nanoscale lateral dimensions this effect can be significant[157] and has to be countervailed by e.g. a magnetically compensated stack design[158]. For unpatterned films this magnetostatic effect is zero.

Static contributions to the bilinear coupling (J_1) can also be triggered by *correlated* surface roughness of either FM_b or NM, where bumps of the rough surface create magnetic poles which give rise to a fringing field[159]. This *orange-peel effect* leads to interlayer coupling for MTJs that has its origin in the interface topology of multilayers. The roughness can be described with a more or less correlated profile (contrary to the uncorrelated roughness model of J_2). Therefore by symmetry, two parallel magnetic layers have a lower field energy when their fringing fields oppose each other. Then their magnetizations are parallel, fig. 55, and the contribution to J_1 is thus positive. It can effectively reduce the antiparallel RKKY interaction which has even been reported for perpendicular spin valves[160]. This correlated interface roughness can be approximated by a sinusiodial waviness and following the field model of Néel the dipolar orange-peel coupling is given by[161]:

$$H_N(A,\lambda) = \frac{\pi^2 A^2}{\sqrt{2}\lambda t_{fl}} M_s \exp\left(-\frac{2\pi\sqrt{2}t_s}{\lambda}\right), \qquad (52)$$

where A and λ are the amplitude and the wavelength of the roughness profile. t_{fl} and t_s are the thicknesses of the *free layer* (FL) and spacer, respectively. At a given A the coupling has a maximum at $\lambda_0 = 2\pi\sqrt{2}t_s$. Fig. 56 shows the coupling field strength for different choice of parameters in eq. 52.

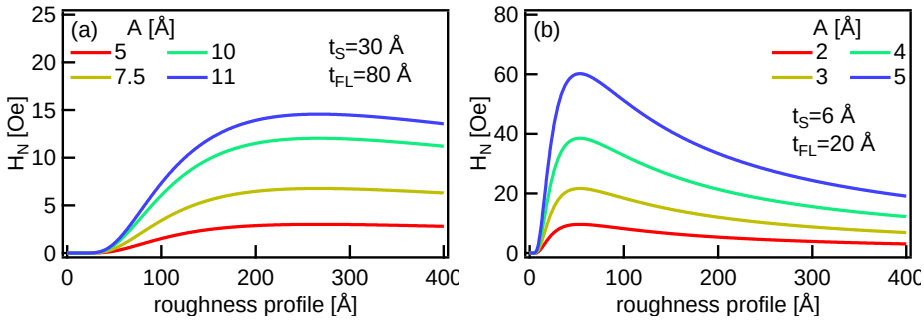

Figure 56: orange peel effect for different parameters for eq. 52, using typical (a) CPP-GMR and (b) TMR device film thicknesses and $M_s = 1000$ emu/cc. The effect is larger for TMR devices, since typically small, e.g. $t_{fl} \sim 20$ Å and $t_s \approx 6$ Å increase H_N, following eq. 52.

Exchange coupling in CPP-GMR stacks

A CPP-GMR pseudo-spin valve stack (no pinning, see p. 97) is deposited onto the record-Q^T_{001}, low-RA seed/buffer combination (see tab. 1). The complete stack is depicted in fig. 57. Its spacer layer is Ag with a thickness ranging from 17 to 43 Å. Ag is *cryo-deposited* at -125°C, as described earlier. The finished stack is in-situ annealed via RTA at 400°C

[157] T. Dimopoulos et al., *J. Magn. Magn. Materials* **242-245**, 1 (2002), pp. 512–514

[158] M. Yoshikawa et al., *J. Appl. Physics* **97**, 10 (2005), 10P508

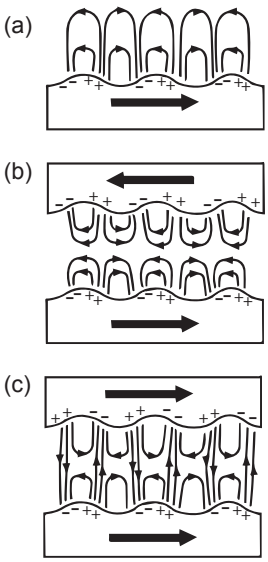

Figure 55: (a): roughness of a film with uniform magnetization gives rise to a fringing field with the pluses and minuses denoting magnetic poles; (b): antiparallel alignment of two films with correlated roughness and (c): parallel alignment, where the field lines cross the spacer, effectively reducing field energy, which is the reason why this configuration is favored.

[159] D. Dexin Wang et al., *J. Appl. Physics* **93**, 10 (2003), pp. 8558–8560

[160] J. Moritz et al., *Europhys. Lett.* **65**, 1 (2004), p. 123

[161] B. D. Schrag et al., *Appl. Phys. Lett.* **77**, 15 (2000), pp. 2373–2375

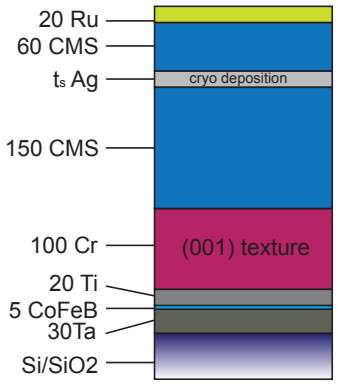

Figure 57: CPP-GMR pseudo-spin valve stack using CMS as top and bottom FM layer with variable t_s.

for 600 seconds. Low field MOKE-measurements in the range $[-500, 500]$ Oe are shown in fig. 58 (a). The normalized Kerr angle is defined as $\alpha = M(H)/M_s$. The shapes of the curves feature coupling signatures: at field strengths ± 5 Oe there is a visible kink. In order to visualize this kink the derivative dH/dα is shown in fig. 58 (b). The remanence is plotted in fig. 58 (c). Since for the bottom $t_b^{CMS} = 150$ Å and for the top $t_t^{CMS} = 60$ Å, 90° pure biquadratic coupling would lead to a normalized remanence $M_r/M_s \approx 0.78$, while only bilinear AFM coupling would give $M_r/M_s = 0.43$. Bilinear FM coupling is not possible to estimate with this stack, but its contribution would lead to $M_r/M_s > 0.78$.
The kink around $M/M_s \approx 0.43$ for all t_s of Ag suggests 180° coupling and the general trend of $M_r/M_s \approx 0.78$ can be explained by an additional small uncorrelated 90° coupling contribution at zero field. Another possible explanation for the shape of the MOKE curves in fig. 58 (a) is simply an underlayer-dependent film quality, since the bottom CMS grows on Cr, while the top CMS is deposited onto Ag. To test this argument, another trilayer with $t_s^{Ag} = 30$ Å and bottom $t_b^{CMS} = 100$ Å is fabricated.

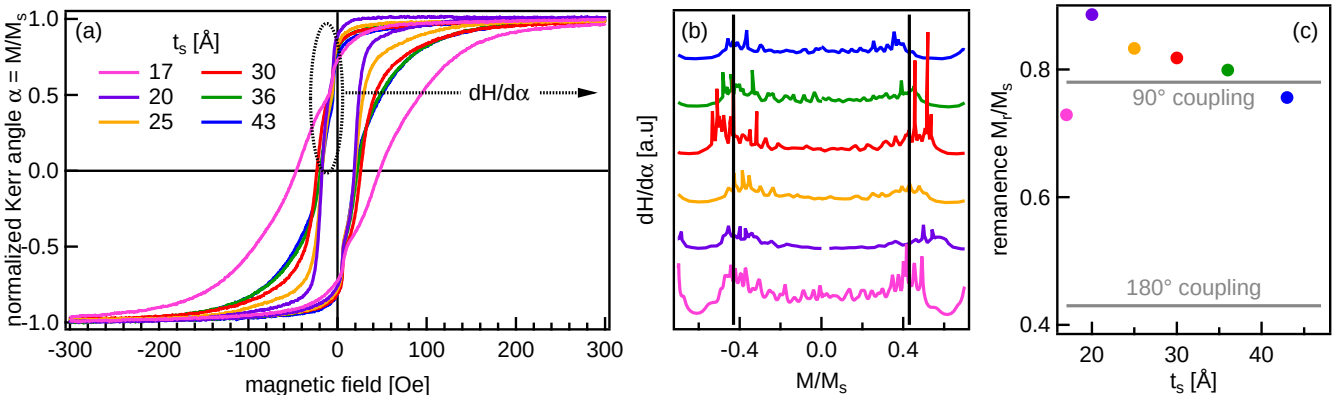

Figure 58: (a): low-field MOKE curves for the stack depicted in fig. 57 for different t_s of Ag. The curves feature possible coupling signatures; (b): derivative dH/dα shows kinks around -5 Oe and +5 Oe that are on the level of 180° bilinear coupling and (c): the remanence suggests possible 90° biquadratic coupling.

Additionally, 30 Å Ag cryo-deposited insertion layers sandwiching the FM_b/NM/FM_t part of the stacks are inserted at -125°C, see fig. 59 (b). The deposition conditions for each layer are identical to the stack in fig. 57, wherefore no considerable change in FM/NM interface roughness is expected. The normalized MOKE signal in fig. 59 shows no kink. Therefore it can be concluded that the kink is a Cr underlayer effect on the lower CMS electrode and not a result of bilinear interlayer coupling. Furthermore both curves in fig. 59 (a) feature the same remanence, which would not be the case for active biquadratic coupling because the two stacks have different bottom t_{CMS}. Therefore, these polycrystalline pseudo spin valves exhibit no significant AFM bilinear or 90° biquadratic coupling and the kink in fig. 58 (b) is the result of different H_c for top and bottom FM due to a respective Cr and Ag underlayer. Biquadratic exchange is also reported to be negligible for (001)-epitaxial CMS/Ag/CMS PSV[162] with $t_s = 5$ nm deposited at RT. Oscillating AFM

[162] H. S. Goripati et al., *J. Appl. Physics* **110**, 12, 123914 (2011)

coupling is relevant for (001)-epitaxial CFMS/Ag/CFMS [163] samples for $0.5 < t_s < 5$ nm. Here it is most likely suppressed due to uncorrelated roughness.

[163] T. M. Nakatani et al., *Appl. Phys. Lett.* **99**, 18, 182505 (2011)

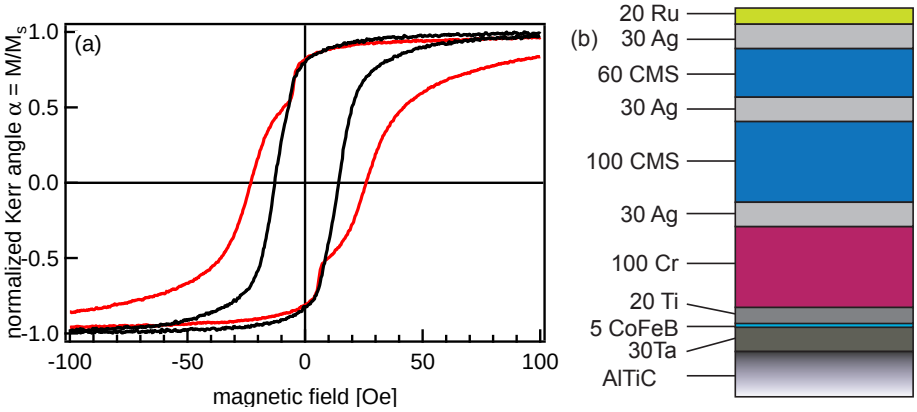

Figure 59: (a): MOKE curves of the pseudo spin valve stack depicted in fig. 57 with Ag spacer and $t_s = 30$ Å (red) and the one shown in (b) (black). No kink is visible for the stack with Cr/Ag underlayer combination.

Lastly, to test for possible FM bilinear coupling, the same CPP-GMR stack but with AFM-pinning and $t_s^{Ag} = 30$ Å is deposited on the same seed/buffer as the previous pseudo spin valve. The stack is depicted in fig. 60 (c). High-field MOKE data is shown in fig. 60 (a) and (b). With

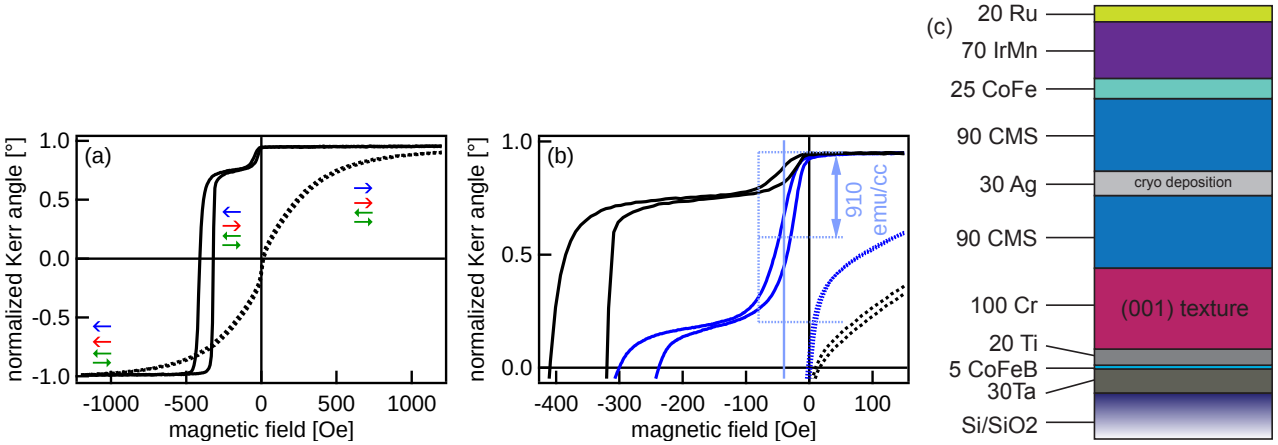

Figure 60: (a): zoom of the high-field MOKE data of the (001)-textured and pinned CPP-GMR stack with CMS as RL and FL. The orientation of the AFM, RL and FL is colored in green, red and blue, respectively. The switching of the FL is magnified in (b) together with the BHLooper data (blue). The FL-MOKE signal is reduced due to depth sensibility. The strength of the bilinear coupling can be quantified by the shift of the FL hysteresis, which is about -40 Oe.

this kind of stack any contribution of J_1 will shift the FL switching curve (also called *minor loop*) away from the zero field position, i.e. it will move it closer to ($J_1 > 0$) or away ($J_1 < 0$) from the AFM/RL switching loop, respectively. J_2 will stretch/distort the hysteresis along the x-direction due to the scissor-like switching of FL versus RL, but is hard to estimate with this particular stack. The FL switching is shifted by 40 Oe, smaller than for reported 3 nm Ag spacer sandwiched between CoFe electrodes[164]. For comparison, the same FL/NM/RL trilayer is grown on the record-Q_{011}^{T} Ta/Ru seed combination. The Ag spacer grows (111) here and the thickness of CMS can be reduced to the critical

[164] J. C. Read et al., *J. Appl. Physics* **118**, 4, 043907 (2015)

thickness $t^{\mathrm{CMS}} = 60$ Å (obtained from fig. 42 (a); just before considerable loss of M_s). The full stack is shown in fig. 61 (c). Even though the

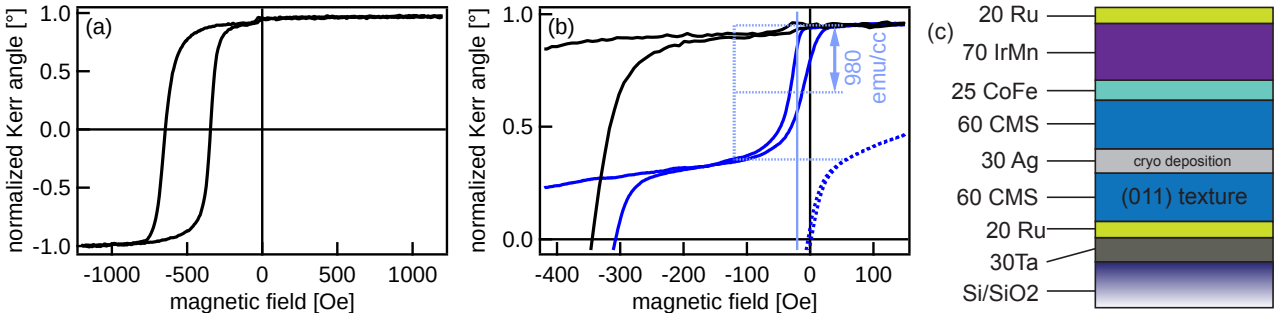

Figure 61: (a): zoom of the high-field MOKE data of the (011)-textured and pinned CPP-GMR stack along the pinning direction. Stack is shown in (c) with CMS as RL and FL; (b): $H_d = -20$ Oe.

bottom CMS is thinner, J_1 is reduced comparably to the (001)-textured stack, hinting towards a improved FM/NM interface roughness. To demonstrate the importance of Ag cryo-deposition, the same stack as in fig. 61 (c) is grown with Ag at RT. BHLooper data is shown in fig. 62, which shows, that RL and FL are strongly ferromagnetically coupled, preventing independent switching.

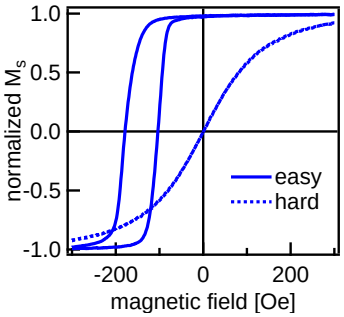

Figure 62: BHLooper of the same stack as in fig. 61 (c), but with the Ag spacer deposited at RT. The agglomeration of Ag on CMS is strong enough so that roughness induced FM coupling prevents independent switching

Roughness estimation for orange-peel coupling

AFM images of the lower part of the stack including FM_b, but without Ag are recorded to estimate the morphological contribution of FM_b to the FM_b/NM interface roughness. The cross section of the (001)-textured stack from fig. 60 (but without Ag and successive layers) is shown in fig. 63. It is noticeable that the main height fluctuations are in the dimension of $\lambda \sim 100$ Å, see eq. 52. Thus contributions with shorter wavelengths are filtered out with the help of a 1D Fourier transformation and it is found that filtering out $\lambda < 70$ Å captures the essential morphological fluctuations that most likely contribute to the orange-peel effect due to dipole formation, see fig. 63 (a). Local minima and maxima are found by differentiating the filtered height profile and looking for the zero-crossings, see fig. 63 (b). Then, the heights and distances of about 250 adjacent local extrema are extracted and respective histograms fitted to a log-normal distribution $P(x)$

$$P(x) = \frac{1}{\sigma\sqrt{2\pi}} \exp \frac{-(\ln x - x_0)^2}{2\sigma^2} \tag{53}$$

The same approach is conducted for the (011)-textured film, see fig. 63 (c). Fig. 64 shows the histograms and fits for the two different texture type stacks. By definition the fitted most abundant peak-to-valley height is equal to twice the amplitude A. And twice the value of the most prominent peak-to-valley distance is equal to the dominating sinusoidal roughness wavelength λ. However, the fit for the average peak-to-valley height is poor and fails to extract a useful A for the (011)-textured film, see fig. 64 (a). Therefore R_a from AFM measurements will be used

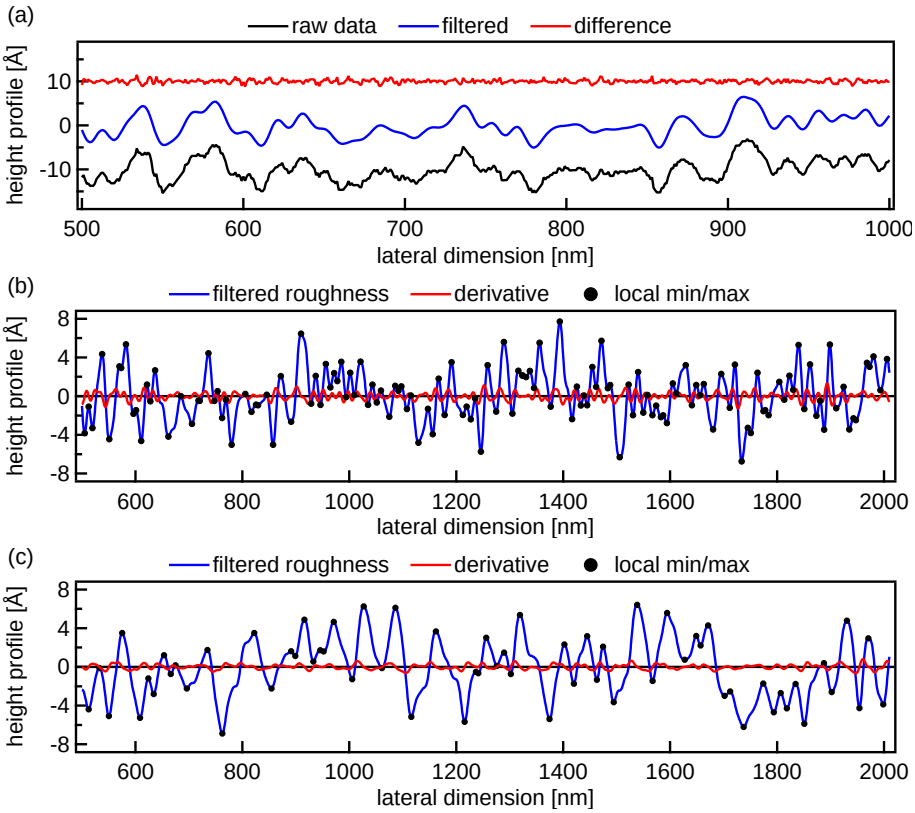

Figure 63: (a): excerpt of a 2.5 µm long roughness profile of the FM_b terminated (001)-textured stack. The data is filtered via 1D FFT with a cut-off frequency of 0.15 nm^{-1}; (b): same roughness profile with its derivative added in order to find peaks and valleys; (c): excerpt of a 2.5 µm long roughness profile of the FM_b terminated (011)-textured stack with its derivative and marked peaks/valleys.

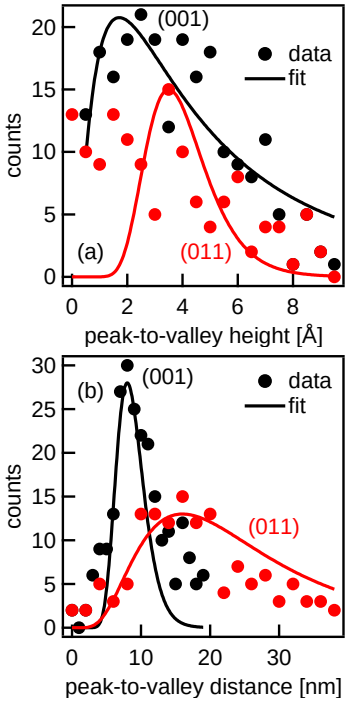

Figure 64: histograms of (a) peak-to-valley heights and (b) peak-to-valley distances extracted from an AFM profile of the sample in fig. 63 (b) (black) and 63 (c) (red). The profile scan length is 2.5 µm.

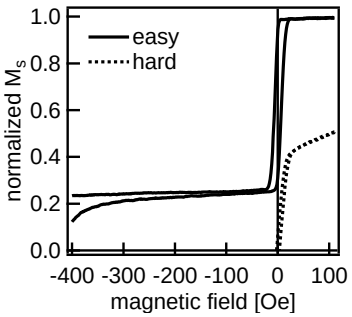

Figure 65: same stack as in fig. 61, but with CFMS as RL and FL. $J_1 = 0$, since the minor loop shows no offset. The major loop is not shown here.

instead of A to calculate the dipolar field H_d. The obtained values are summarized in tab. 6, where also roughness R_a is added. H_d for both

Table 6: extracted roughness parameters (via AFM) of the FM_b/NM combinations used in the CPP-GMR stacks. H_d is the orange-peel coupling field calculated via eq. 52 as a function of λ and A, explanation see text.

stack	λ [nm]	A [Å]	R_a [Å]	H_d [Oe]
(001)	16	1.7	2.1	0.37
(011)	32	n.a.	2.1	0.68

texture types is considerably smaller than the measured hysteresis-offset seen in figs. 60 (b) and 61 (b). Furthermore, the extracted λ for the (011) stack is twice as large as compared to the (001) stack, which theoretically should lead to $H_d^{(011)} > H_d^{(001)}$, taking the similar amplitudes of both surface profiles into account, see fig. 56 (a), but the opposite trend is obtained experimentally in the films, compare fig. 60 (b) and 61 (b). And comparatively, the roughness of FM_b that perpetuates through the spacer leading to a correlated roughness profile cannot be the lone origin for the magnitude of the observed minor loop shift caused by FM coupling in the samples. Pin-holes in the Ag spacer might add to the magnitude.

The same stack as in fig. 60 (c) is grown with CFMS as RL and FL. All the deposition parameters are the same. Interestingly, the bilinear coupling is zero, see fig. 65. Because CFMS and CMS single films have an almost indistinguishable roughness profile for both texture types, differences in Ag growth on each Heusler are likely the reason for the observed properties, specifically the formation of pin-holes which couple FM_b with FM_t with $J_1 > 0$. Both Ag cryo-deposition and addition of Y (Y=Mg, Ti, Cu, Al) for $Ag_{1-x}Y_x$ is proposed as spacer materials for the fabrication of CPP-GMR devices in order to prevent pinhole formation.

Tunable damping α for $Co_{2-x}Ir_xMnSi$

Tunability of the Gilbert damping parameter α[165] in applied materials for spintronic applications is a crucial step towards controlling switching behavior and thus the efficiency of a CPP-GMR, MRAM or STT-RAM device. Fast relaxation of the magnetization into equilibrium without *ringing*, i.e. an excessive precession of the magnetization vector[166], is needed. Furthermore, the damping contribution during magnetization precession points in the opposite direction of STT, where a current through the layers disturbs the magnetization within the FM by exerting a torque on it. This is desired for STT-switching applications but reduces CPP-GMR device performance. Thus tunable damping will help to balance the effect of STT. There have been different approaches, i.e. modifying composition by rare-earth doping[167], which however leads to increasing film amorphization. Other efforts include change of CMS composition by adding Co in $Co_{2(1+x)}Mn_{1-x}Si_{1-x}$[168] which leads to a reduction of half-metallicity[169] and increase of intrinsic damping parameter α by introducing Co-antisites[170]. However, it has not been attempted to tune the intrinsic damping while at the same time maintaining HM properties. The controlled tuning of intrinsic damping of the HM Heusler compound CMS by means of substituting Co with the isoelectronic element Ir leads to $Co_{2-x}Ir_xMnSi$ (CIMS) up to $x = 1.0$ (bulk) and 0.54 (thin films). Theoretical calculations[171] are combined with bulk ingot preparation and sputtered thin films of this novel quaternary Heusler compound. Damping is found to be linearly increasing with substituent concentration whereas maintaining M_s in bulk and half-metallicity in theory[172].

Bulk

Table 7: lattice constant a, magnetization M and Curie temperature of the bulk samples.

x	a [Å]	M [μ_B/f.u.] @1.8 K/298 K	T_C [K]
0.00	5.660	5.0/5.0	1008
0.05	5.672	4.9/4.7	987
0.10	5.681	4.7/4.6	983
0.20	5.704	5.2/5.0	943
0.25	5.711	5.0/4.7	923
0.50	5.721	n.a.	n.a.

[165] T. L. Gilbert, *Phys. Rev.* **100** (1955), p. 1243, T. L. Gilbert, *IEEE Trans. Magn.* **40**, 6 (2004), pp. 3443–3449

[166] R. H. Koch et al., *Phys. Rev. Lett.* **81**, 20 (1998), pp. 4512–4515

[167] W. Bailey et al., *IEEE Trans. Magn.* **37**, 4 (2001), p. 1749, S. Ingvarsson et al., *Appl. Phys. Lett.* **85**, 21 (2004), p. 4995, S. G. Reidy, L. Cheng, and W. E. Bailey, *Appl. Phys. Lett.* **82**, 8 (2003), p. 1254

[168] Y. Sakuraba et al., *Appl. Phys. Lett.* **96**, 9 (2010), p. 092511

[169] R. A. de Groot et al., *Phys. Rev. Lett.* **50** (25 1983), pp. 2024–2027, J. Kübler, A. R. Williams, and C. B. Sommers, *Phys. Rev. B* **28**, 4 (1983), pp. 1745–1755

[170] F. Yang, X. Kong, and X. Chen, *J. Phys. D: Appl. Phys.* **46**, 19 (2013), p. 195001

[171] A. Köhler et al., *Phys. Rev. B* **93** (9 2016), p. 094410

[172] In this work the experimental part of the corresponding publication will be presented. The theoretical calculations of this Heusler compound were performed by co-author Lukas Wollmann and can be read in the published scientific report.

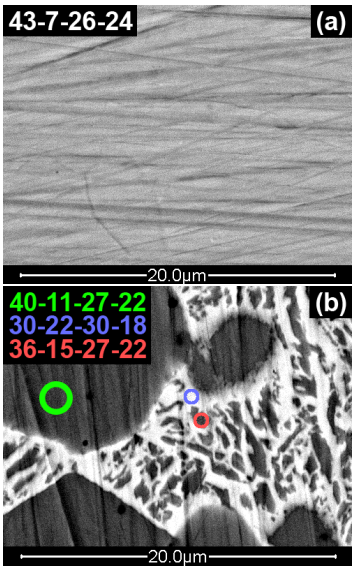

Figure 66: SEM phase contrast images, numbers are at% composition Co-Ir-Mn-Si: (a) $x = 0.25$, single phase only; (b): $x = 0.5$, phase separation (green and blue) and intermediate phase (red).

Table 7 shows M_s, T_C and lattice constants for the bulk samples. There are slight variations in M_s which are not attributed to x but most likely originate from arc melting parameter adjustments due to increasing Ir content. T_C decreases about 100 K and the lattice parameter increases by 1% when going from Co_2MnSi towards $Co_{1.75}Ir_{0.25}MnSi$. Fig. 67 shows the corresponding XRD $2\theta/\omega$-scans. The degree of

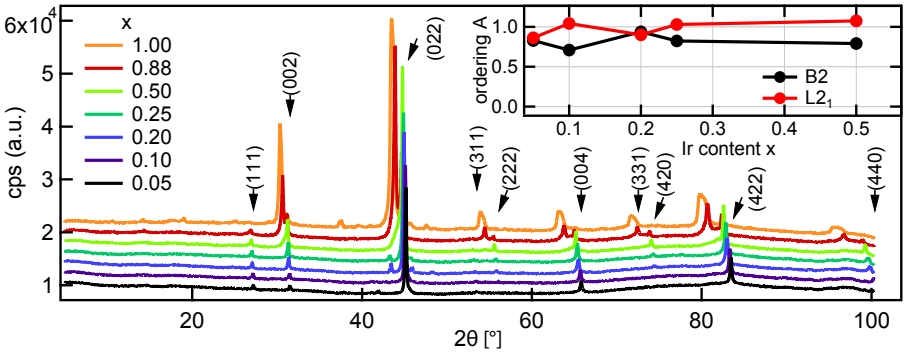

Figure 67: XRD $2\theta/\omega$-scans for polycrystalline bulk samples for increasing substitution of Co by Ir; inset: ordering after eq. 54

$B2$ and $L2_1$ ordering is evaluated by order parameter $A_{B2/L2_1}$ and is shown in the inset of fig. 67:

$$A_{B2} = \frac{I(002)/I(004)}{I_0(002)/I_0(004)},\ A_{L2_1} = \frac{I(111)/I(022)}{I_0(111)/I_0(022)} \qquad (54)$$

where I and I_0 are the corresponding experimental and theoretical integrated XRD peak intensities, respectively.

For x $\geq$ 0.5, a secondary Ir-rich phase develops which cannot be cured by subsequent melting and annealing for several days (fig. 66). The curves in fig. 67 confirm this phase separation with the appearance of broad peak-shoulders and peak splitting. A zoom into the (002) and (004) peak region is given in fig. 68. The peak splitting for x $\geq$ 0.5 can be interpreted as the evolution of an additional tetragonal phase. This would split the $L2_1$ (002) peak into $D0_{22}$ (002), (110) and $L2_1$ (004) into $D0_{22}$ (004), (220), respectively. Interestingly, with higher x the peak splits increasingly into three individual peaks. This means that aside from cubic $L2_1$ two tetragonal phases are present: the lattice constants are either $c < \sqrt{2}a$ or $c > \sqrt{2}a$. A simulation of these two cases is exemplified in fig. 69. A comparison with the measured peak heights in fig. 68 hints that both $D0_{22}$ phases are present in addition to the decreased cubic phase. The phase with $c < \sqrt{2}a$ is more abundant than $c > \sqrt{2}a$ with increasing x.

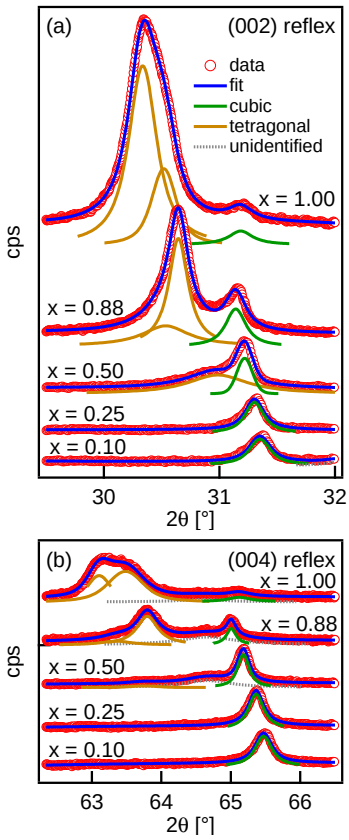

Figure 68: XRD $2\theta/\omega$ scans of the bulk samples around the cubic (a) (002) and (b) (004) reflex region. Two tetragonal peaks evolve for $x \geq 0.5$.

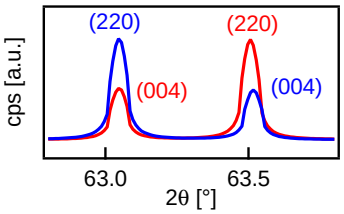

Figure 69: simulated XRD CIMS peak heights for the $D0_{22}$ phase with $a = 5.85/\sqrt{2}$Å, $c = 5.89$Å (red) and $a = 5.89/\sqrt{2}$Å, $c = 5.85$Å (blue).

Thin films

CIMS films with x = 0.23 and x = 0.41 have been co-sputtered on (001)-MgO-subs/20MgO and post-annealed at 400°C for 5 hours. The magnetization is zero and no (002) or (004) XRD reflexes are visible. The use of a buffer material and/or elevated deposition temperature is

necessary.
In order to enable technological applicability of the thin film stack no MgO as seed material is added, but rather the developed Ti/Cr combination is chosen to obtain the (001)-texture, which maintains a low $RA < 0.1\ \Omega\mu m^2$. The Ta/Ru seed combination is chosen for the (011)-textured samples. The typical surface roughness is $R_q = 2$ Å, even after annealing. The stacking is:

- (001)-texture: 30Ta/5CoFeB/20Ti/150Cr/**180CIMS**/20Ru
- (011)-texture: 20Ta/20Ru/**180CIMS**/20Ru

M_s is measured by BHLooper, whereas M_{eff} is obtained from the fitted IP FMR response. Fig. 70 shows magnetization curves for the two differently textures systems for varying x.

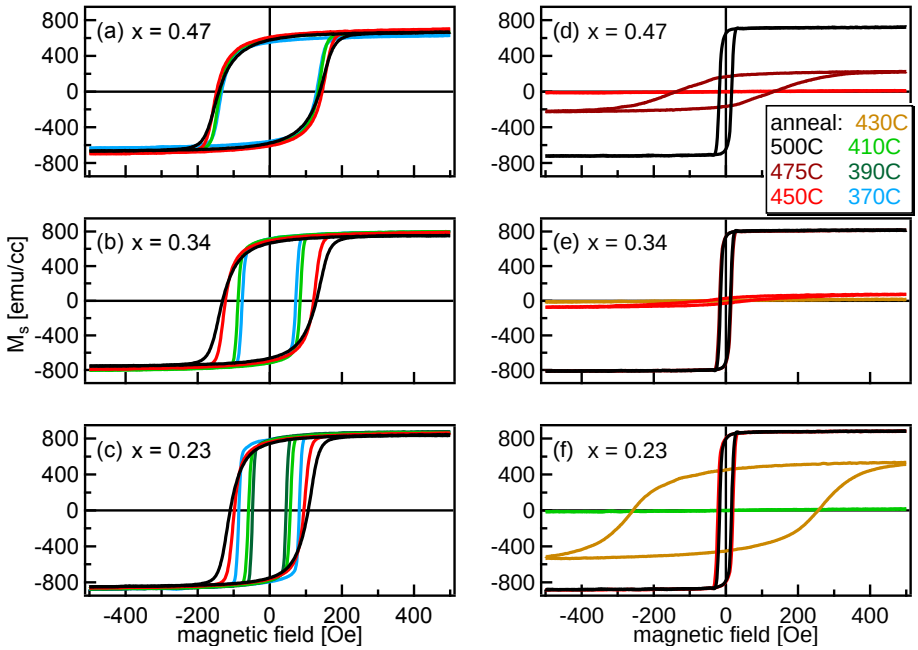

Figure 70: magnetization loops (BHLooper) for three compositions with increasing Ir content; (a)–(c): (001)-textured films with Ti/CoFeB/Cr seed/buffer combination; (d)–(f): (011)-textured films with Ta/Ru seed. A magnetically dead layer of $\tilde{t} = 8$ Å has been accounted for in (d)–(f). $\tilde{t}$ is assumed to be constant throughout the range of Ir content.

Ti/CoFeB/Cr seed/buffer, (001)-textured films

Instead of utilizing a Cr buffer on a single crystalline MgO substrate, a full 8″Si wafer is coated with a high Q_{001}^{T} high-RA seed/buffer combination, i.e. 20Ti/5CoFeB/20MgO/150Cr. Then a CIMS gradient is deposited and in-situ annealed at 370°C for 1h. The complete stack is shown in fig. 71. Additionally, a twin sample for compositional measurements via XRF is deposited, which is further compared to calculated Ir composition (as described on p. 31), see fig. 72 (a) and (b). The calculation of Ir composition shows very good agreement with the measured

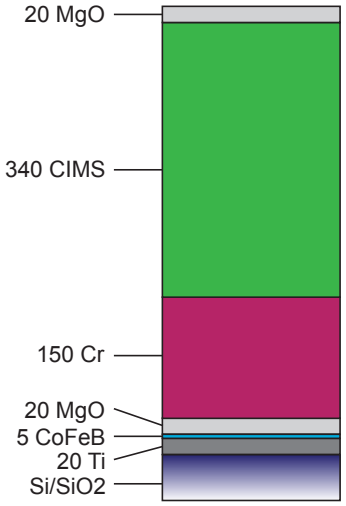

Figure 71: CIMS gradient stack on high Q_{001}^{T} seed/buffer system. The CIMS film has a thickness of 340 Å in the center of the wafer.

values and thus proves to be a valuable approach here, as it allows for the evaluation of points close to the edge of the wafer. The ordering

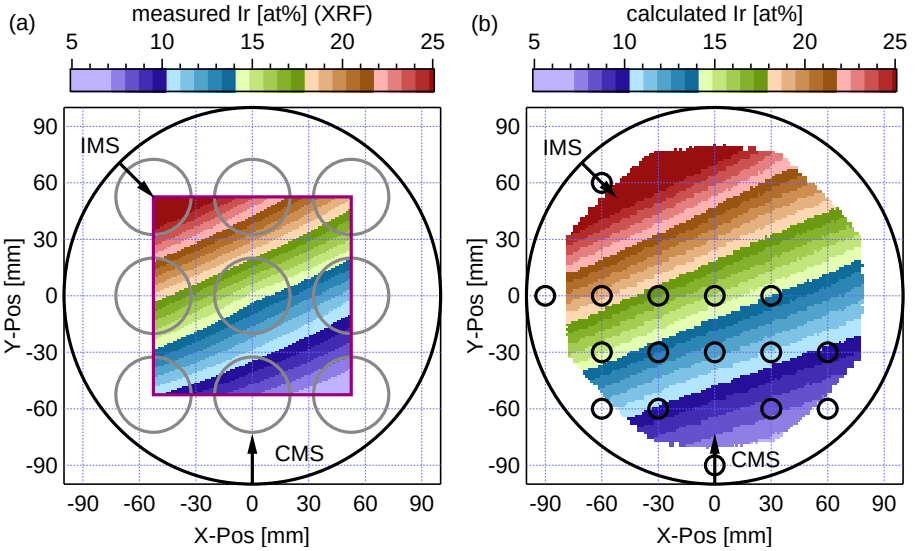

Figure 72: the measured composition on a wafer shown in (a) matches the calculated Ir concentration in (b). The gray circles in (a) illustrate the XRF spot size of 4 cm diameter (values in between are interpolated), whereas the smaller black circles in (a) indicate the locations that have been measured with XRD (1cm diameter spot size).

of the (001)-oriented CIMS thin films is compared to that of the bulk samples and theoretical expected values of XRD height ratios, see fig. 73. For the thin films, the wafer locations depicted in fig. 72 (b) provide the XRD data for varying x. Since M_s of CMS increases with higher ordering A2 $\mapsto$ B2 $\mapsto$ $L2_1$ and annealing temperature T_a[173] and only B2 or $L2_1$ order linearly increase I_{002}/I_{004}, A2 or inverse Heusler order can be excluded. This confirms B2/$L2_1$ crystallization of the thin film samples for the chosen seed/buffer type. For the damping investigations, CIMS films with selected x are deposited with substrate rotation onto the same Q_{001}^{T} buffer and (001) preferred orientation is again confirmed by XRD $2\theta/\omega$-scans in fig. 74, which show only the substrate and (002) and (004) Heusler peak (at least B2 order). Lattice constants obtained via XRD, M_s via BHLooper and M_{eff} with FMR are summarized in fig. 78 (a) and (b). There is a sensitive annealing dependence on all film properties, but only if they contain Ir. For high Ir content with $x > 0.48$, M_{eff} is sufficiently higher than M_s, hinting towards an increasingly negative $K_U^{\perp}$. For the lower Ir concentrations this effect is less pronounced. Furthermore for $T_a = 500°C$, M_s drops for all samples, which hints towards film degradation due to high annealing temperatures. An explanation for this would be Cr diffusion into the Heusler or disorder between Co/Ir and Mn sites that can lead to the deterioration of M_s of samples annealed at $T_a \geq 450°C$[174]. But here the sample with $x = 0.0$ shows no degradation, thus Cr diffusion can be excluded (future Ag insertion between Cr and Heusler could further prevent potential Cr diffusion). More likely, after a critical annealing temperature, crystallization of nanoclusters with fluctuating composition and magnetization takes place, just as observed for the bulk samples, see fig. 66. This *smears*

[173] T. Graf, C. Felser, and S. S. P. Parkin, *Progress in Solid State Chemistry* **39**, 1 (2011), pp. 1–50

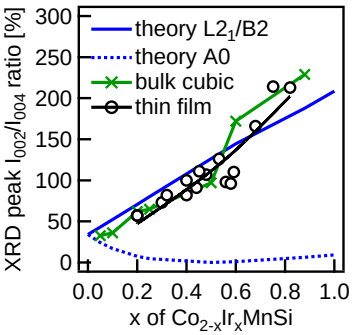

Figure 73: the XRD peak ratio I_{002}/I_{004} for CIMS thin film and bulk samples follows the theoretical trend for B2/$L2_1$ crystallization.

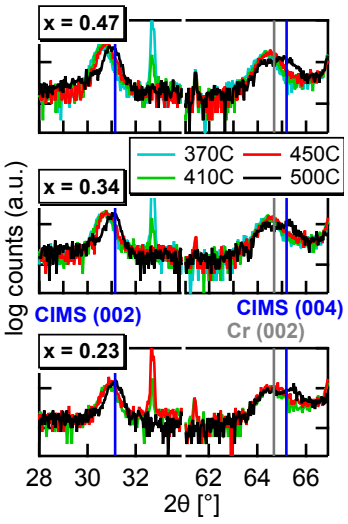

Figure 74: $2\theta/\omega$ XRD scans of the (001)-textured samples. After the 500° anneal the stress relaxes.

[174] M. P. Raphael et al., *Phys. Rev. B* **66** (10 2002), p. 104429

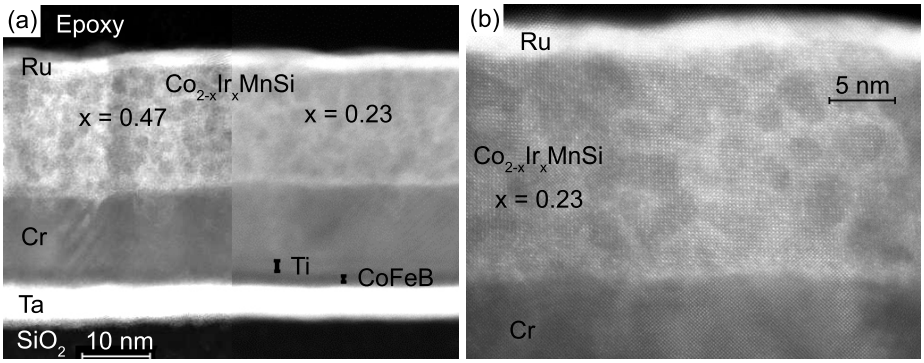

Figure 75: STEM images of Ti/CoFeB/Cr buffered (001)-textured samples; (a): for x= 0.23, difference of contrast within the CIMS layers can be attributed to the formation of clusters with differing Ir concentrations, which integrate into the lattice without defects or stacking faults. The (001)-texture is clearly visible; (b): same region as in (a) next to another composition. The image has been processed so that both luminosity histograms of the lower Ta/CoFeB/Ti/Cr-part of the stack match. An increasing clustering is apparent with increasing x.

out the resonance location and leads to a large frequency-independent ΔH_0 which is about 4 times larger than in the films with Ta/Ru seed, see fig. 78 (b). To prove this argument, *scanning transmission electron microscopy* (STEM) cross section images of two samples with x = 0.23 and x = 0.47 (T_a = 450°C for both) are recorded and are shown in fig. 75. Deviations in contrast are clearly visible within the CIMS layer, which relate to density fluctuations. Brighter regions contain more Ir. This has a peak broadening effect on ΔH_0 in the FMR spectra (not shown here). Magnetization measurement results and FMR data evaluation are shown in fig. 78. Another possible contribution to the large ΔH_0 could lie in the antiferromagnetic nature of Cr, where local pinning centers at step edges of the Cr/CIMS interface give rise to local anisotropies. Overall, the sensitive dependence of the results on the annealing conditions for this Cr-based seed/buffer system complicates the interpretation of the data for the Cr-buffered (001)-oriented stacks.

Ta/Ru seed, (022)-textured films:

Since randomly distributed atoms (A2 disorder) lead to poor M_s[175] and the fact that here M_s is not changing when $T_a > T_a^0$, one can associate T_a^0 with formation of a $B2$ phase which leads to a high magnetization curve with low coercivity, see fig. 70 (a)–(c). It is further known that $T_a > T_a^0$ eventually leads to $L2_1$ order[176], which has to be investigated via direct structural measurement techniques and will not be quantified within the scope of this report. However, for $T_a > T_a^0$, all measured film properties for any x are absolutely independent of T_a. This hints towards successful $B2/L2_1$ mixed crystallization in our case, since the magnetic properties, e.g. damping, are sensitively dependent on the structural ordering[177].

XRD $2\theta/\omega$-scans in fig. 76 show only the substrate and (022) Heusler peak. There is a saturating jump for the (022) reflex after annealing at specific minimal temperature $T_a^0(x)$ that increases with x, see fig. 76.

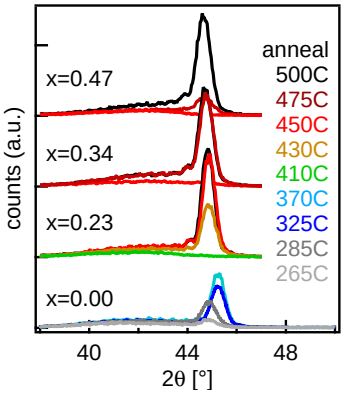

Figure 76: $2\theta/\omega$ XRD scans of the (011)-textured samples. The (0002) peak of the 20 Å Ru seed is broad and around 42.2°, adjacent to the (002) Heusler peak (substrate peak not shown).

[175] N. Tal et al., *J. Appl. Physics* **114**, 16 (2013), p. 163904

[176] S. Rodan et al., *Appl. Phys. Lett.* **102**, 24 (2013), p. 242404

[177] R. Yilgin et al., *Jap. J. Appl. Phys.* **46**, 9 (2007), pp. L205–L208

All annealing steps were 600 sec via RTA. Since there is no apparent XRD-peak degeneration with increasing x, amorphization can be excluded. In fact, the peak intensity is rising with x due to an increasing atomic form factor which proves the integration of Ir atoms into the Heusler lattice. The films are 2–3% strained in c-direction as compared to the bulk lattice parameters due to the smaller in-plane atomic distance in the (0002) Ru plane. Crystallite size obtained via the Scherrer formula[178] is increasing with temperature and equals film thickness at $T_a^0(x)$. (022) rocking curves (not shown here) gave FWHM $\simeq 4.5°$, negligibly depending on annealing temperature, which corresponds to a minimum lateral coherent scattering crystallite size of $\simeq 25$ Å, accompanied by broadening due to mosaicity. This indicates distinct columnar growth that is induced by the Ta/Ru seed layer.
All following results are from (022)-textured samples annealed at 500°C if not indicated otherwise.
Fig. 77 shows the IP FMR response and fitted data (OP FMR data not shown here). The resonance positions $f(H_{res})$ are fitted via eq. 25. It is

[178] J. I. Langford and A. J. C. Wilson, *J. Appl. Cryst.* **11**, 2 (Apr. 1978), pp. 102–113

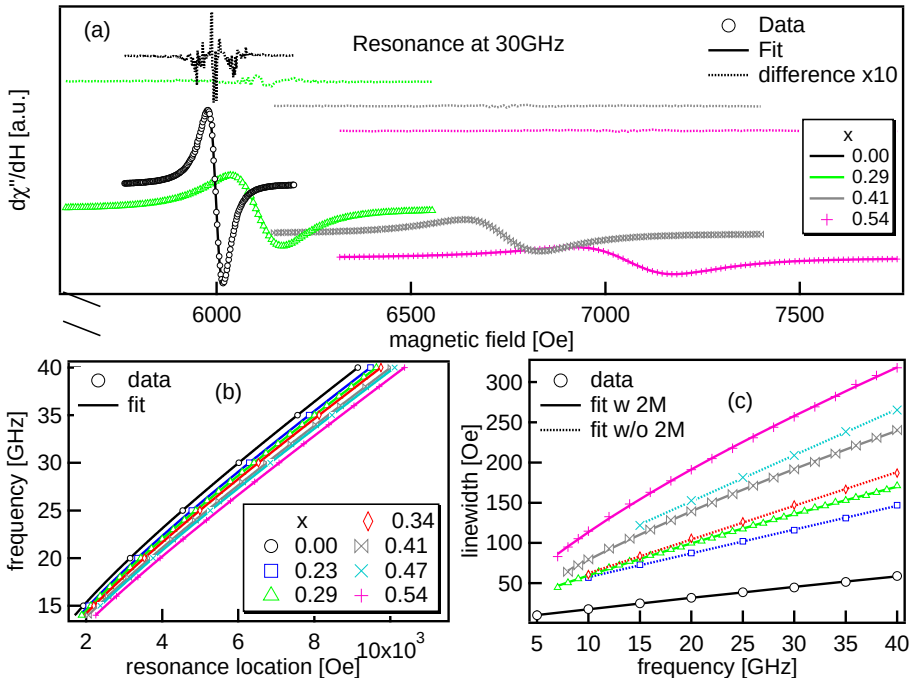

Figure 77: (a): IP FMR response, asymmetric Lorentzian fit and difference for selected Ir concentrations for samples annealed at 500°C. The curves are shown with an offset for better visibility; (b): (zoomed in) using results from a) and fitting it using the solution to the LLG-equation eq. 25; (c): Fit for α and Γ with eq. 33. For the samples with x = 0.23, 0.34 and 0.47 a linear fit without the 2M term was performed.

pointed out, that fitting IP FMR $f(H_{res})$ is very sensitive to the chosen range, which can lead to a comparably large uncertainty in $M_{eff}^{||}$[179]. This is accounted for by fitting within different ranges and including an error for $M_{eff}^{||}$. It is further found that the fit following eq. 39 for the OP case is less sensitive to the chosen range, leading to a smaller error in $M_{eff}^{\perp}$. Damping parameter α is evaluated following eq. 33 and 40, depending on the FMR configuration.

[179] J. M. Shaw et al., *J. Appl. Physics* **114**, 24 (2013), p. 3906

Lattice constant a, M_s, H_c $M_{eff,}^{\parallel/\perp}$, ΔH_0, $\alpha^{\parallel/\perp}$, $\alpha^{\parallel/\perp} \cdot M_s$ and Γ are shown in fig. 78 (e)–(h). There was a slight compositional difference of the resulting films from the two targets which inevitably induced an increasing Mn deficiency up to 5 at% (20 at% instead of 25 at% in the compound) for $x = 0.54$. This monotonically reduces M_s[180] since the Mn positions carry the main contributing magnetic moment. However, the measured reduction of M_s with x is about twice as strong as the estimation based on a simple removal of Mn from the octahedral positions predicts, as included in fig. 78 (f). Increasing anti-site disorder is therefore suspected which additionally reduces the magnetic moments of the neighboring atoms.

[180] G. Li et al., *Phys. Rev. B* **89** (1 2014), p. 014428

Since $\alpha = G/(\gamma M_s)$[181], with G being the Gilbert constant, we phenomenologically account for the Mn-depletion related loss of magnetization by evaluating $\alpha \cdot M_s$, that trends linearly with x. The proportionality of the experimental data for $\alpha \cdot M_s\,(x)$ is less drastic as $\alpha\,(x)$ and more comparable to the theoretical slope, but still about a factor 2 larger.

[181] J. Lindner et al., *Phys. Rev. B* **68** (6 Aug. 2003), p. 060102

For the IP case $\Delta H_{2M}\,(f)$, see eq. 34, can be difficult to extract for $\Delta H(f)$ data with small curvature, since the fit handles all linebroadening contributions independently. Therefore two types of fits for the IP linewidth data are presented: one that includes the expression for $\Delta H_{2M}\,(f)$, thus giving $\alpha^{\parallel}$, and one that omits it, where in the latter case the resulting *2M-uncorrected-*$\alpha^{\parallel}$ is effectively enhanced, see fig. 78 (g), (h). It is found that the inclusion of the $\Delta H_{2M}\,(f)$ term into the fit leads to a very good agreement of $\alpha^{\parallel}$ with $\alpha^{\perp}$, but only if there are data points in a wide enough frequency range[182], thus validating this approach even for less apparent curvatures in $\Delta H(f)$.

[182] D. L. Mills and R. Arias, *Physica B* **384**, 1-2 (2006), pp. 147–151

Tab. 8 summarizes thin film data obtained by XRD, BHLooper and FMR measurements. It is noted that $g^{\perp} \simeq g^{\parallel} \equiv g$ (difference in g is $< 2\%$). Note that the damping parameter $\alpha = 0.003$ of the CMS sample annealed at $T_a = 370°C$ is one magnitude smaller than for previously reported CMS polycrystalline samples, i.e. $\alpha = 0.025$[183] and even smaller than

[183] R. Yilgin et al., *J. Magn. Magn. Materials* **310**, 2 (2007), pp. 2322–2323

Table 8: lattice constant a, M_s, damping parameter $\alpha_{\parallel}$ and $\alpha_{\perp}$ from IP and OP FMR configuration (respectively) of the (011)-textured films, two-magnon scattering strength Γ obtained from the IP data and the averaged g-factor of the thin film samples at RT. The values for $\alpha^{\parallel}$ printed in *italic* are the results from a linear regression where the 2M term in eq. 25 was omitted, which clearly leads to an overestimation of the intrinsic damping by comparison with $\alpha^{\perp}$.

x	a [Å]	M [$\mu_B(f.u.)$]	$\alpha^{\parallel}$	$\alpha^{\perp}$	Γ [Oe]	g
0.00	5.668	4.9	0.0031	0.0030	8	2.034
0.23	5.719	4.7	*0.0073*	0.0064	n.a.	2.027
0.29	5.722	4.5	0.0071	0.0069	51	2.025
0.34	5.730	4.3	*0.0128*	0.0073	n.a.	2.033
0.41	5.738	4.1	0.0095	0.0097	100	2.025
0.47	5.740	3.9	*0.0142*	0.0109	n.a.	2.032
0.54	5.749	3.6	0.0121	0.0128	133	2.030

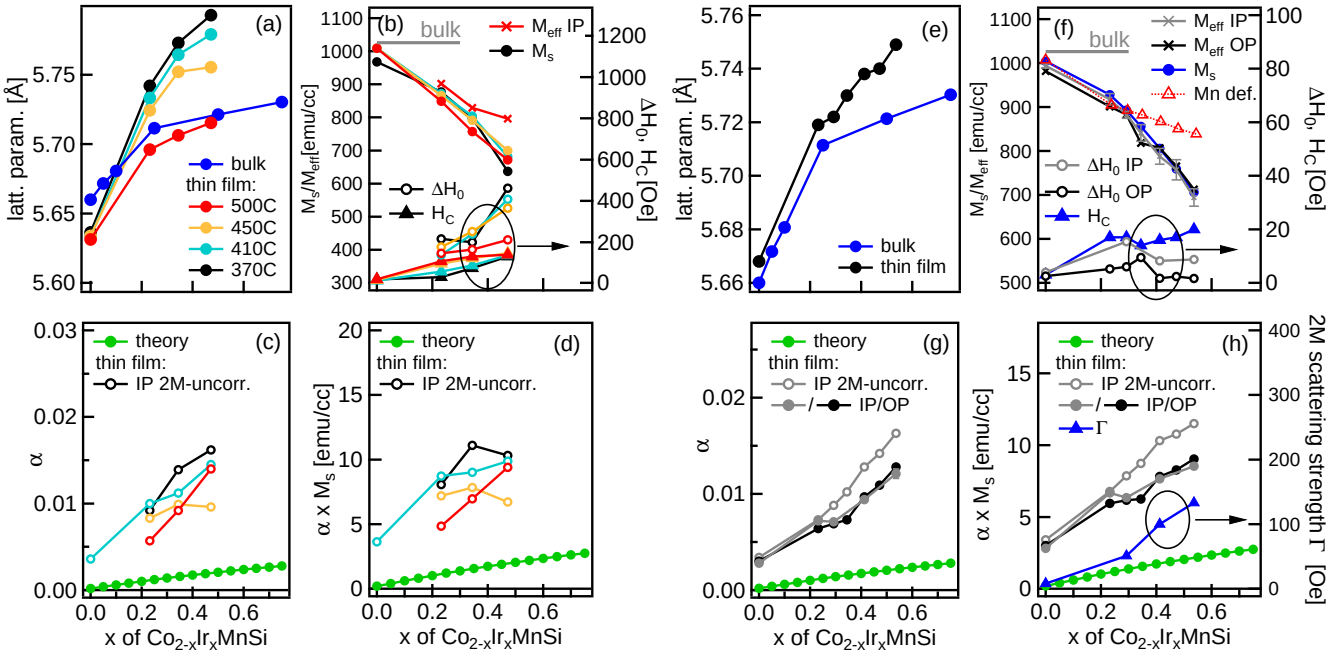

Figure 78: (a)–(d): measured and calculated data on the (001)-textured CIMS films on Cr buffer; (a): film/bulk lattice parameter obtained via XRD; (b): M_s and M_{eff} (IP FMR configuration), H_c and extrinsic contributions ΔH_0 (IP only); (c): intrinsic damping $\alpha^{\shortparallel}(x)$; (d): product of $\alpha^{\shortparallel}$ with corresponding M_s. Overall, the Cr buffered films show a strong temperature dependence; (e)-(f): the same values as for (a)-(d) but for the (011)-textured CIMS films on Ta/Ru seed and for both the IP and OP FMR configuration; (b): the red curve is the expected trend for a linearly increasing Mn depletion of 5 at% within this range.

for reported high quality epitaxial samples with B2[184] or $L2_1$ order where $\alpha = 0.0054$[185] - in fact it is the to date lowest reported α for any CMS film with a thickness below 20 nm. Therefore it hints towards a high spin polarization for this sample[186], which should be further investigated. The high value for $M_s = 1004$ emu/cc supports this argument. In any case, since B2 disorder maintains HM[187] this eases up the requirements from an application perspective.

No thickness dependent FMR measurements for CIMS will be reported here and one has to bear in mind that this thickness dependence can account for the offset of experiment and theory in fig. 78 (h). Just as presented for CMS and CFA in fig. 44, the extracted bulk damping parameter from the intercept with the ordinate will be smaller than α from corresponding thin films, possibly due to unaccounted 2M contributions. 2M-scattering is active when the magnon wave vector is in the range $k \approx 4\pi M_s t/D$[188], where t is thin film thickness and D exchange stiffness. By interpolating a bulk value for α with $t \to \infty$ it follows that $k \to \infty$. Since FMR probes $k \approx 0$ it is unaffected by 2M then.

For both the (001)-textured films on Cr buffer and (011)-textured films on Ta/Ru seed no tetragonal phase as in the bulk samples is observed.

[184] R. Yilgin et al., *Jap. J. Appl. Phys.* **46**, 9 (2007), pp. L205–L208

[185] T. Kubota et al., *Appl. Phys. Lett.* **94**, 12 (2009), p. 122504

[186] M. C. Hickey and J. S. Moodera, *Phys. Rev. Lett.* **102**, 13 (2009), p. 137601

[187] S. Picozzi, A. Continenza, and A. J. Freeman, *Phys. Rev. B* **69**, 9 (2004), p. 094423

[188] D. L. Mills and R. Arias, *Physica B* **384**, 1-2 (2006), pp. 147–151

TMR

Introduction

The main component of many spintronic devices is the MTJ, where an insulating barrier[189] separates two FM layers. The resistance perpendicular to the stack depends on the relative orientation of the magnetic moments and in general the *antiparallel* (AP) state results in a higher resistance than the *parallel* (P) orientation, i.e. $R_{AP} > R_P$. This defines the TMR:

$$\mathrm{TMR} = (R_{AP} - R_P)/R_P. \tag{55}$$

At small voltages the resistance is related to spin polarization of the conduction electrons and thus to the spin dependent *density of states* (DOS) at the Fermi level (E_F) of the FM layers, allowing to rewrite the TMR into the form[190]

$$\mathrm{TMR} = \frac{2P_b P_t}{1 - P_b P_t} \tag{56}$$

with the spin polarizations P_b and P_t of the two FM layers. An unwanted mechanism that typically adds to the conductivity of the antiparallel state and thus reduction of TMR is inelastic tunneling caused by thermal magnon excitation, which is the consequence of a non-ideal half-metal with small minority-spin gap and/or interface states. Furthermore, if the distance of E_F from a valence band is less than the level of thermal fluctuation $k_B T_{RT} = 25.7$ meV, spin polarization drastically decreases with temperature.

Typically, TMR thin film samples are patterned into µm-sized junctions via photolithography and ion beam etching. Via multiple other fabrication steps, which will not be discussed in detail here, the junction can be implemented into a HDD read head, which is sketched in fig. 79. A *hard bias* (HB) orients the FL so that it is operating around 90° relative to the RL. This guarantees a linear response but reduces the effective magnetoresistance that can be utilized.

RA is widely used as a normalized measure of junction resistance, since with $R = \rho \cdot t/A$ it is independent of the junction size. RA of MTJs typically ranges from $0.5\,\Omega\mu m^2$–$1\,M\Omega\mu m^2$, depending on the barrier height. MRAM typically exhibits 4–$1000\,\Omega\mu m^2$, whereas modern HDD read heads have $< 1\,\Omega\mu m^2$. Low resistance metal based CPP-GMR type sensors showcase $RA \sim 50\,m\Omega\mu m^2$ and therefore have a considerably

[189] J. S. Moodera et al., *Phys. Rev. Lett.* **74** (16 Apr. 1995), pp. 3273–3276

[190] M. Julliere, *Phys. Lett. A* **54**, 3 (1975), pp. 225–226

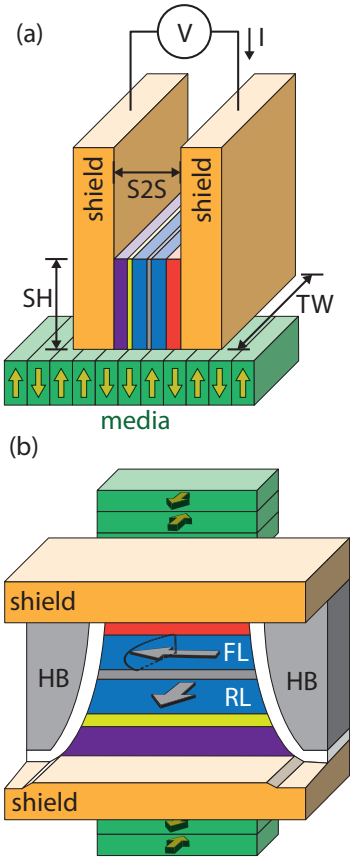

Figure 79: (a): typical HDD read head with perpendicularly magnetized media. Indicated are shield-to-shield distance (S2S), sensor height (SH), track width (TW) and media (green). Hard bias is not shown here; (b): top view with hard bias (HB), free layer (FL) and reference layer (RL).

smaller measurable signal $\Delta RA = RA_{AP} - RA_P$, as compared to MTJs. Together with the requirements of a uniform current through the CPP-GMR junction the area needs to be $\approx$100x100 nm^2, which complicates the route of measuring CPP-GMR compared to TMR, which will be elucidated later.

A typical TMR stack is shown in fig. 80. First, a seed/buffer combination is sputtered onto the plated NiFe shield. It generates a preferred orientation and lays the foundation for the (111)-texture of the $70Ir_{20}Mn_{80}$. The first $20Co_{90}Fe_{10}$ layer is pinned via direct exchange coupling and is termed P1. 4Ru serve as a metallic spacer for IEC of P1 with the second part of the pinned layer, also called P2, which is a CoFe-based combination tri-layer with partial Boron addition, typically $Co_{40}Fe_{40}B_{20}$ between $Co_{90}Fe_{10}$ or a similar composition. Boron is included because of its amorphous growth during deposition[191]. This increases the crystalline quality of the MgO barrier during the post-annealing after deposition (this effect was also relevant for the seed layer development section on p. 39). The AFM/P1/Ru/P2 design is crudely speaking a *synthetic antiferromagnet* (SAF) and the design is thus termed *SAF-pinning*. Its advantages over a single AFM/P design is a reduction in magnetic stray fields and a considerably stronger *exchange bias* H_{ex}. The MgO barrier follows, which can be either RF-sputtered or created by natural oxidation, whereas the latter is advantageous because of reduced unwanted oxidation of P2[192]. Thereafter follows the FL, which is finalized with dual layer of CoFeB and NiFe. This combination has shown to reduce magnetostriction which would be detrimental to the TMR output and device performance[193]. Lastly, the stack is capped with a specifically engineered CIPT-cap that adjusts the top layer (all of which is deposited after the barrier) sheet resistance to about 1 Ω/□, see oncoming section.

[191] H. Kurt et al., *J. Appl. Physics* **107**, 8 (2010)

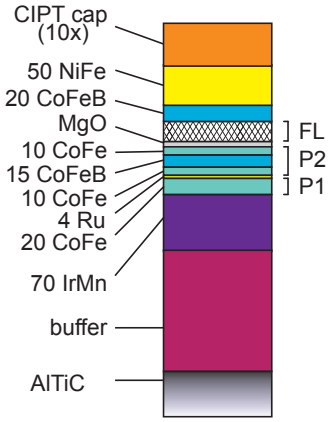

Figure 80: TMR stack used to implement CMS and CFA as FL. Numbers are in Å.

[192] A. T. Hindmarch et al., *Appl. Phys. Lett.* **97**, 25, 252502 (2010)

[193] K. Tsunekawa et al., *IEEE Transactions on Magnetics* **42**, 2 (Feb. 2006), pp. 103–107

[194] D. C. Worledge and P. L. Trouilloud, *Appl. Phys. Lett.* **83**, 1 (2003), pp. 84–86

[195] Capres.com

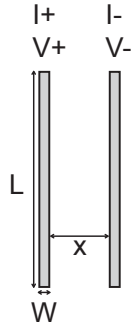

Figure 81: simplified two-contact CIPT probe head with indicated dimensions and labeled terminals.

Theory of CIPT

The comparably high RA of MTJs allows for a measurement technique that makes junction patterning redundant: *current-in-plane tunneling*[194] (CIPT) uses a four point probe to measure TMR and RA on an unpatterned wafer by placing the probes at appropriate spacings that range from 3-59 µm ($RA < 1\,\Omega\mu m^2$) to 1.5-8.3 µm ($RA > 1\,k\Omega\mu m^2$)[195].

To illustrate the idea of CIPT, consider two contacts of a two point probe having width W, length L and separation x, see fig. 81. Given that $L \gg x \gg W$ the wafer can be modeled by four resistors: two horizontal ones along the two magnetic layers and two vertical ones that include mainly the insulating barrier. The top and bottom layer have the resistance xR_t/L and xR_b/L, with sheet resistance R_t and R_b, respectively. The vertical resistors each have area $xL/2$ and therefore resistance $2RA/xL$. Solving the resistor network for the total

resistance gives:

$$R(x) = \frac{x}{L}\frac{R_t R_b}{R_t + R_b}\left(1 + 4\frac{R_t}{R_b}\frac{1}{4 + x^2/\lambda^2}\right) \tag{57}$$

where $\lambda = \sqrt{RA/(R_t + R_b)}$ which constitutes an intermediate length scale at which some of the current flows through the barrier while the vertical resistance is a substantial fraction of the total resistance. This becomes apparent when evaluating eq. 57 for $x \to 0$ or $x \to \infty$, where in the first case the current flows only within the top layer ($MR_{cip} = 0$) and in the second case it is distributed following a parallel configuration of the top and bottom layer resistance ($MR_{cip} = 0$ as well, since the barrier resistance is negligible compared to the horizontal contributions). The resistance is now measured as a function of probe tip spacing. $MR_{cip} = (R_{AP} - R_P)/R_P$ is then obtained by subtracting the data from a parallel magnetization configuration fitted to $R(x)$ from the fit to the antiparallel case and using $\lambda_{AP} = \sqrt{RA_{AP}/(R_t + R_b)}$ and $\lambda_P = \sqrt{RA_P/(R_t + R_b)}$ for the respective case.
Eq. 57 is a simplified model. The exact analytical solution that can be extended to four linearly aligned probes (to seperately measure voltage while driving current) is obtained by starting from differential equations that address current conservation and applying boundary conditions for currents and electric fields. For this it is furthermore assumed that $R_t t_t^2 \ll RA$ and $R_b t_b^2 \ll RA$, so that vertical voltage drops within the top and bottom layers can be ignored. This leads to[196]:

$$R = \frac{R_t R_b}{R_t + R_b}\frac{1}{2\pi} \cdot \left[\frac{R_t}{R_b}\left(K_0\left(\frac{a}{\lambda}\right) + K_0\left(\frac{d}{\lambda}\right) - K_0\left(\frac{b}{\lambda}\right) - K_0\left(\frac{c}{\lambda}\right)\right) + ln\left(\frac{bc}{ad}\right)\right], \tag{58}$$

where the distances a, b, c, and d are sketched in fig. 82 and K_0 being the modified Bessel function of the second kind of order zero. The data is recorded for low field (-400 Oe $\to R_{AP}$) and high field (+400 Oe $\to R_P$). For fitting the data to eq. 58, $R_{P/AP}$ is treated as a function of three independent variables, i.e. R_t, R_b and $RA_{P/AP}$. The probe pitches a, b, c, and d are given parameters for each point. It is important to notice that low top layer resistance will always partly short the barrier and thus effectively reduce MR_{cip}, depending on its ratio to the bottom layer resistance. Therefore a high ratio of $R_t/R_b = 10$ is chosen by depositing an appropriate CIPT-capping layer. An exemplary CIPT scan of a full TMR stack with TMR = 51% is shown in fig. 83.

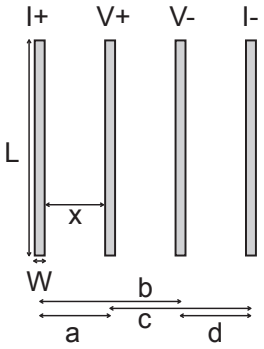

Figure 82: sketch of the dimensions of the CIPT four-contact probe head.

[196] D. C. Worledge and P. L. Trouilloud, *Appl. Phys. Lett.* **83**, 1 (2003), pp. 84–86

Results

The introduction of a Heusler as FL to the TMR stack has a promising starting point, since the deposition will be onto the MgO barrier. This

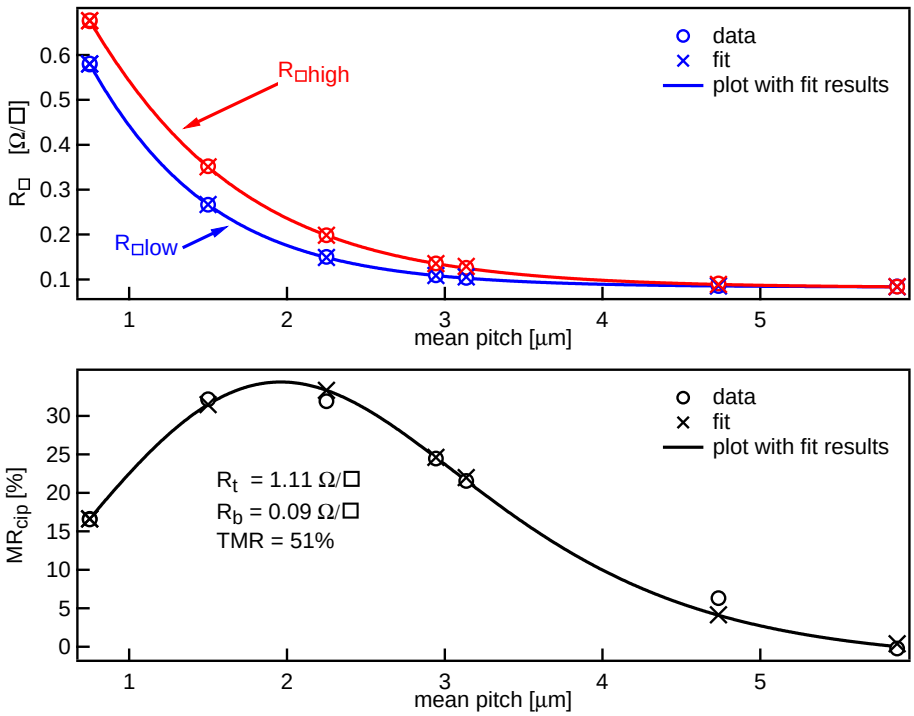

Figure 83: CFA used as FL in TMR stack (see next section) is measured via the CIPT method and evaluated following eq. 58. The mean pitch is determined from the parameters a, b, c and d which are the tip spacings of the CIPT probe. The line is a plot of eq. 58 using the fit results for R_t, R_b and $RA_{P/AP}$ (and MR_{cip}).

renders nucleation conditions similar to growing it onto the high-RA seed/buffer system which promoted (001)-texture. Using it as RL in the P2 however not only demands (001)-texture, but also requires optimized growth conditions of (001)-MgO on this RL. The utilization of the investigated (001)-seed/buffer layer combinations as presented earlier is however not possible, since the bottom-pin material $Ir_{20}Mn_{80}$ demands for a specificly designed seed layer in order to generate large exchange coupling. Therefore CMS and CFA are only employed as FL in the TMR stack depicted in fig. 80 and the utilization as RL will not be investigated here.

CMS FL for TMR

CMS has a higher B2 ordering temperature than CFA[197] and it is expected to provide higher TMR with increasing annealing temperature. Nine stacks with the stacking as in fig. 80 with CMS as FL are prepared. All samples are ex-situ postannealed at 285°C for 5 hours under 10 kOe magnetic field to promote crystallization and align the pinning. The nine samples are divided in three groups: A, B and C. Each group systematically investigates a different correlation with three samples: group **A** has three varying CMS thicknesses and a 2 Å CoFe termination at the MgO interface on the FL side. This serves two investigative purposes: CoFe-termination of CMS-based MTJs is reported to destroy the interfacial SP. The effect of surface termination is the same for CMS[198] and CFMS[199] and only Mn-Mn termination preserves high spin polar-

[197] D. Ebke, link, PhD thesis, 2010

[198] S. J. Hashemifar, P. Kratzer, and M. Scheffler, *Phys. Rev. Lett.* **94** (9 2005), p. 096402

[199] Y. Feng et al., *Appl. Surf. Sci.* **346** (2015), pp. 1–10

ization. Since no pure Mn target is available, the reverse approach is chosen here to see if a change of interface composition has an effect on the TMR at all. Secondly, by gradually adding CMS to the FL, a critical thickness can be evaluated and the impact of interface contribution can be separated. All three stacks of group A are in-situ RTA treated at 370°C for 10 seconds before the pinning anneal, as it is found to generate sufficient B2 order.
Group **B** tests the influence of annealing for the optimal CMS thickness established from group A, i.e. 6 Å. All three stacks of group B are in-situ RTA treated at different temperatures for 10 seconds.
Group **C** employs Co-Co-termination to investigate another possible decrease of SP of CMS[200]. The intermediate CMS thickness of group A is used and the previously established optimal annealing condition for CMS is tested. The group details are summarized in tab. 9.
Interestingly, increasing CMS thickness in group A decreases TMR and

Table 9: sample groups with different FL designs. The RTA treatment was done in-situ for 10 seconds after the deposition of the FL.

group	sample	FL	RTA [°C]
A	1	2CoFe/6CMS	370
	2	2CoFe/12CMS	370
	3	2CoFe/20CMS	370
B	1	6CMS	-
	2	6CMS	325
	3	6CMS	370
C	1	2Co/12CMS	-
	2	2Co/12CMS	325
	3	2Co/12CMS	370

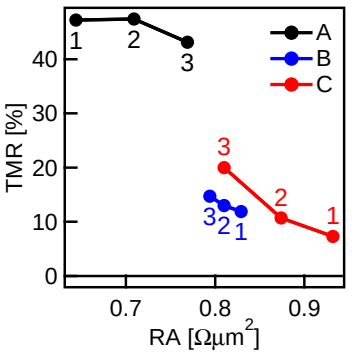

Figure 84: nine TMR stacks utilizing CMS as FL, details see tab. 9.

[200] S. J. Hashemifar, P. Kratzer, and M. Scheffler, *Phys. Rev. Lett.* **94** (9 2005), p. 096402

the highest value is obtained for 6 Å CMS, terminated with 2 Å CoFe at the interface with MgO. Without CoFe (sample 3 of group B), TMR drops to 15% with a slight RA increase for 6 Å CMS and there only a minor improvement on the TMR is observed with implementing the additional 10 second in-situ RTA step (group B). In-situ RTA has the highest impact on the Co-terminated 12 Å CMS.

CFA FL for TMR

Since CFA is DC-cosputtered from three elemental targets, it gives the opportunity to sputter a compositional gradient across the wafer, see fig. 85 (a)–(c). The target arrangement is optimal for minimizing an unavoidable thickness gradient of $\approx \pm 30\%$ (relativ to the center point), see fig. 85 (d). Before deposition of the MTJ stacks, a 150 Å CFA gradient single film is deposited onto Si/SiO_2 with a 20Ti/5CoFeB/10MgO seed to investigate the preferred orientation. Four points on the wafer are scanned with XRD, i.e. the center and 80 mm from the center towards each of the single element targets. $2\theta/\omega$ scans are shown in fig. 86 and

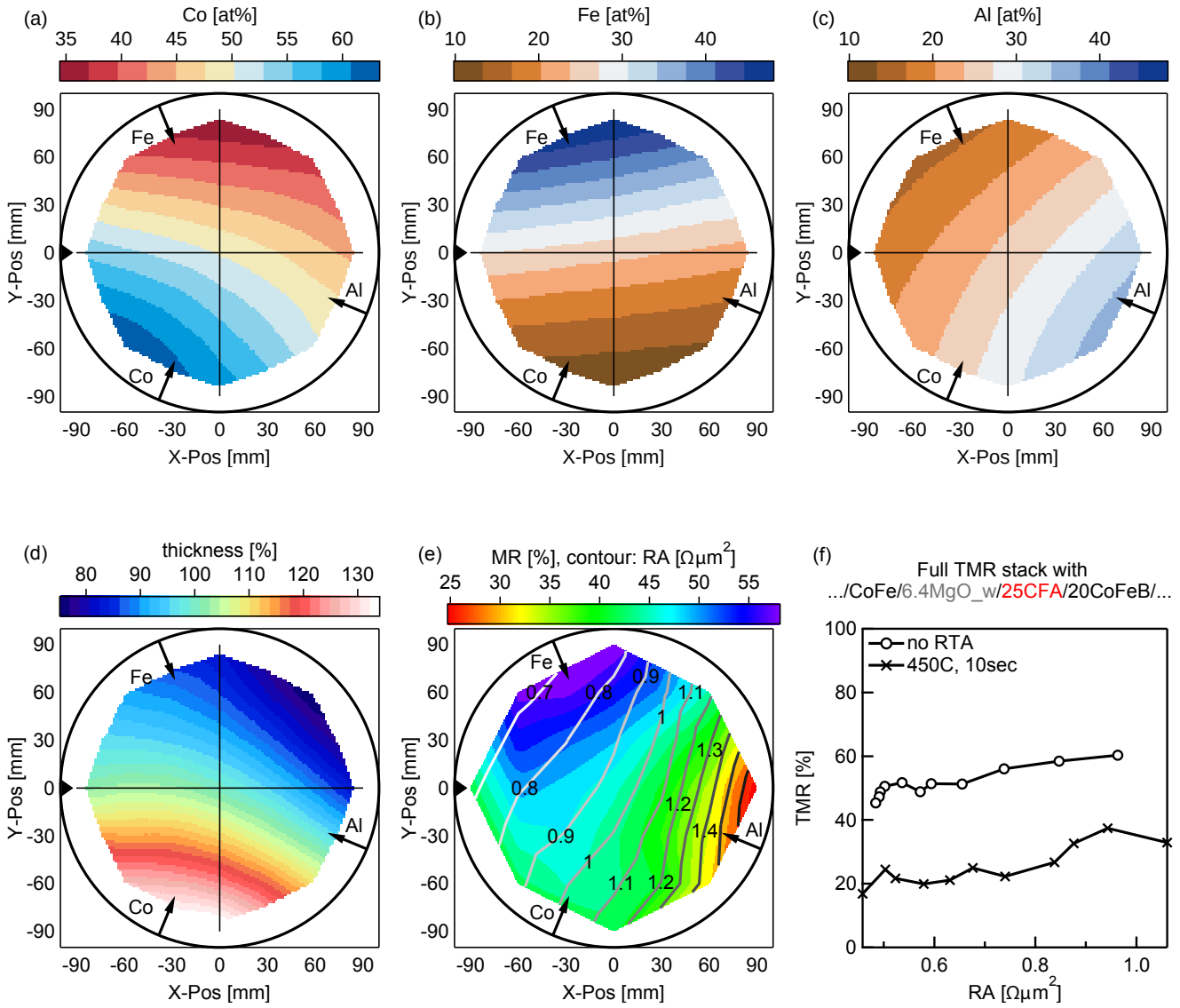

Figure 85: (a)-(c): Compositional range of the CFA gradient in at% for each element. The target positions are indicated by arrows and gradients are calculated as explained in the chapter on page 31; (d) unavoidable systematic thickness gradient profile due to CFA FL deposition without rotation and target arrangement; (e): MR and RA of the same CFA gradient as shown in (d), implemented as FL into an TMR stack as in fig. 80 and measured via CIPT. The center spot has a total FL thickness of $t_{\mathrm{CFA}} = 25$ Å; (f): Full TMR stacks with 25 Å stoichiometric CFA FL and MgO barrier thickness gradient which effectively varies RA. One of the stacks is additionally treated in-situ with RTA at 450°C for 10 seconds before the pinning annealing while the other is only annealed at 285°C for 5 hours.

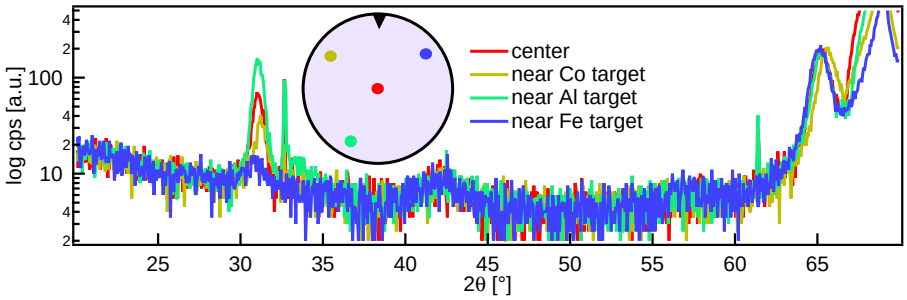

Figure 86: $2\theta/\omega$ XRD scans of the 150 Å CFA gradient on Si/SiO_2 with 20Ti/5CoFeB/10MgO seed. The inset depicts the XRD measurement spots on the wafer (the black triangle is the wafer notch).

all points exhibit pure (001)-orientation. The lattice constant for CFA (center point) is 5.69 Å, which is the same value as reported for epitaxial films on MgO[201]. It is smaller than the literature value of 5.73 Å[202] due to a 5% lattice mismatch with MgO, which elongates the lattice in-plane and reduces the out-of-plane height. The other three points are off-stoichiometric but feature the same (002) and (004) diffraction peaks as CFA when assuming the same $L2_1$ structure. Fig. 87 shows the lattice constants for off-center spots, calculated independently from the (002) and (004) reflex positions. Interestingly, all four compositions lie within the $L2_1$ phase of the calculated ternary phase diagram[203]. However, binary bcc Co-Fe combinations are added for comparability and it is pointed out that the XRD measurement spot close to the Co target ($Co_{60}Fe_{15}Al_{25}$) has with 4:1 a comparable Co to Fe ratio as the binary $Co_{75}Fe_{25}$, but features a smaller lattice constant than this phase, hinting towards a ternary compound.

The (002)/(004) peak intensity ratio is evaluated for the four positions on the CFA gradient wafer and compared to the theoretical values of the $L2_1$, B2 and A2 structure to estimate the order in the stack, see fig. 88. In the case of off-stoichiometric compositions it is assumed that an excess/deficit of atoms is equally distributed over the sublattices corresponding to the considered order. The center point with stoichiometric CFA seems to consist of mixed B2/A2 order. The intensity ratio for the composition $Co_{60}Fe_{15}Al_{25}$ matches well for $L2_1$ ordering, but since this is unlikely with the utilized annealing temperatures, it is rather a B2/A2 mix. $Co_{38}Fe_{45}Al_{17}$ agrees well with the theoretical values for $L2_1$/B2 order, most likely the excess of Fe supports crystallization. The same gradient deposition is now chosen to investigate the compositional dependence of CFA on the TMR. A full TMR stack with $t_{CFA} = 25$ Å as FL (this leads to a maximum thickness variation of ± 7.5 Å) and $t_{MgO} = 6.4$ Å is grown and treated in-situ with RTA at 370°C for 10 seconds after the deposition of CFA and CoFeB to crystallize the FL. Just like the CMS based TMR stacks, the samples are post-annealed at 285°C for 5 hours for crystallization and setting of the pinning. RA and TMR for 25 Å CFA gradient FL full TMR stack are shown in fig. 85 (e). TMR drops rapidly with increasing Al content and exhibits a maximum at an

[201] D. Ebke et al., *J. Magn. Magn. Materials* **322**, 8 (2010), pp. 996–998

[202] K.H.J. Buschow, P.G. van Engen, and R. Jongebreur, *J. Magn. Magn. Materials* **38**, 1 (1983), pp. 1–22

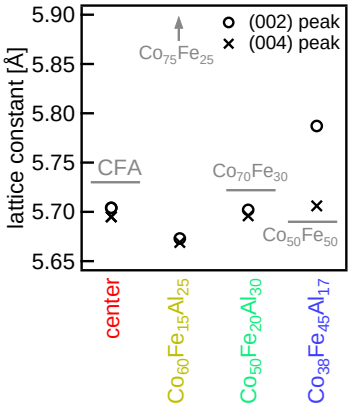

Figure 87: lattice constants of the bcc Co-Fe binary phase are: 2·2.849 Å (bcc $Co_{30}Fe_{70}$); 2·2.845 Å (bcc $Co_{50}Fe_{50}$); 2·3.008 Å (bcc $Co_{75}Fe_{25}$)

[203] C. Colinet, G. Inden, and R. Kikuchi, *Acta Metallurgica et Materialia* **41**, 4 (1993), pp. 1109–1118

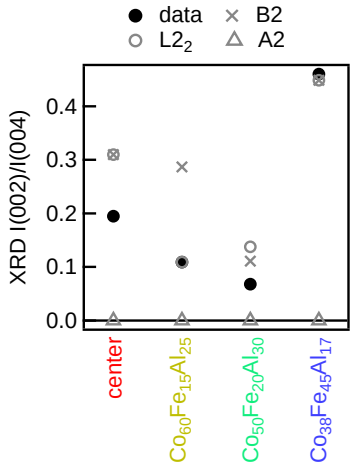

Figure 88: (002)/(004) peak intensity ratio from the data shown in fig. 86. Expected theoretical values are added for comparison.

off-stoichiometric composition of $Co_{38}Fe_{46}Al_{16}$. Further experiments, i.e. *X-ray magnetic circular dichroism* (XMCD) measurements or TEM nano-diffraction for local order investigation, are necessary to elucidate this peculiarity and the monotonic behavior of TMR throughout the compositional range.

To investigate the TMR(RA) dependence of the stoichiometric 25 Å CFA, two full TMR stacks featuring a MgO thickness wedge are deposited with $t_{MgO} = 4.9$–7.9Å. The difference between these two stacks is the previously conducted in-situ annealing: only one wafer is treated with RTA at 450°C for 10 seconds just after completing the CoFeB deposition after the FL. 450°C might be promoting better B2 crystallization of CFA and higher TMR for epitaxial samples[204], but the TMR altogether drops here, see fig. 85 (f). The overall RA is unaffected by the RTA step. Interdiffusion, specifically of B into MgO is detrimental to the TMR[205] and reducing the in-situ annealing temperature to 370°C instead of 450°C results in a significantly higher TMR($RA = 0.5\ \Omega\mu m^2$) ≈ 50%, see wafer center in fig. 85 (e). But on the other hand the 370°C anneal is inferior to the result without RTA step. No in-situ annealing leads to TMR($RA = 1\Omega\mu m^2$) ≈ 60%. So far the highest reported values were 110% at 4 $\Omega\mu m^2$ for epitaxial 25 Å CFA/MgO/CoFe MTJs[206] and about 10% at 1 $\Omega\mu m^2$ for polycrystalline 20CFA/MgO/CoFe stacks[207].

While the here reported TMR at this RA is by far the record value for polycrystalline CFA, the wafer gradient approach reveals a fundamental problem of the integration of this Heusler compound into MTJs. The successful crystallization of the $L2_1$ phase has been reported neither for polycrystalline nor epitaxial CFA films on (001)-MgO substrates below 500°C due to the thermodynamic stability of CFA[208]. Together with the XRD data this strongly suggests B2 structure at the most, i.e. Fe-Al anti-site disorder in the CFA FL. However, other types of antisite-disorder could be the reason for gradual decline of TMR with increasing Al content in fig. 85 (e), as possibly excess Al increasingly occupies Fe and Co sites leading to increasing A2-type disorder, even after high temperature post-annealing procedures[209]. This problem is known for CFA as resonant and high energy photo emission measurements by *Wurmehl et al.* show a discrepancy between bulk samples and theory and strong difference in surface and bulk signatures. One sign of (partial) A2 phase is a higher M_s than predicted for CFA[210] by the Slater-Pauling rule[211]. Specifically Co-Al disorder drastically reduces spin polarization for CFA[212]. In an attempt to recreate crystallization as observed for the thicker CFA gradient film in fig. 86, a 100 Å CFA FL is integrated into the TMR stack. As shown earlier, a thicker CFA film will lead to a small α which reflects good ordering[213]. However, a decrease in TMR is the result, most likely due to an inferior growth of thicker CFA on the MgO barrier. In order to increase TMR with CFA it is suggested to use the related quaternary Heusler $Co_2Cr_{0.6}Fe_{0.4}Al$ which has a predicted SP of 97% for the $L2_1$ phase and 94% for B2[214].

[204] D. Ebke et al., *J. Magn. Magn. Materials* **322**, 8 (2010), pp. 996–998

[205] V. Harnchana et al., *J. Appl. Physics* **113**, 16, 163502 (2013), T. Miyajima et al., *Appl. Phys. Lett.* **94**, 12, 122501 (2009)

[206] W. Wang, H. Sukegawa, and K. Inomata, *Phys. Rev. B* **82** (9 Sept. 2010), p. 092402

[207] Z. Wen et al., *Phys. Rev. Appl.* **2** (2 Aug. 2014), p. 024009

[208] R. Y. Umetsu, A. Okubo, and R. Kainuma, *J. Appl. Physics* **111**, 7, 073909 (2012)

[209] B. Balke et al., *Appl. Phys. Lett.* **90**, 15, 152504 (2007)

[210] S. Wurmehl et al., *J. Phys. D: Appl. Phys.* **39**, 5 (2006), p. 803

[211] I. Galanakis, P. H. Dederichs, and N. Papanikolaou, *Phys. Rev. B* **66** (17 2002), p. 174429

[212] Y. Miura, K. Nagao, and M. Shirai, *Phys. Rev. B* **69** (14 Apr. 2004), p. 144413

[213] S. Mizukami et al., *J. Appl. Physics* **105**, 7, 07D306 (2009)

[214] Y. Miura, K. Nagao, and M. Shirai, *Phys. Rev. B* **69** (14 Apr. 2004), p. 144413

CPP-GMR

Reduced spin-flip processes at the FM/spacer interface, as compared to a FM/barrier interface in the case of a MTJ, makes a CPP-GMR structure a promising detector for half-metallicity at RT[215]. The low RA of a CPP-GMR SV leads to low noise and high SNR ratios[216], while reducing Johnson-noise[217]. For example, an all-metal CPP-GMR multilayer with MR = 10% and $RA = 40\ \mathrm{m\Omega\mu m^2}$ has a better SNR than a TMR device with MR = 50% and $RA = 1\ \Omega\mu\mathrm{m}^2$ when reducing the sensor width below 35 nm[218].

Unlike TMR, the GMR effect originates from spin-asymmetric scattering of electrons in the spacer, spacer/FM interface and within the bulk-like region the FM. The Valet-Fert model[219] assumes diffuse transport based on the Boltzmann equation and uses a two-current series resistor in the limit of infinite spin diffusion length l_{sf}. Depending on the orientation of the conduction electron spin relative to the magnetization, the resistivity of the ferromagnet is different, i.e. shows an asymmetry with $\rho_{\mathrm{F}}^{\uparrow} < \rho_{\mathrm{F}}^{\downarrow}$, where $\uparrow$ means that the electron moment points along the magnetization and $\downarrow$ means it points in the opposite direction, where for the latter it experiences increased scattering due to higher scattering probabilities of an electron. The dimensionless bulk scattering asymmetry parameter is $\beta = (\rho_{\mathrm{F}}^{\downarrow} - \rho_{\mathrm{F}}^{\uparrow})/(\rho_{\mathrm{F}}^{\downarrow} + \rho_{\mathrm{F}}^{\uparrow})$. The same asymmetry is active on the N/FM interfaces and generally the interface resistance $R_{\mathrm{N/FM}}^{\uparrow} < R_{\mathrm{N/FM}}^{\downarrow}$. The interface scattering asymmetry analogously can be defined as $\gamma = (R_{\mathrm{N/FM}}^{\downarrow} - R_{\mathrm{N/FM}}^{\uparrow})/(R_{\mathrm{N/FM}}^{\downarrow} + R_{\mathrm{N/FM}}^{\uparrow})$.

The change in the resistance area product ΔRA is now governed by these parameters. For a $\mathrm{FM_b/N/FM_t}$ trilayer in the case of a CPP-GMR SV with the same FM material, but with different thickness t_{b} and t_{t} this leads to:

$$\Delta RA = \frac{\left[\beta\rho_{\mathrm{F}}^{*}\left(t_{\mathrm{b}} + t_{\mathrm{t}}\right) + 2\gamma R_{\mathrm{N/FM}}^{*} A\right]^2}{RA_{\mathrm{AP}}}, \tag{59}$$

where $\rho_{\mathrm{F}}^{*} = (\rho_{\mathrm{F}}^{\downarrow} + \rho_{\mathrm{F}}^{\uparrow})/4 = \rho_{\mathrm{F}}/(1-\beta^2)$ and ρ_{F} is the independently measured resistivity of the ferromagnet (in an environment without GMR). $R_{\mathrm{N/FM}}^{*} = (R_{\mathrm{N/FM}}^{\downarrow} + R_{\mathrm{N/FM}}^{\uparrow})/4$.

RA_{AP} is the resistance area product in the antiparallel state and it includes the resistances of all layers in the stack:

$$RA_{\mathrm{AP}} = \rho_{\mathrm{F}}^{*}\left(t_{\mathrm{b}} + t_{\mathrm{t}}\right) + 2R_{\mathrm{N/FM}}^{*} A + \rho_{\mathrm{N}} t_{\mathrm{N}} + R_0 A, \tag{60}$$

[215] P. Mavropoulos, M. Le žai ć, and S. Blügel, *Phys. Rev. B* **72** (17 2005), p. 174428

[216] J. R. Childress et al., *IEEE Transactions on Magnetics* **44**, 1 (2008), pp. 90–94

[217] M. Takagishi et al., *IEEE Transactions on Magnetics* **38**, 5 (2002), pp. 2277–2282

[218] K. Nakamoto et al., *IEEE Transactions on Magnetics* **44**, 1 (2008), pp. 95–99

[219] T. Valet and A. Fert, *Phys. Rev. B* **48** (10 1993), pp. 7099–7113

where ρ_N is the resistivity of the spacer and R_0A is the sum of contributions other than originating from the $FM_b/N/FM_t$ part of the stack, e.g. AFM pinning layer (see subsection *Exchange-biased CPP-GMR stacks* below), seed/buffer layer or capping layers. It is possible to account for RA_0 and extract a corrected MR by subtracting these contributions from the denominator, which however ultimately doesn't lead to any change/gain in ΔRA.
ΔRA can be plotted vs. $(t_b + t_t)$. When resistivities $\rho_{N/FM}$ and ρ_N are known and $R_{N/FM}$ is established (e.g. first principle calculations), eq. 59 can then be used to fit for β and γ.
The general HDD read head design is the same as for TMR-based sensors as illustrated in the previous section in fig. 79.

Latest reports on CPP-GMR

Compounds from the Heusler compound class currently hold the record for CPP-GMR output. The most prominent and promising candidates that have been reported for CPP-GMR in the last years are summarized in tab. 10. Epitaxial samples feature higher ΔRA due to superior crystalline quality. However, the record ΔRA values are obtained with post-annealing temperatures $T_a > 500°C$, which is unacceptable for industrial implementation. On the other hand the cited reports below the solid double line in tab. 10 use lower annealing temperature $T_a \approx 300°C$ and aim directly at realizing devices for applications. More details about the processing and parameters can be found in the respective reports. Almost all of the reports utilize full- instead of half-Heuslers, because MR is significantly higher for the $L2_1$ full-Heusler (like CMS, CFA or CFMS) as compared to the $C1_b$ half Heusler (like NiMnSb), even though the intrinsically wider bandgap[220] for the latter can be advantageous for a small temperature dependence and increased thermal stability of the MR[221].

[220] I. Galanakis, P. Mavropoulos, and P. H. Dederichs, *J. Phys. D: Appl. Phys.* **39**, 5 (2006), p. 765

[221] Z. Wen et al., *Sci. Reports* **5**, 18387 (2015)

choice of spacer layer material

Because of its superior electrotransport properties, Ag holds the record for CPP-GMR as spacer material[222]. l_{sf} of Ag thin films at 4.5 K is $l_{sf} > 26$ nm[223]. Other reports measured $l_{sf} > 40$ nm[224] and $l_{sf} > 130$ nm for Ag wires[225]. The recent use of a (111)-textured AgSn spacer in combination with (011)-CoFe as FM electrode allowed for a reduction of spacer thickness due to reduced roughness, decreased interlayer coupling and less interdiffusion upon annealing[226]. While the resistivity of AgSn is higher than Ag, it retains a long spin-diffusion length[227]. ΔRA with a spacer thickness $t_s = 40$ Å is still largest when using Ag in the report by *Read et al.*, which reminds of the intrinsic superiority of pure Ag as a noble metal with long spin-diffusion length and thus calls for only a small and diluted addition of impurities to Ag when tailoring spacer growth. However, the drastically improved corrosion-resistance

[222] J. Sato et al., *Appl. Phys. Express* **4**, 11 (2011), p. 113005

[223] G. Bergmann, *Zeitschrift Phys. B Cond. Matt.* **48**, 1 (1982), pp. 5–16

[224] W. Park et al., *Phys. Rev. B* **62** (2 2000), pp. 1178–1185

[225] R. Godfrey and M. Johnson, *Phys. Rev. Lett.* **96** (13 2006), p. 136601

[226] J. C. Read et al., *J. Appl. Physics* **118**, 4, 043907 (2015)

[227] J. Bass et al., *Mat. Sc. Engin.: B* **31**, 1 (1995), pp. 77–83

of AgSn tested by submerging CPP-GMR devices in water plays in favor of this spacer material and a trade-off in ΔRA should be considered as a reasonable approach. Other Ag-impurity combinations like Ag-Ti can potentially improve the thermal stability of the device[228].

[228] M. Kawamura et al., *Vacuum* **87** (2013), pp. 222–226

Table 10: recent output values for CPP-GMR devices. *Italic* values are at LT. Hono (2015) used a $Mg_{0.5}Ti_{0.5}O$ (MTO) seed for the (001)-textured stack.

year	FM	spacer	type	RA [mΩμm^2]	ΔRA [mΩμm^2]	group
2009	Co_2MnSi	Cr	(001)-epitax.	125	6.5	Takanashi
2009	Co_2MnSi	Ag	(001)-epitax.	31	8.9	Takanashi
2010	Co_2MnSi	Ag	(001)-epitax.	32	11.5	Takanashi
2011	$Co_2Fe_{0.4}Mn_{0.6}Si$	Ag	(001)-epitax.	156	116.7	Ando
2013	$Co_2FeGa_{0.5}Ge_{0.5}$	Ag	(001)-epitax.	21	12.0/*33.0*	Hono
2014	$Co_2Fe_xMn_{1-x}Si$	Ag	(001)-epitax.	31	17.2	Takanashi
2015	$Co_2FeGa_{0.5}Ge_{0.5}$	$Cu_{52}Zn_{48}$	(001)-epitax.	34	8.0	Hono
2015	$Co_2FeGa_{0.5}Ge_{0.5}$	AgZn	(001)-epitax.	36	21.5	Hono
2015	$Co_2Fe_{0.4}Mn_{0.6}Si$	$Ag_{0.83}Mg_{0.17}$	(001)-epitax.	36	16.0	Takanashi
2015	$Co_2FeGa_{0.5}Ge_{0.5}$	NiAl	(001)-epitax.	48	4.3	Hono
2015	NiMnSb	Ag	(001)-epitax.	26	2.1	Takanashi
2016	NiMnSb	Ag	(001)-epitax.	54	2.3	Hono
2011	Co_2MnGe	Cu	polycrystalline	40	4.0	Childress
2013	$Co_2FeGa_{0.5}Ge_{0.5}$	Ag	(011)-textured	40	4.0	Hono
2013	$Co_2FeGa_{0.5}Ge_{0.5}$	Ag	(001)-textured	36	5.8	Hono
2014	$Co_2Fe_{0.4}Mn_{0.6}Si$	Ag	(001)-textured	50	9.0	Diao
2015	$Co_2FeGa_{0.5}Ge_{0.5}$	Ag	(001)-textured	241	6.6	Hono
2015	CoFe	$Ag_{1-x}Sn_x$	(011)-textured	40–50	6.6	Childress

General requirements

Low damping is a signature of Heuslers that exhibit high spin polarization due to a lack of spin-mixing channels and is required for low thermal mag-noise in the device[229]. However, to minimize the switching time higher damping is preferable. Another way to support fast switching is by utilizing a high anisotropy field H_K. The low junction resistance R of the CPP-GMR stack, which is typically $RA \approx 50$ mΩμm^2, sets requirements for the bottom and top lead contact sheet resistance (R_b and R_t) and the device sizing. Consider a cylindrical CPP-GMR pillar with radius r_0, area $A = \pi r_0^2$ and height h exhibiting an average resistivity ρ, see fig. 89. The bottom and top contacts of width w with the resistivities ρ_b and ρ_t have thickness t_b and t_t, respectively, leading to their respective sheet resistance $R_b = \rho_b/t_b$ and $R_t = \rho_t/t_t$. Note that $\rho h = RA$.

[229] N. Smith, M. J. Carey, and J. R. Childress, *Phys. Rev. B* **81** (2010), p. 184431

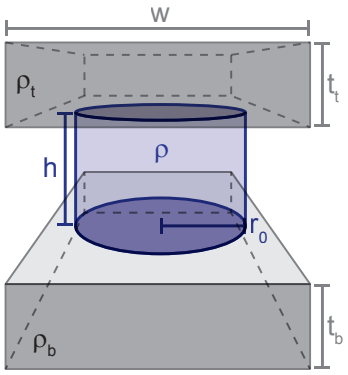

Figure 89: illustration of a CPP-GMR pillar (blue) including the contacts (gray) with properties as described in the text. The contact pads are considerably wider in reality.

Current crowding in the contacts

If the contact pad width w is much larger than the pillar junction radius r_0 a voltage drop along the contacts can give rise to an additional current-

crowding resistance R_{cc} for both the AP/P state, which altogether can reduce the measured MR. The relationship is given by[230]

$$R_{cc} \approx 0.1\,(R_b + R_t)\ln(w/r_0)\,. \tag{61}$$

In other words the lead resistance can generate relevant resistance R_{cc} along the leads if their size to pillar radius ratio is large. However, a voltage drop in the leads will ultimately only become relevant if R_{cc} is comparable to the resistance of the pillar (the smaller r_0 the higher R_{cc}, but also the pillar resistance is $R \sim r_0^{-2}$). To prevent the impact of R_{cc} on the MR measurement therefore it has to be made sure that $RA \gg R_{b/t} t_{b/t}^2$. For MTJs with large $RA \sim 1\ \mathrm{k\Omega\mu m^2}$ and a typical contact resistance of $R_{b/t} \approx 1\,\Omega$, using a millimeter-sized lead pad for a junction size of $A \approx 10\mathrm{x}10\ \mu\mathrm{m}$ (simple photo-lithographic process) will result in negligible R_{cc}. Because of the low RA of CPP-GMR SVs however, the junction size has to be considerably smaller in order to obtain a large enough measurable device resistance $R \sim r_0^{-2}$. A helpful pillar size estimation can be obtained by assessing the uniformity of the current through the junction for a given lead resistance.

[230] J. Chen et al., *J. Appl. Physics* **91**, 10 (2002), pp. 8783–8785

Non-uniform current through the pillar

Consider a situation where the contact resistivities ρ_b and ρ_t are large compared to the pillar resistance. Then the current that flows in the contacts towards the cylindrical junction will be drained along the walls of it instead of flowing uniformly throughout the whole junction.
To estimate if a current flows uniformly through the pillar with given RA, the length parameter $\lambda = \sqrt{RA/(R_b + R_t)}$ is evaluated. *Chen et al.* derived an approximate expression[231] for the spatial distribution of the voltage $V(r)$ over the pillar:

$$V(r) = cI_0(r/\lambda) \tag{62}$$

where c is a constant that depends on the boundary conditions and contains the total current flowing through the junction. I_0 is the modified Bessel function of zeroth order of first kind. Uniform current in the pillar now means that the current density is approximately equal in all regions when progressing from the edge of the pillar at $r = r_0$ towards the center $r = 0$. When r_0 is considerably smaller than λ so that $r/\lambda \ll 1$ for any $r < r_0$, the Bessel function $I_0(r/\lambda)$ is approximately equal to unity and only slowly increases $r \to r_0$ wherefore the condition for current uniformity is established. However, when $r/\lambda > 1$ the Bessel function increases exponentially ($\sim \exp(r/\lambda)/\sqrt{2\pi r/\lambda}$) and most of the current flows between r_0 and $r_0 - \lambda$ and not in the center of the pillar. Conclusively, $r_0 \ll \lambda$ has to be fulfilled for a uniform current flow.

[231] J. Chen et al., *J. Appl. Physics* **91**, 10 (2002), pp. 8783–8785

MR output and SNR

Certainly, highest MR values are desirable and a necessary condition for industrial applicability, but how much MR is really necessary? Ul-

timately, the goal for a CPP-GMR device is to achieve a high voltage output ΔU at a certain bias U, which is $\Delta U = MR \cdot U_{\text{bias}} = \Delta RA \cdot j$, where j is the operating current density. ΔU has to dominate the noise level and a high SNR is the main target. Therefore the performance of a CPP-GMR device has to be measured in a series of *quasi-static tests* (QST), where the output amplitude and noise level are monitored in a simulated device operation under constant applied field for different bias voltages. One will quickly notice that also the device size is another critical parameter, as it is linked to stray fields which in turn influence switching behavior. Another most relevant source of noise is STT, which is increasing with current density, and Johnson noise, which can be written as $U_{\text{J}} = \sqrt{4k_{\text{B}}TR\Delta f}$, where T is temperature, R is the device resistance and Δf is the operating bandwidth ($\Delta f \approx 1$ GHz).

Exchange-biased CPP-GMR stacks

For measuring GMR the strength of H_{ex} is irrelevant and only the relative alignment of the magnetization directions P or AP is important[232]. Therefore a simple exchange biased structure with FM/AFM coupling is sufficient for the RL and no complex SAF design is necessary. In this case a 25CoFe/70IrMn pinning layer combination can be used, which can either designed below or above the FL, where CoFe is adjacent to the spacer. After deposition, subsequent H-field annealing at 285°C for 5 hours sets the pinning. However, the relatively high resistivity of IrMn and the required minimal thickness of $t_{\text{IrMn}} \approx 70$ Å, see fig. 90, will reduce the MR output following eq. 59 by increasing RA_{AP} but keeping ΔRA essentially the same. Therefore a design will be favored, where the independent switching will not be generated by pinning to an AFM, but with the help of shape anisotropy. No AFM is needed for this design, also termed *pseudo spin valve* (PSV).

[232] V. S. Speriosu et al., *Phys. Rev. B* **44** (10 1991), pp. 5358–5361

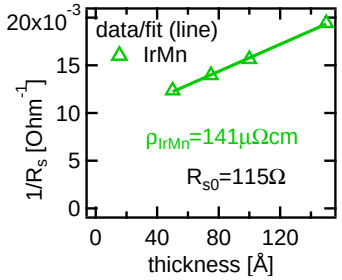

Figure 90: resistivity ρ of IrMn on Ta/Ru seed obtained by sheet resistance measurements and fitted to eq. 48.

Pseudo Spin Valves (PSV)

Independent switching of the two FM layers can be achieved by adjusting the in-plane anisotropy of either one. This can be achieved by patterning FM_{t} (FL) into an elliptical shape with axis a, b and c, thus utilizing *shape anisotropy* by the generation of a demagnetizing field $\mathbf{H}_{\text{d}}$ inside the FL. $\mathbf{H}_{\text{d}}$ will reduce the external field $\mathbf{H}_0$ to an effective field $\mathbf{H}$. Written in components one obtains:

$$H_{\text{i}} = H_{0\text{i}} - \mathcal{N}_{\text{i,j}} M_{\text{j}} \quad \text{with} \quad \text{i,j} = \text{a,b,c}. \tag{63}$$

The shape of the PSV FL can be approximated by a general ellipsoid with axis a, b and c. The demagnetization factor $\mathcal{N}_{\text{i,j}}$ then has a diagonal form with $\mathcal{N}_{\text{a}} + \mathcal{N}_{\text{b}} + \mathcal{N}_{\text{c}} = 1$ via[233]:

[233] M. Beleggia, M. De Graef, and Y. Millev, *Phil. Mag.* **86**, 16 (2006), pp. 2451–2466

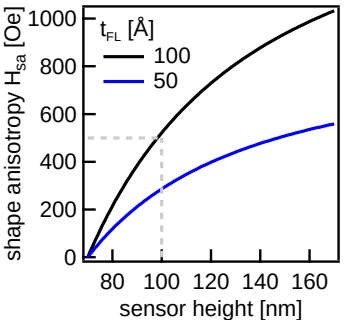

Figure 91: calculation of shape anistropy H_{sa} via eq. 63 and 64 for two different FL thicknesses with 70 nm track width and $M_{\text{s}} = 1000$ emu/cc.

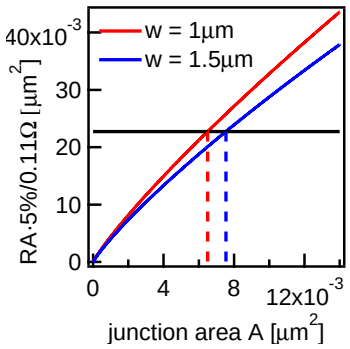

Figure 92: the goal to limit current crowding to 5% of the total device resistance (eq. 65) with a contact lead width w of 1 µm or 1.5 µm gives the upper limit for the junction size.

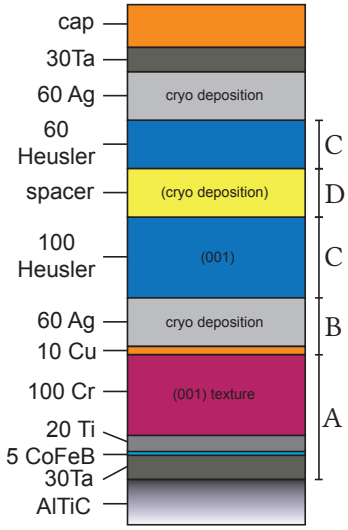

Figure 93: (001)-textured PSV design with Ag cryo deposition and Cu interlayer. The labeled regions on the right are explained in the text.

$$\mathcal{N}_c(\tau_a,\tau_b)=\frac{1}{2}\int_0^\infty \frac{dx}{(1+x)^{3/2}\left(1+x\tau_a^2\right)^{1/2}\left(1+x\tau_b^2\right)^{1/2}}. \quad (64)$$

Where $\tau_a = c/a$ and $\tau_b = c/b$. $\mathcal{N}_a$ and $\mathcal{N}_a$ are obtained by rotation, i.e. $\mathcal{N}_a = \mathcal{N}_c(1/\tau_a, \tau_b/\tau_a)$ and $\mathcal{N}_b = \mathcal{N}_c(\tau_a/\tau_b, 1/\tau_b)$.
Assuming single domains in each FM layer, the anisotropy fields can be calculated. To guarantee independent FL/RL switching it is recommended to pattern the FL so that the saturation field is $H_s \approx 500$ Oe, where $H_s = |H_c - H_b|$, i.e. the anisotropic field difference between b and c axis. The necessary sensor height (longest axis of the ellipsoid, axis c) of a pillar with 70 nm track width (axis b), 100 Å FL thickness (axis a) and $M_s = 1000$ emu/cc to provide this amount of shape anisotropy is estimated by using eq. 63 by setting $H_{0c} = 500$ Oe and with the corresponding demagnetization factors calculated using eq. 64. For the given example, the optimal sensor height is about 100 nm, see fig. 91. The total sensor thickness limits the maximum down-track resolution, which is why generally minimal FL thickness should be targeted.

Status at WD

A special CPP-GMR device production route (*short loop route*) has been implemented at WD, which allows for a high throughput device fabrication based on a PSV design. The device dimensions are chosen based on the previous considerations. Anticipating a targeted $RA = 50$ mΩµm^2 and requiring the current crowding to be less than 5% allows for a estimation of the maximum for the junction size. This is obtained by using eq. 61 and setting $R_{cc} \leq 0.05\, RA/A$, using $A = \pi r_0^2$ for approximated round pillars and inserting typical values for $R_b = 0.1$ Ω/□ and $R_t = 1$ Ω/□:

$$A \cdot \ln \frac{w\sqrt{\pi}}{\sqrt{A}} \leq \frac{5\% \cdot RA}{0.11\,\Omega}. \quad (65)$$

Eq. 65 is plotted in fig. 92 for different contact widths w and RA. The capabilities of the available photo-lithography limit the contact size to the smallest possible $w \approx 1$ µm, thus calling for a junction size of about 0.007 µm^2, which is met by considering the discussion concerning the shape anisotropy with the choice of 70x100 nm^2. This gives a read head resistance of about 7 Ω.

CPP-GMR stack design proposals

Based on the results acquired for CMS, CIMS and CFA the following stacks are proposed to be manufactured by the short loop route. Also the findings on potential spacer layer materials Ag and Cr will be contributing to the design. All stacks will be deposited on AlTiC wafers with Py-shield ($R_b \simeq 0.1$ Ω). For all stacks the top contact will be mostly consisting of Cu. With a measured $\rho_{Cu} = 2.5$ µΩcm, a film thickness of 250 Å is necessary to obtain $R_t \simeq 1$ Ω. A Ta interlayer between the cap

and the top Ag will act as a Cu diffusion barrier. TaN would be even better due to its extremely high interfacial diffusion energy barrier[234]. The thickness of Ag in these proposals is chosen because of typical values for the coalescence of islands of 30–50 Å[235]. Furthermore it has been shown here, that a Ag spacer thickness of 30 Å or below results in FM coupling for CMS. A thicker spacer with $t_s = 60$ Å that is well below l_{sf} is therefore suggested but a thickness optimization will be necessary.

[234] Y. Zhao and G. Lu, *Phys. Rev. B* **79** (21 2009), p. 214104

[235] A. Romanyuk et al., *Surf. Sci.* **602**, 9 (2008), pp. L49–L52

1. (001)-textured CPP-GMR PSV

The stack is shown in fig. 93. **A**: the best (001)-texture seed/buffer combination for low-RA stacks with $Q^{T}_{001} = 13$ is chosen. This will result in a lower RA than using recently reported rock-salt-type $Mg_{1-x}Ti_xO$ as seed[236] which exhibited $RA = 241\ \Omega\mu m^2$. **B**: a thin Cu layer will reduce the critical thickness for Ag, improve the uniformity and prevent roughening due to post-annealing. A minimal wafer temperature of −140°C is achievable prior to deposition. This guarantees minimized Ag roughness with $R_a \leq 7$ Å. All Ag layers in the stack are deposited at cryogenic temperature. **C**: FM1 and FM2 are CMS, CFA or CIMS. In-situ RTA at 370°C (CMS) or higher[237] (CIMS) for 600 seconds after finished deposition fuses the Ag/Heusler/spacer/Heusler/Ag combination by recrystallization on the Cr buffer template. A further enhancement of spin polarization in CMS and reduction of post-annealing temperature can be achieved by using an alloy target $CMS_{1-x}Ag_x$ with $x < 4.5$ at%[238]. A similar effect is to be expected with the related compound CIMS. **D**: the following spacer materials will be systematically tested: cryo-deposited Ag; $Ag_{1-x}Al_x$ with $x \approx 0.05$ for thermal stability and reduced agglomeration[239]; $Ag_{1-x}Ti_x$ with $0.002 < x < 0.005$ for lowest ρ and suppressed agglomeration[240]; $Ag_{1-x}Mg$ with $0.15 < x < 0.2$ for a higly ordered $L1_2$ phase with an ordering temperature $T < 350$°C[241]. Optimal lattice matching with CMS and CFA should also be considered.

[236] Y. Du et al., *IEEE Transactions on Magnetics* **51**, 11 (2015), pp. 1–4, B. S. D. Ch. S. Varaprasad et al., *J. Appl. Physics* **113**, 20, 203907 (2013)

[237] optimal T_a on Cr/Ag has yet to be established

[238] S. Bosu et al., *Scripta Materialia* **110** (2016), pp. 70–73

[239] H. C. Kim et al., *Mat. Research Soc. Symp. Proc.* Ed. by R.J. Carter et al., vol. 812, link, 2004, pp. 209–214

[240] M. Kawamura et al., *Vacuum* **87** (2013), pp. 222–226

[241] K. Fujiwara et al., *J. Phys. Soc. Japan* **13**, 2 (1958), pp. 167–174

2. (011)-textured CPP-GMR PSV

The omisson of a buffer layer gives this version an advantage of a reduced stack height (by 100 Å). As previously discussed, this texture generally leads to a lower MR, as compared to the (001)-type. Cu insertion will support smoother (111) Ag, even as not as significant as for (001)-texture. The stacking is shown in fig. 94.

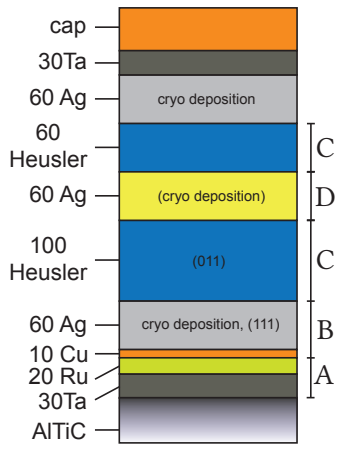

Figure 94: (011)-textured PSC design with Ag cryo-deposition and Cu interlayer.

Publications and conferences

Publications

2013

1. **Albrecht Köhler**, Ivan Knez, Daniel Ebke, Claudia Felser, Stuart S. P. Parkin: *Loss of anisotropy in strained ultrathin epitaxial $L1_0$ Mn-Ga films*, Applied Physics Letters **103**, 162406 (2013)

2014

2. Olga Meshcheriakova, **Albrecht Köhler**, Siham Ouardi, Yukio Kondo, Takahide Kubota, Shekhar Chandra, Julie Karel, Carlos V. Barbosa, Rolf Stinshoff, Roshnee Sahoo, Shigenori Ueda, Eiji Ikenaga, Shigemi Mizukami, Stanislav Chadov, Daniel Ebke, Gerhard H. Fecher, Claudia Felser: *Structural, electronic, and magnetic properties of perpendicularly magnetised Mn_2RhSn thin films*, Journal of Physics D: Applied Physics **48**, 164008 (2014)

2016

3. **Albrecht Köhler**, Lukas Wollmann, Daniel Ebke, Stanislav Chadov, Christian Kaiser, Zhitao Diao, Yuankai Zheng, Qunwen Leng, Claudia Felser: *Tunable damping in the Heusler compound $Co_{2-x}Ir_xMnSi$*, Physical Review B **93**, 094410 (2016)

Conferences

2013

1. Albrecht Köhler, Ivan Knez, Daniel Ebke, Claudia Felser, Stuart S. P. Parkin: *Loss of anisotropy in strained ultrathin epitaxial $L1_0$ Mn-Ga films*, ASPIMATT summer school and annual meeting, Dresden

2014

2. Albrecht Köhler, Lukas Wollmann, Daniel Ebke, Stanislav Chadov, Christian Kaiser, Zhitao Diao, Yuankai Zheng, Qunwen Leng, Claudia Felser: *CPP-GMR Heusler devices with tunable damping constant*, IEEE Intermag Europe, Dresden

Acknowledgement

I would like to thank everybody who supported me in the making of this work. My deepest gratitude and appreciation goes towards *Prof. Claudia Felser* and *Prof. Stuart Parkin* for providing the possibility to be a part of this global research effort at the dawn of spintronic technologies. Thanks to *Prof. Mizukami* and your research team for the hospitable welcome in Tohoku and for letting us use your laboratory equipment. Thanks to all the bright minds at both the Max-Planck-Institutes in Halle and Dresden for the good times and your cooperative spirit. *Lukas Wollmann*, *David Bende* and the whole Felser team: thanks for the inspirational talks, the successful research and the friendships we built together. I wish we could continue to work on our cutting edge ideas. Thanks to Daniel Ebke who inspired me to strive towards elegant design for scientific publishing and got me hooked on evaluating my data via customized scripting in Igor Pro. Special thanks to *Christian Kaiser*, my supervisor at Western Digital®, for your unwavering support and scientific guidance into the world of applied nanotechnology. Thanks to *Josh Jones* for being a like-minded collegue and friend and for all your contributions to the design of the FMR system. I would also like to thank *Yuankai Zheng*, *Zhitao Diang* and the former members of the WD R&D team *Xin Xiang* and *Qunwen Leng* for your inspiration, collaboration and the amicable team spirit. Thanks *Lilly Ou* for the good times and your support. Big thanks also to *Lena Miloslavsky* for letting me use the XRD-system and *Rima Leonov* for fast action on all AFM measurements. Furthermore a big thumbs up to *Mai Dang* for your technical realization of the FMR in-plane holder and your progressive thinking and to *Yang Dong* for your technical support. Furthermore I would like to express my gratitude towards the lab engineers at WD: *Dennis Rafferty*, *Susan Legaspi*, *Mai Huynh*, *Nai Yang* and *Edna Dilinila*. Thanks to my parents who have always supported me in achieving my goals. Thanks to my lovely wife *Christianna* for supporting me in the tedious writing phase and for expanding my perspective on life.

Personal details and educational background

Albrecht Köhler was born in Leipzig on 17th of February 1987. His interest in scientific methodology, for which the foundation was laid in the *Sächsisches Landesgymnasium Sankt Afra zu Meissen*, led him to the studies of physics at the *Goethe-University* in Frankfurt a.M. from 2006 to 2012. He obtained his B. Sc. in experimental thin film physics in 2009 after working on Josephson junctions in the group of Prof. Michael Huth. He continued his research in the same group to aim for his M. Sc., which he completed in 2012 after the investigation of the novel Si-thin film precursor Neopentasilan. In order to pursue his promotional studies on Heusler thin films in the group of Prof. Claudia Felser he relocated to the *Max-Planck-Institute of Chemical Physics of Solids* in Dresden. This enabled him to take part in a multitude of international research efforts, such as the first growth of Heusler thin films which exhibited the signatures of Skyrmions at the *Advanced Insitute of Materials Research* in Tohoku (Japan) with the group of Prof. Shigemi Mizukami. During a subsequent 3-month research exchange at *IBM* in Almaden (CA, USA) he uncovered fundamental properties of ultrathin, perpendicularly magnetized Heusler-type hard magnets for MRAM applications. It was there where his interest for the progressive style of research in the Silicon Valley was primed. At IBM he started to work with renowned physicist Prof. Stuart Parkin, which would later become director of the *Max-Planck-Institute of Microstructure Physics* in Halle, Humbold-Professor at the *Martin-Luther University Halle-Wittenberg* and ultimately his promotional supervisor. A 2-year research collaboration at *Western Digital* in Fremont (CA, USA) to develop the next-generation HDD-read heads equipped with highly spin-polarized Heusler compounds and utilizing TMR and CPP-GMR technology led to the content of this dissertation.

Albrecht Köhler, 15th of November 2016